Microfabrication of Microdischarge-Based Sensors and Actuators

By
Ravish Malhotra

**A dissertation submitted in partial fulfillment
of the requirements for the degree of
Doctor of Philosophy
(Electrical Engineering)
in the University of Michigan
2014**

Doctoral Committee:

Professor Yogesh Gianchandani, Chair
Professor Mark Kushner
Professor Khalil Najafi
Professor Luis Bernal
Scott Green, Research Scientist

Started from the bottom, now we're here

-Drake

Dedication

To my parents:

For giving me the happiest and the safest childhood

To my two sisters:

For giving me countless memories which will always keep me happy

Acknowledgements

Firstly, I would like to acknowledge my advisor professor Gianchandani for providing me with the opportunity to do research with his group. My fondest memories and unsurprisingly, the most stressful ones involved solving some of the research problems presented to me. I learnt numerous new approaches/concepts and ultimately developed a certain amount of joy in finding things out. In this journey, many people helped me along.

Dr. Scott Green was my first mentor and under his tutelage I picked up a lot of his approaches in solving problems ingeniously. He showed utmost patience in explaining important concepts, regardless of how trivial they might have seemed to him. Dr. Christine Eun showed me the ropes in the radiation detector project. She trained me on the appropriate instruments and to this day, I use many of the things she left behind.

All the people in my research group, past and present. They were the most supportive group of people I could have worked with. Always ready for any help or guidance they could provide.

In my time here at Ann Arbor, I had a small but very close group of friends. I would especially like to thank Anup for countless times he had helped me with various things I might have thrown at him. I especially enjoyed my numerous conversations with Anurag about most conceivable topics. I sincerely hope that we change the world in our little ways

Finally, I would like to thank my mother for her support, unconditional love and great food, without which I could not have completed the PhD. My dad for his constant support and my two sisters for their love and keeping me grounded whenever I acted funny. My girlfriend Neha, for showing unconditional support, believing in me when I surely did not believe in myself.

Table of contents

List of Figures

List of Tables

List of Appendices

Abstract

For sensors and actuators that use microdischarges, microfabrication technology provides both portability and ease of integration into microsystems. This thesis investigates two types of microfabricated devices: sputter ion pumps (SIP) to control on-chip vacuum, and miniature radiation detectors for sensing beta particles, gamma rays or neutrons.

The SIP utilizes lithographically micromachined Penning cell array to ignite a plasma at pressures as low as 1.5 μTorr. The system pressure is reduced from 1 Torr to <10 mTorr. By reducing the interelectrode distance, the plasma is ignited as low as 400-600 V, compared to >2000 V for commercial devices. The resulting power consumption is 100-250 mW. The overall pump volume is 0.2 cm^3.

A microfabricated neutron detector, operating in the Geiger Muller regime, utilizes electrodes that are lithographically micromachined from 50-μm thick stainless steel #304 foil. The cathode is coated with 2.9-μm thick layer of Gd on one side to convert thermal neutrons into fast electrons and gamma rays, which are then detected by ionization of the fill gas (Ar). Three electrodes are stacked in a cathode-anode-cathode arrangement, separated by 70-μm thick polyamide spacers, and assembled within a commercial TO-5 package. For a 90 μCi ^{252}Cf neutron source, placed at a distance of 10 cm from the detector, the total neutron count rate with an applied voltage of 285 V is typically 8.7 counts per minute (cpm). Detector dead time is measured as 5.3 ms. The device is operated at lower voltages with a reduced volume and can detect beta particles, gamma rays and neutrons, when compared to commercial devices which operate at >900 V, have a higher detector volume (>100 mm^3) and can only detect a subset of the listed radiation.

Finally, this thesis describes a new architecture for microdischarge based radiation detectors intended to enhance stability, improve sensitivity and reduce dead time. The device stability can be improved through use of an asymmetric electric field between the anode and cathode. Detector sensitivity can be improved through use of stacked cathodes as it increases radiation interaction probability. The device dead time can be improved by having multiple detectors operate in parallel.

Chapter 1: Introduction

1.1 Motivation

In the past decade, microdischarges have been explored in a variety of sensing and actuating devices. Microdischarges can be easily operated at pressures exceeding atmospheric pressure by reducing the interelectrode distance [Pas87]. By miniaturizating microdischarge-based devices, very high power densities can be achieved without requiring high power: while conventional plasmas may operate at 10-500 mW/cm^2 of electrode area, volumetric power densities in the tens of kW/cm^3 can be achieved in microdischarges [Ede05, Foe06]. A variety of important applications can be addressed by discharge-based microsystems.

There is a growing need for chemical sensing in applications ranging from environmental monitoring to homeland security. The emission spectrum of a discharge arises from spontaneous emission due to relaxation of excited chemical species to ground state [Mit08, Eji00]. Therefore, in principle, a single observation of a pulsed discharge can provide information regarding the composition of ambient gas.

Microdischarges can enable pressure sensing in high temperature environments over a wide range of pressure. Devices utilizing microdischarges are suitable for high temperature operation because the electrons and ions have average energies in the range of 1-3 eV [Ede05, Foe06, Mit08, Eji00] and >0.03 eV, respectively, in an ambient environment. Consequently, the species are only minimally affected by a high or low temperature ambient, making it possible for microdischarge-based devices to operate at elevated or cryogenic temperature. Three microdischarge based pressure sensors have been reported in the past. One approach exploits the variation in the mean free path of gas molecules as a function of pressure [Wri12a]. The other approach measures the deflection of a diaphragm electrode resulting from an external pressure

[Wri12b, Luo14]. There are other interesting applications for microdischarges, two of which will form the subject of this report: use of microdischarges to control the pressure of a system in a micro sputter ion pump (SIP) [Gre13] and microdischarge-based radiation detectors that operate in the Geiger-Muller (G-M) regime [Eun10, Eun 11].

SIPs operate by creation of discharges between electrodes. Ions, after acceleration and collision with the titanium cathode, sputter fresh titanium onto the surrounding walls and anode. The titanium getters reactive gases like nitrogen and oxygen and buries noble gases like argon and helium to reduce system pressure and generate vacuum. To operate at low pressures, an externally applied magnetic field can be used to trap electrons which eventually ionize surrounding gases.

For microdischarge based radiation detectors, incident radiation ionizes fill gas. Under an applied bias, the ions and electrons are swept to the cathode and anode respectively, resulting in a current pulse. Additionally, the detectors inherently generate ultra-wide band (UWB) signals which can be used to create wireless sensor networks [Nem04, Kyk04].

The goal of this research is demonstrate microdischarge based sensors and actuators which utilize micromachining techniques to demonstrate device compactness and lower power consumption. These are important considerations because there is a great need for highly integrated sensor and actuator suites (for instance, in current smartphones) that enable detection of multiple phenomena and appropriate responses. For instance, integration of a micro radiation detector with a micro gas-chromatography system on the same chip can enable detection of dirty nuclear bombs and/or other harmful explosives (TNT, RDX) at the same time. Another example is a micromachined vacuum pump, which may be used for modulating the pressure within a

variety of vacuum electronic devices, such as chip scale atomic clocks. Use of micromachining technologies helps leverage the existing fabrication knowledge base to achieve devices that are smaller in volume while achieving superior performance than their macro counterparts and operating at voltages which easily lends them to integration. In doing so, the entire field of MEMS stands to benefit from microdischarge based devices as these can open new avenues of applications where none existed previously or at the very least improve the status quo.

In view of the above, the following sections introduce and detail state of the art for two applications of microdischarges. Section 1.2 introduces the SIP, discussing its applications while comparing it with other micro machined vacuum generation alternatives. Section 1.3 does the same for microdischarge based radiation detectors. Section 1.4 discusses the common goals and challenges associated with both the devices.

1.2 Sputter Ion Pump

On-chip vacuum generation is an attractive alternative and complement to vacuum sealing for microsystems that require very long-term or very precise control over package pressure. Examples of microsystems with these requirements include resonators and frequency references, which take advantage of the minimized damping; chip-scale atomic clocks, which have more stable temperature characteristics when operated in vacuum; and portable mass spectrometry systems, which require a minimum vacuum level to ensure no unwanted sample-to-gas collisions occur [Lut04, Zoo92, Hwa06]. In micro-scale packages with reduced volumes, the pressure increase due to even small outgassing and leakage sources is amplified. Thus, the presence of a vacuum pump can add to system robustness and reduce requirements for hermetic sealing and use of low outgassing materials.

The applications mentioned typically require a vacuum level of 1 Torr (133.3 Pa) and below. This pressure regime is not well met by chip-scale mechanical peristaltic pumps or thermal transpiration (Knudsen) pumps [Gup12], as the compressibility of the gas at low pressures works against the peristaltic pumps and the required scaling of viscous flow channels at low pressures works against the Knudsen pumps. The operating pressure range trends for various micromachined vacuum pumps are shown in Fig. 1-1.

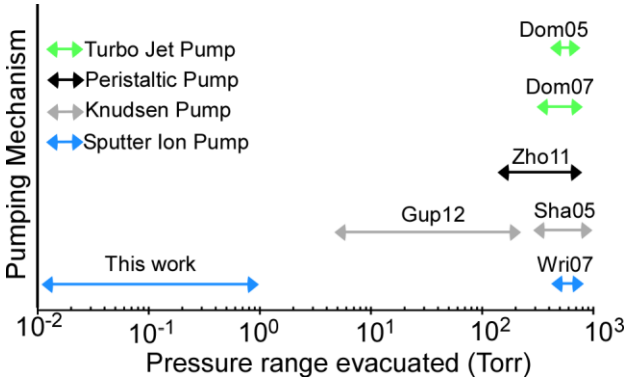

Figure 1-1: Pressure regimes for various micromachined vacuum pumps.

In general, SIPs are simple in structure, consisting of electrodes spaced by gaps in which the gas that is to be pumped resides prior to pumping (Fig. 1-2). SIPs operate by using high electric fields between the electrodes to ionize the gas; the ions are accelerated toward the titanium cathode(s) with sufficient energy to sputter the cathodes and expose fresh titanium. The exposed and deposited titanium getters reactive gas molecules (such as oxygen and nitrogen) from the atmosphere, while inert gas molecules (such as argon) are ionized and implanted in the cathode or are buried by the sputtered material. This effectively lowers the package pressure.

Previous micro-SIP efforts utilized thin-film planar titanium electrodes with small (<150 μm) electrode gaps, and operated at near-atmospheric pressures [Wri07]. At low pressures and for reduced package dimensions, the increased mean free path of electrons results in unwanted electron-wall collisions prior to ionizing collisions. The wall collisions hamper ionization

efficiency; indeed, at low enough pressures, the ionization process is so inefficient that required voltages for breakdown in the electrode geometries previously studied are substantially increased and highly impractical to apply.

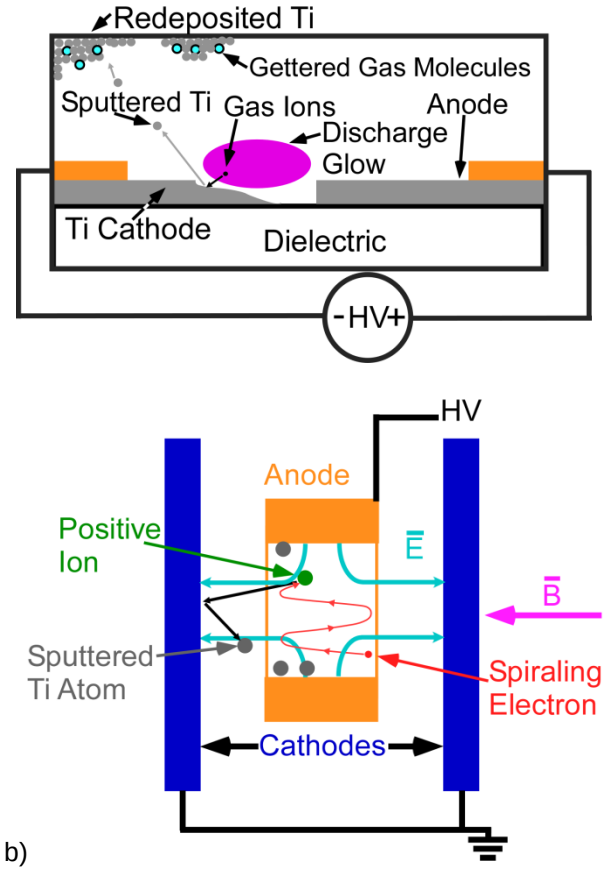

Figure 1-2: Sputter ion pump (SIP) and Penning cell operating principle. a) In an SIP, the gas between electrodes is ionized and sputters the titanium cathode. The exposed and re-deposited cathode material chemisorbs active gases and buries noble gases, effectively reducing the pressure. b) The crossed electric and magnetic fields and potential energy valley in the center of the Penning cell trap electrons in long oscillating orbits, increasing the ionization efficiency at low pressures.

One way of overcoming this effect is to trap the electrons in long orbits through the use of electric and magnetic fields and the Lorentz forces that arise from these fields. One architecture that can trap electrons in such a way is a Penning cell [Pen37, Sch67]. A single Penning cell consists of a cylindrical anode sandwiched between two planar titanium cathodes, resulting in radially-directed electric field lines at the mid-length of the anode cylinder. This arrangement,

along with an axially directed magnetic field of sufficient strength, will cause electrons in the cell to spiral indefinitely – or until an ionizing collision with a gas molecule can occur. The detailed discussion of design, fabrication and testing of the device is discussed in Chapter 2.

1.3 Radiation Detectors

Environmental monitoring is emerging as a significant driver of microsystems technology. One sensor category of particular interest is radiation sensing. There is a rising demand for microsystems that can provide real-time, first alert information on the presence of dangerous radioisotopes. In particular, these miniaturized detectors can target applications ranging from monitoring radiation safety levels of nuclear power plants to guarding against illicit trafficking of radioactive chemicals and port screening for homeland security.

The miniaturization of radiation detectors can lead to ultra-portable and reconfigurable sensor systems, reduce power requirements, and permit the use of lithographic manufacturing to drive down sensor cost. In addition, smaller sensor dimensions allow for the formation of composite sensor structures, which can increase overall functionality. Finally, scaling down feature sizes and electrode spacing can lead to increased resolution in imaging applications. Miniaturized radiation sensors with wireless signaling capability can be useful both in networks and as individual devices. As elements of a network, they can facilitate cost-effective sensing in public spaces (e.g., football stadiums, amusement parks, and shopping malls), or in dangerous and inaccessible environments (e.g., contaminated or remote areas). Individually, they could be used in applications for which the weight or space is at a premium, e.g. micro-air vehicles (MAVs), or helmets. In general, such devices offer high portability, minimal power demands, and modest manufacturing costs.

Radiation can be classified into three different types: 1) charged particles such as alpha particles and beta particles, 2) high energy electromagnetic waves like X-rays and gamma rays and 3) neutrons. Detection of neutrons is particularly challenging because these carry no charge and thus cannot be influenced by electric fields. This gives neutrons high penetration depth and allows them to pass through detectors without interaction. The problem is further exacerbated when using miniaturized detectors as these have a limited interaction area for the incident radiation.

Neutron detection can be made possible through use of a material like Gd which has a high neutron interaction probability. Gd converts neutrons into beta particles and gamma rays, which in turn can be detected through gas ionization under an applied bias. Since the conversion products of Gd are beta particles and gamma rays, a detector that utilizes Gd can sense all three different types of radiation. Typically, other radiation detectors are only sensitive to a subset of the three types of radiation. Table 1-1 shows the current state of the art for micromachined gas-based detectors used for detecting beta particles, gamma rays, neutrons or a subset of these radiations.

Table 1-1: Comparison of various gas-based radiation detectors. Commercial macroscale G-M detector are intended for γ rays.

	β particles	γ rays	Neutron
This work	✓	✓	✓
MSGC [OED95]	✓		✓
MWPC [Cha68]	✓		✓
GEM [Sha06]	✓		✓
Si micromachined [Eun08]	✓		
Proportional detector- Ar fill gas	✓		
Microdetector [Eun10], [Eun11]	✓	✓	
MicroMEGAS [Cha02]			✓
^{6}Li converter [Eng04]			✓

To be able to take advantage of miniaturization and the rapid adoption of these detectors it is important to improve upon the device parameters not only in terms of device volume but also increased sensitivity. This forms the basis of the redesigned architecture which utilizes stacked cathodes to increase the probability of interaction with gamma rays. Since the probability of interaction of gamma rays is proportional to metal thickness, the detector sensitivity can thus be improved. Fig.1-3 shows the target sensitivity against currently available commercial detectors. Along with increased sensitivity, the detector is more stable as it is less prone to spurious discharges. This is achieved by having an asymmetric electric field distribution between the anode and the cathode. The detector dead time which is the amount of time the detector is unavailable after a detection event is also reduced by use of multiple detectors operating in parallel.

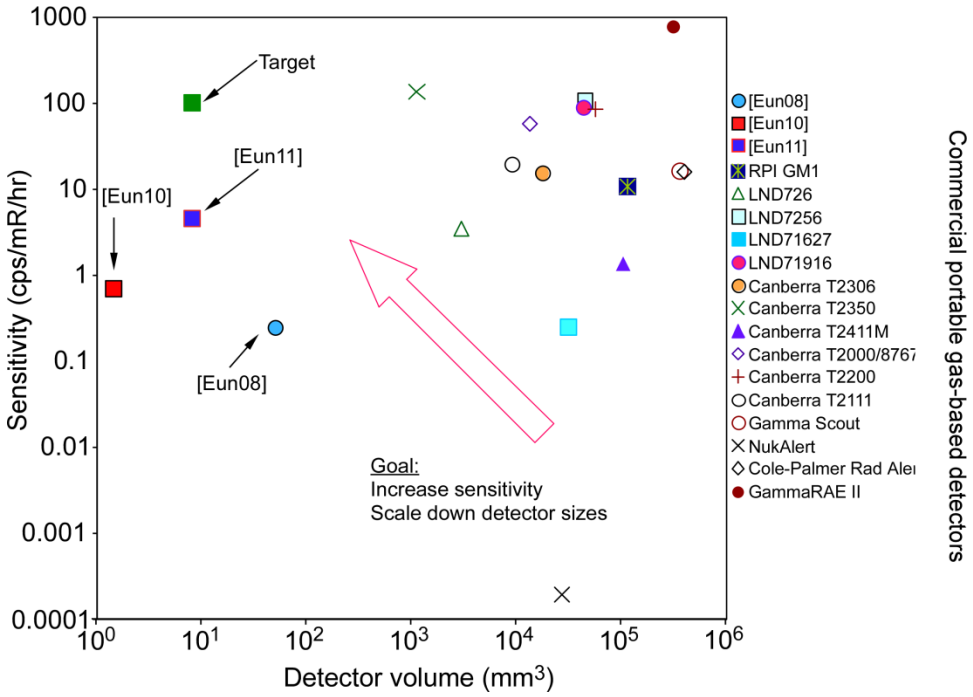

Figure 1-3: Detector volume versus sensitivity for various gamma radiation detectors

1.4 Goals and Challenges

The overall goal of this work is to leverage micromachining techniques in manufacturing microdischarge devices which demonstrate device compactness and lower power consumption. In doing so, a common set of challenges arise for both SIP and radiation detector devices: 1) Minimize interelectrode distance to reduce operating voltages. Because both devices operate at higher pressures than used conventionally, it is important to reduce the inter electrode distance so that a discharge can be started at lower voltages in effect, reach the Paschen minimum of the lowest discharge causing electric field for a given pressure-electrode distance product. 2) Reduction of device footprint to enhance portability. This will require careful assessment of the fabrication and assembly techniques to optimize area versus throughput of the actuator and sensitivity of the sensor device. 3) Limitations imposed by lithographic manufacturing on the device structure, usable materials, assembly, packaging and gas encapsulation.

In the end, the main contributions of this work are expected to be: 1) demonstration of vacuum pumping and plasma ignition for micromachined SIP at pressures lower than previously achieved (~mTorr) while reducing operating voltages by the use of a Penning cell architecture; 2) demonstration of a neutron detector working at atmospheric pressure while using a small footprint to enhance integration and portability, 3) demonstration of a gamma radiation detector that utilizes a multi stack architecture to increase sensitivity, asymmetric electric field distribution to improve device stability and multiple detectors operating in parallel to reduce system dead time. In each application, critical design parameters and fabrication considerations will be identified for use in future generations of the devices.

The preliminary report begins with Chapter 2 outlining the functioning of an SIP fabricated from micromachined titanium cathodes and SS 304 anodes, and use of external magnets to

enhance operation at low pressures while still maintaining a comparatively lower operation voltage. Chapter 3 describes the fabrication and testing of microdischarge-based detectors targeted towards sensing of neutron radiation. The device uses micromachined electrodes separated by polyamide spacers to minimize interelectrode distance. Chapter 4 describes the design and fabrication of a stable and sensitive device architecture which can be used to detect gamma radiation

Chapter 2: Micro Sputter Ion Pump

2.1 Introduction

[1]Macro-scale SIPs utilize Penning cell architectures as a standard [Wel01, Sag94]. These pumps are typically targeted for operation at 10^{-3}-10^{-9} Torr (133.3 mPa – 133.3 nPa), with pumping speeds at these respective pressures of 1 Torr-L/s – 1 μTorr-L/s (133.3 Pa-L/s – 133.3 μPa-L/s) for air. The diameter of a single anode cylinder (D_A) in macro-scale SIPs is typically 1-3 cm, and the length of the anode (L_A) is typically equal to the diameter. Electrode gaps (g) are between 0.6 cm and 1.0 cm. The required magnetic flux density for trapping electrons in such a structure is typically 0.1 T, and the applied voltages are 3-7 kV. In order to deliver the required magnetic flux in macro-scale SIPs, AlNiCo or Ferrite magnets that are typically 10 mm thick are used. To show that SIPs present a viable option for chip-scale pumps at sub-Torr pressures, anode dimensions need to be scaled down to the ~1 mm length and diameter range; ideally, operating voltages can also be scaled down to make power supply and voltage feedthrough requirements more manageable. To this end, this work presents theoretical modeling and experimental validation of a miniature Penning cell array SIP architecture. Important design and modeling considerations are described in the next section, followed by a description of the device fabrication. Experimental methods and results are then presented and discussed.

2.2 Design and Modeling

There are a number of material and geometry considerations that play into the design of a chip-scale SIP:

2.2.1 Electrode Materials

The cathodes should be formed from a gettering material such as titanium. Because the

[1] This work was performed in collaboration with Dr. Scott Green

cathodes will be continuously eroded by the sputtering action during pump operation, thicker cathodes will result in longer pump lifetime. The anode must have low relative magnetic permeability. This results in a uniform magnetic flux density within the anode cylinder, leading to efficient electron trapping. Candidate materials for the anode include aluminum and non-magnetic stainless steels such as annealed type 304 stainless steel and austenitic stainless steels.

2.2.2 Package Materials

The ionization of the gas will require the sustainment of a relatively large electric potential between the electrodes. Because the miniaturization of the SIP will necessarily reduce the gaps between the electrodes, the resulting electric fields will also be relatively large. Thus, at least the portion of the package between the anode and cathode must be fabricated from superior insulating materials. In addition, to minimize the gas load that the device is required to pump, the materials that comprise the package should have low outgassing properties and – if necessary for high and ultra-high vacuum applications – the ability to withstand baking at temperatures as high as 300^{o}C. Ceramics are particularly suited to these requirements.

2.2.3 Magnetic Circuit Materials

The permanent magnet material should be that which provides the highest remanent magnetization; this results in a minimum magnet thickness for a given required flux density. High remanence magnetic materials like neodymium-iron-boron are thus indicated. To improve the uniformity of the flux density within the Penning cells, as well as to shield other nearby devices from the effects of the strong magnetic fields, a magnetic circuit consisting of highly permeable material (such as low-carbon steel) can be used. High permeability and high saturation values will allow minimum thicknesses with maximum shielding for these materials. The magnetic circuit materials may be outside the vacuum envelope and removable for many applications; however, for certain highly integrated applications the magnetic circuit materials

may be inside the vacuum envelope or fixed to the device. In these applications, outgassing and bakeability (including Curie temperature considerations) may be concerns depending on the required vacuum levels.

The scaling of the Penning cell to millimeter dimensions is expected to affect a number of the operating characteristics of the SIP. Pump operational pressure is determined by the electrode gap and anode diameter. For pressures at which the electron mean free path is comparable to or shorter than the gap between the electrodes, the plasma that is created will be similar to the parallel-plate glow discharges that have been studied at these scales previously [Wri07]. The mean free path of an electron is about 100 μm at 1 Torr (133.3 Pa); thus it is expected that electron spiraling for improved ionization efficiency is only important at or below around 1 Torr (133.3 Pa) for pumps of the dimensions studied here. The ability for the Penning cell to cause electrons to spiral is mainly a function of anode diameter in combination with the axial magnetic flux density. An anode with smaller diameter requires larger magnetic flux density to trap the electrons. The ability of the cell to trap electrons determines the lowest pressure for gas ionization and pump operation.

Pump throughput is proportional to ionization rates, sputtering rates, and pump conductance [Wel01, Sag94, Sue95]. With respect to pump geometry, the ionization rate is directly proportional to the volume of the cell, as larger cells can trap larger numbers of electrons and gas molecules and thus promote ionizing collisions. Sputtering rates are typically related to the ionization rates and thus proportional to cell volume. However, the cell surface area and electrode gap – in conjunction with the operating pressure – can affect the plasma resistance (and thus the voltage that can be sustained across the plasma for a given input power) and the number of parasitic ion-neutral collisions that occur prior to the ion striking the cathode. A lower

sustained voltage and a higher number of parasitic ion-neutral collisions will lower sputtering efficiency and thus reduce sputtering rates.

Models of the complete performance of macro-scale sputter ion pumps typically rely on empirical relationships between geometrical factors and pumping rates [Sag94, Sue95]. The difficulties in modeling charge distribution within a Penning discharge – especially as the pressure (and thus discharge regime) changes – result in this reliance on empirical relationships. These empirical relationships are highly non-linear and are not generated from or appropriate for pumps with dimensions similar to those studied here. The development of more appropriate empirical models is outside the scope of this work. However, a subset of the pump operating characteristics – including cut-off magnetic flux and expected sputter yield – can be analyzed in more detail as described in the subsequent sections.

2.2.4 Magnetic Flux Considerations

In order to trap the electrons in an extended spiral path within the Penning cell, an axially-directed magnetic field of sufficient strength must be applied. To estimate the flux density required for Penning cells of the scale investigated in this work, electromagnetic steady state finite element analysis was utilized. This analysis calculated the electric field and magnetic flux resulting from a given voltage, applied field, and geometry, and used them to predict (through Lorentz force calculations) the motion of an electron ejected from the cathode surface with an assigned kinetic energy. The Lorentz force vector equation applied was as follows:

$$m \cdot \vec{a} = \begin{bmatrix} qE_x + q(v_y B_z - v_z B_y) \\ qE_y + q(v_z B_x - v_x B_z) \\ qE_z + q(v_x B_y - v_y B_x) \end{bmatrix}, \tag{2-1}$$

where q is the charge of the particle (-1.602 x 10^{-19} C), m is the mass of the particle (9.1095 x 10^{-}

^{31} kg), $\vec{E}$ is the electric field vector, $\vec{a}$ is the acceleration vector, $\vec{v}$ is the velocity vector, and $\vec{B}$ is the magnetic flux density vector.

For this investigation, COMSOL Multiphysics (COMSOL, Inc.; Burlington, Mass., USA) was used. The initial kinetic energy assigned to the ejected electrons was equal to the work function for titanium, or 4.3 eV [Arc73], with initial velocity normal to the cathode surface and ejected from a radial position equal to 75% of the anode radius. A uniform magnetic flux density was applied along the length of the anode, the anode surfaces were given a specific potential equal to the applied voltage, and the cathode surfaces were set at ground potential. Anode length, anode diameter, and electrode gap were varied and the effects analyzed. The cut-off magnetic flux can be estimated by noting the magnetic flux at which the electron spirals within the cell indefinitely (Fig. 2-1a), rather than colliding with the anode (Fig. 2-1b). From a perspective of device performance, the cut-off magnetic flux is the lowest magnetic flux that will result in plasma discharge at very low pressures. The results were most sensitive to anode diameter; typical cut-off magnetic flux densities for anode diameters in the 1-2 mm range were estimated at 0.2-0.4 T. Selected results for experimentally evaluated geometries are shown in Table 2-1. The results of this investigation were negligibly sensitive to the initial electron energy.

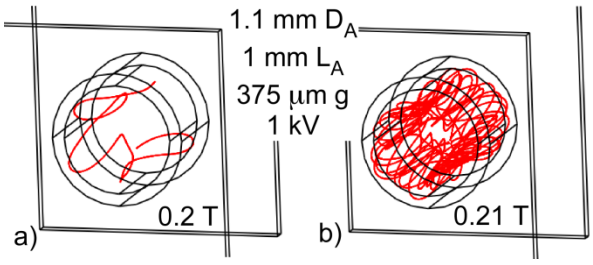

Figure 2-1: a) With insufficient magnetic field, an electron will collide with the anode before significant spiraling occurs. b) A small increase in the magnetic field leads to long electron spirals, with the probability for ionization greatly increased.

Table 2-1: Device details including architecture and geometrical parameters (electrode gap, g; anode diameter, D_A; number of cells, n) and calculated estimates of cutoff magnetic flux density (B_{cut}).

Device	Arch.	g (mm)	D_A (mm)	n	B_{cut} (T)
A	Folded Cathode	1	1.5	8	0.18
B	Folded Cathode	1	1	16	0.20
C	Ceramic Base	0.4	1.5	8	0.26
D	Folded Cathode	1	1.5	8	0.18

For this device, the required magnetic flux is to be provided by bulk magnets located outside the cathodes. To estimate the size of magnets that will deliver the required flux, finite element analysis was again utilized. In magnetostatic axisymmetric and three-dimensional models, subdomains representing the magnets were given a remnant magnetization of 1.2 T, typical of that of neodymium magnets [Mye97]. A magnetic circuit, along with the non-linear effect of saturation of the magnetic circuit was incorporated in the model [Pal07]. The air gap in the magnetic circuit was sized to accommodate all of the pump components as well as packaging. These analyses, along with the previously calculated estimates of cut-off magnetic flux densities, indicated that commercially available neodymium magnets (1.6 mm thick, K&J Magnetics) and magnetic circuits custom-made from low-carbon steel (1 mm thick) would provide sufficient magnetic flux for operation of the Penning cell arrays. In arrangements with streamlined packaging – such that the magnets could be located immediately outside the cathodes – neodymium magnets slightly less than 1 mm in thickness could be used. Reduction of the overall pump thickness – including electrode gap and anode length – could also dramatically lessen the required magnet thickness.

2.2.5 Sputtering Yield

In order for the pump to efficiently getter active gases like nitrogen and oxygen, fresh titanium must be exposed through the sputtering process. The sputtering yield – the number of target (titanium/titanium nitride/titanium oxide) atoms that are sputtered per impacting ion – indicates the efficiency of the sputtering process, and is determined by a number of factors including ion kinetic energy, ion mass, and impact angle. To a much lesser extent, the target material also affects the sputtering yield. For a simple Penning cell structure as described here, the pump designer and operator has influence on the sputtering yield mainly by affecting ion kinetic energy – through variations in electrode size and spacing, applied voltage, and operating pressures.

To estimate the variation in sputter yield for various pressures, cell geometries, and applied voltages, SIMION software (Scientific Instrument Services; Ringoes, New Jersey, USA) was used in conjunction with empirical curves for sputter yields versus ion impact energy. The focus of this analysis was to first evaluate how much energy the ions would lose as they traveled from the site of ionization to the site of cathode impact due to intermediate ion-neutral collisions. The distribution of impact energy was then used to calculate an average sputter yield.

To establish conditions for the SIMION analysis, in which the distribution of ion impact energies was estimated, a few simplifying assumptions were made. First, the plasma was assumed to be operating in a Penning discharge regime, as opposed to a glow discharge regime. The transition between the regimes can be estimated by Paschen's curves, which describe the voltage required for plasma ignition for a given pressure-gap product [Pas89]. For miniaturized SIPs with electrode gaps of less than 1 mm, the transition between a glow discharge (occurring between the parallel surfaces of the cathode and anode) and a Penning discharge (occurring within the cylinder of the Penning cell) is expected to take place below 6 Torr for nitrogen. The

second assumption was that the majority of initial ionization occurs at the mid-length of the anode cylinder, and near the cylindrical surface of the anode. This is where the electron kinetic energy is the highest, and this higher energy increases the probability of ionization resulting from an electron-neutral collision. The third assumption was that the distribution of the space charge in the plasma (from the spiraling electrons) does not substantially affect the electric potential distribution in the cell. Depending on the pressure, magnetic flux density, and anode voltage, the second and third assumptions will not be strictly correct, as the accumulation of space charge in certain portions of the cell can suppress the electric potential in that area and affect the location at which most ionizing collisions occur. The result of these simplifying assumptions is an underestimation of impact energy (and thus sputtering yield), as the combination of these assumptions results in the longest travel length for the ion from ionization to cathode impact, which will result in the largest number of energy-reducing ion-neutral collisions.

With the above assumptions, SIMION was used to model a large number of ion flights from ionization until impact. The software was first used to implement the 3D geometry of a single Penning cell. The electrostatic potential at all points of the cell was determined using the discretized Laplace equation. This potential was used, along with the Lorentz force equations previously described (discretized in time and space), to determine the stepwise ion trajectory. A hard sphere collision model (HS1) was used to determine the probability of and energy transfer due to an ion-neutral collision for each time step. Mean relative speeds, probability for collision, and gas velocities upon collision are calculated using Maxwell distributions that depend on the assigned pressure and background gas mass. Finally, the ion trajectory is followed until it collides with the cathode surface, and the impact energy is tabulated. The simulated gas is nitrogen (N_2) and ions are assigned a +1 elemental charge and zero initial kinetic energy. For

each geometry and pressure parameter set, the impact energies of 500 ion flights are tabulated. A typical result, showing the probability distribution of ion-cathode collision energy, is in Fig. 2-2.

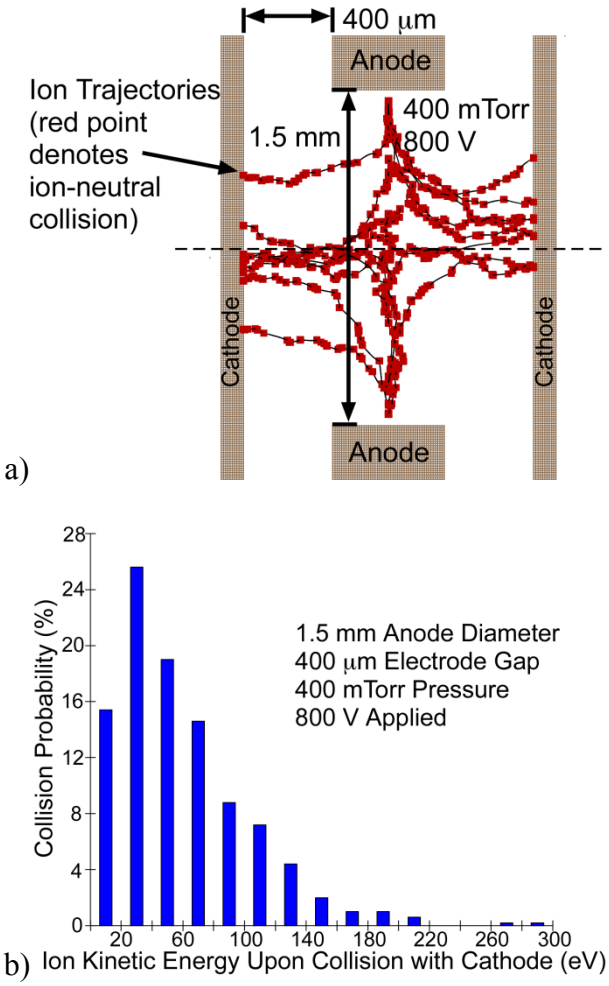

Figure 2-2: a) At relatively high pressures, ionized molecules will collide with other gas molecules and lose kinetic energy in transit to the cathode. To estimate the kinetic energy upon collision with the cathode, SIMION is used. b) Results from 500 ion flights show the expected distribution of ion kinetic energy upon impact with a cathode.

After estimating impact energy distribution, the expected sputter yield can be calculated by using a well known equation [Ohr92]:

$$S = \frac{\overline{E}}{E_t}\left\{1+\left(\frac{\ln \overline{E}/E_b}{\ln 2}\right)^{\frac{1}{2}}\right\}\sigma_0 n_A \qquad (2\text{-}2)$$

where $\overline{E}$ is the average of the threshold energy (E_t, 19.2 eV [Cle93]) required to displace the target atom and the energy transferred to the target atom (via momentum conservation) from the ion impact, E_b is the surface binding energy (4.89 eV [Shi72]) n_A is the number of target atoms per unit area, and σ_0 is the ion-target collision cross-section based on the Bohr radii and the atomic numbers of the two (1.273×10^{-16} cm^2). The average sputter yield estimated by this process for various selected situations is tabulated in Table 2-2. This procedure estimates that sputter yield is expected to be greatly diminished as pressure increases from 1 mTorr to 400 mTorr. The sputter yield is also expected to be proportional to the applied voltage. This analysis does not suggest a strong dependence on geometrical parameters such as anode diameter and electrode gap.

Table 2-2: (Simulated) Expected sputter yield S (atoms/ion) for various electrode gaps g (mm), anode diameters D_A (mm), applied voltages V_A (V), and pressures P (mTorr). Anode length was 1 mm for all cases.

g	D_A	V_A	P	S
1	1.5	800	400	0.049
1	1	800	400	0.055
0.4	1.5	800	400	0.079
0.4	1.5	800	100	0.260
0.4	1.5	800	1	0.989
0.4	1.5	400	400	0.039

2.3 Fabrication

2.3.1 Ceramic Base Architecture

The device base is machined using conventional milling from machinable ceramic (Macor). This is a low-outgassing material with good insulating properties. The base provides ledges on which the electrodes reside. Bases can be fabricated with different electrode gaps. Those reported here have electrode gaps of 400 µm or 1 mm. Cut-outs in the walls of the base allow electrode tabs and pins to extend outside the base to facilitate electrical connection after assembly.

The electrodes are patterned using photochemical machining [ASM 89]. This is a batch-compatible lithographic approach. Anodes with 1 mm and 1.5 mm diameters were patterned in 500 µm thick 304 stainless steel (Fig. 2-3). Cathodes were patterned in 150 µm thick commercially pure (98.9% or better) titanium (Fig. 2-3). Tabs and pins were included in order to facilitate electrical connection after assembly with the base.

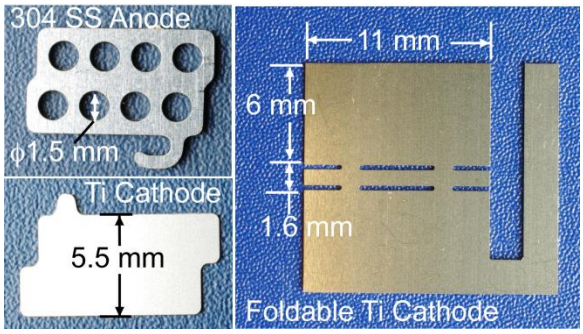

Figure 2-3: Stainless steel anodes (500 µm thick) and titanium cathodes (150 µm thick) used in the devices, with important dimensions. Anodes with various cell diameters were fabricated. Depending on the anode cell diameter, more or fewer cells are placed in the same footprint as shown here.

The titanium surfaces of the cathodes tend to tightly adsorb gases and water vapor – molecules which are difficult to desorb by baking or by time under vacuum. The initial sputtering action, however, typically provides enough energy to desorb a significant number of these molecules – an undesirable situation, as this causes the package pressure to initially rise and reduce the efficiency of the pump. To limit the adsorption of gases and water vapor on the surfaces of the cathodes that are to be sputtered, a thin layer of Cr/Ti/Pt (100 nm/1.5 µm/100 nm) is deposited on these surfaces using an evaporation process. The platinum is intended to passivate the titanium surface and less tightly adsorbs water vapor when exposed to the atmosphere [Har 76]; this layer must be sputtered through to reach the underlying thin-film and bulk titanium.

a)

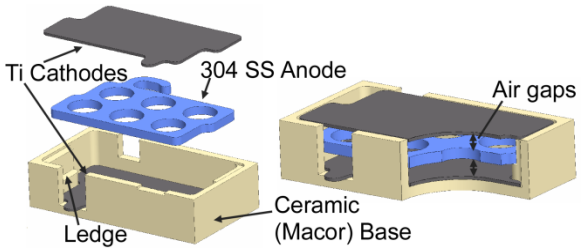

b)

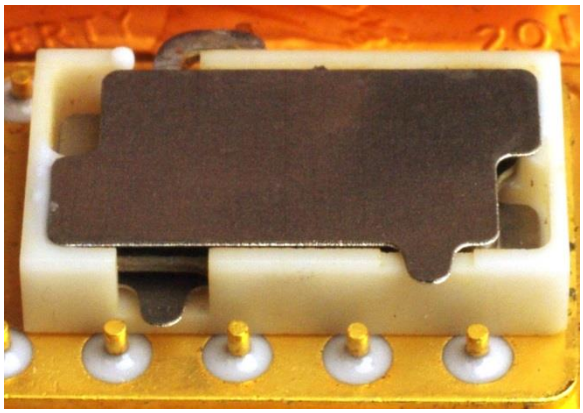

Figure 2-4: a) Penning cell array device consisting of a stainless steel anode with multiple holes, stacked between two titanium cathodes in a ceramic base. b) An assembled device, prior to wirebonding, on the platform of a commercial package.

The electrodes are stacked in the base and fixed in place with a vacuum epoxy (Loctite Hysol 1C, cured for 20 minutes at 80^{o}C). The epoxy is located only on the interface between the ledges of the ceramic base and the corresponding electrode features to ensure that the metal surfaces are maximally exposed to the incident ions and sputtered titanium. The device is then placed in a 12-pin power electronics package (Sinclair Mfg. Co.), and fixed in place with more vacuum epoxy. The package has 2.5 mm thick nickel walls and a 1.6 mm thick copper bottom, is 25 mm square (outside dimensions), and has a cavity depth of 4.8 mm. The anode is soldered to a package pin using fluxless tin solder and an appropriate flux for stainless steel soldering. To ensure full removal of the flux after soldering, the package and device is swabbed successively with acetone, isopropyl alcohol, and deionized water, then baked briefly at 100^{o}C to volatilize any residue. Assembled package is shown in Fig. 2-4. The titanium cathodes are connected to package pins electrically with wirebonds. The package is sealed by affixing a glass slide with

vacuum epoxy.

The magnets and magnetic circuit are arranged outside of the package to facilitate interchange of various magnet sizes. The magnetic circuit is fashioned from plates of 1.5 mm thick 1010 alloy steel. Neodymium magnets with 18 mm diameters and thicknesses of 0.8 mm and 1.6 mm (K&J Magnetics) provide flux to the packaged components (Fig. 2-5).

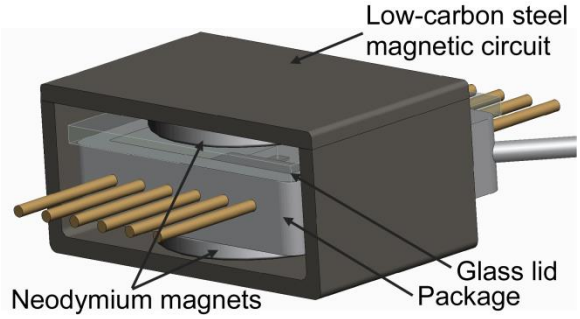

Figure 2-5: Magnetic flux is provided to the packaged components using external magnets and a magnetic circuit composed of 1.5 mm thick low carbon (1010 alloy) steel.

2.3.2 Folded Cathode Architecture

An alternative architecture that facilitated prototyping without the ceramic base in this specific electronic package is also used for testing (Figs. 2-4 and 2-6). In this architecture, the cathode pair is formed from one continuous piece of titanium with two integrated bending hinges and a sidewall defining the overall gap between the cathodes. The anode is soldered to a package pin; this connection is sufficiently robust mechanically to suspend the anode. The cathode is then folded into a "sandwich" manually using a precision-fabricated plate of the desired thickness as a form. Because the integrated bending hinges are plastically deformed, there is minimal snapback of the cathode plates from the shape of the form. Estimated non-parallelism of the cathode plates is much less than 1 degree, which should have a minimal effect on pump performance. The folded cathode is then placed around the anode, and fixed in place with vacuum epoxy. The cathode is connected electrically to a single package pin with a wirebond.

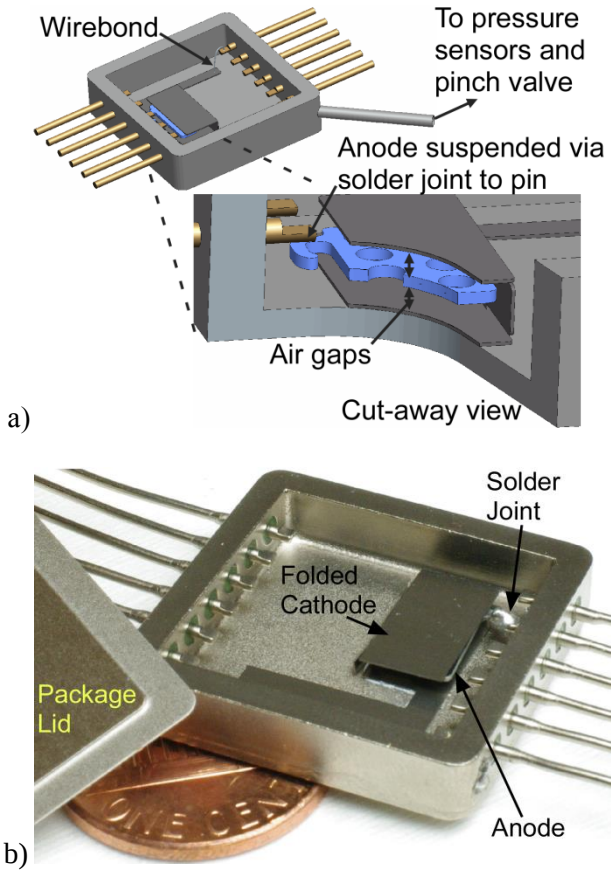

Figure 2-6: a) In a preliminary test structure, the anode is suspended within a single folded cathode by rigidly fixing the anode to a package pin. b) An assembled preliminary test structure, prior to wirebonding, inside a commercial power electronics package (Sinclair Manufacturing).

2.4 Experimental Setup

A schematic of the experimental setup is shown in Fig. 2-7. A high-voltage supply (Acopian, model P05HP12) was used to provide DC high voltage between the anode and cathodes. To limit the plasma current, a 2 MΩ ballast resistor was placed in series before the electrodes. To assess the ion current, a 100 Ω resistor was placed in series after the electrodes, and the voltage measured across the resistor was converted to current. The voltage across the SIP was measured using a high voltage probe.

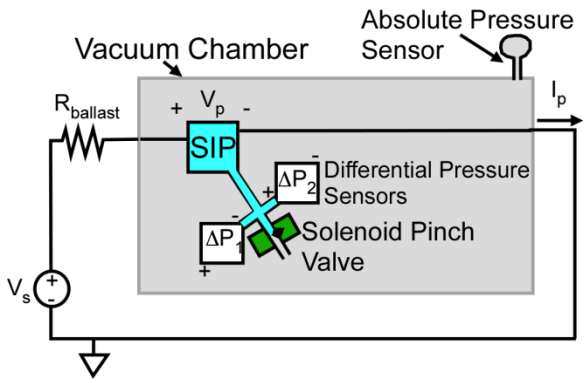

Figure 2-7: Experimental setup. The vacuum chamber is used to regulate the starting pressure inside the device package, and the solenoid pinch valve limits the pumped volume to ~2.5 cm^3. Two differential pressure sensors are used to measure the package pressure; each is attached with opposite polarity in order to fully measure both positive and negative pressure differentials. Probes are attached to measure plasma voltage (V_p) and plasma current (I_p).

In order to modulate the pressure inside the package for purposes of characterizing the Pirani gage and evaluate the pump characteristics at various starting pressures, a steel tube (~2 cm length) was added as an outlet to the package. This tube was then connected with Tygon tubing to two commercial differential pressure sensors (Freescale MPXV4006DP) and a solenoid-actuated, normally-open pinch valve (Cole Parmer). The total volume of the package and tubing was ~2.5 cm^3. The setup was then placed in a vacuum chamber equipped with an absolute pressure sensor (Adixen AHC2010). In conjunction with actuation of the pinch valve, the vacuum chamber was used to set the package pressure. Prior to testing and closure of the pinch valve, the device was held at the desired starting pressure for 12-24 hours to ensure sufficient degassing of the internal package surfaces. In order to minimize the pressure differential (and thus leakage) between the inside and outside of the package during testing, the vacuum chamber was maintained throughout the test at the desired starting pressure. A typical leakage resistance for the package, tubing, and valve is 40 Torr-nL/s/Torr, as measured by shutting the pinch valve prior to reaching full vacuum in the chamber and monitoring the package pressure. In all experiments, lab air was used as the pumped gas.

The pressure inside the package was monitored continuously with the combination of the absolute pressure sensor and the commercial differential pressure sensors. During the course of testing, it was found that the commercial differential pressure sensors lacked sensitivity as the absolute pressure on either side of the pressure sensor dipped below 200 mTorr (26.7 Pa). The differential sensors remain viable and were utilized in tests above this pressure. As a third measure of package pressure, the sensitivity of the ion current through the SIP to pressure for a given applied voltage was studied. This is a technique used by macro-scale SIPs, and in those pumps can provide good linearity and sensitivity down to the nanoTorr regime [Wel01, Sak94].

2.4.1 Minimum Operating Pressure and Cut-Off Flux

To establish the minimum pressure at which a plasma could be ignited and the associated flux density – the cut-off flux density – required to efficiently contain the electrons and enable plasma ignition at very low pressures, the solenoid pinch valve was left open and the pressure inside the package was modulated with the vacuum chamber. The magnetic flux density inside the package was applied with the external magnetic circuit, and was measured with a gaussmeter (F.W. Bell, model 5100). At different combinations of pressure and magnetic flux density, the breakdown voltage required to ignite a plasma (i.e., to generate ion current) was evaluated. A typical result – in this case, for a device with details as described by entry "C" in Table 2-1 – is shown in Fig. 2-8. Without a magnetic field applied to the device, the breakdown voltage began to increase rapidly as pressure was reduced to 1 Torr (133.3 Pa); a voltage of 1 kV was insufficient for igniting a plasma below 1 Torr (133.3 Pa). This pressure limit was similar to that of other (not reported) non-Penning-cell architectures. With a magnetic flux density of 0.25 T applied, the breakdown voltage remained low (~510 V) even as the pressure was reduced to 100 mTorr (13.3 Pa). With an applied magnetic flux density of about 0.3 T, the plasma could also be ignited at 1.5 μTorr (0.2 mPa) – which is near the base pressure achievable by the vacuum

chamber – with an applied voltage of 1.5 kV. Based on these results, the cut-off flux density is estimated to be ~0.3 T, which agrees well with the theoretical estimate.

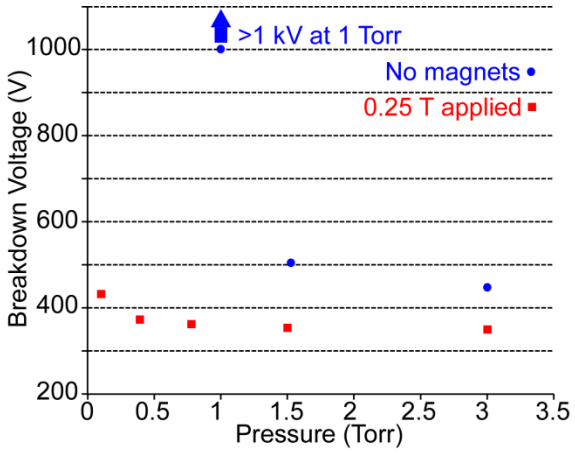

Figure 2-8: In the absence of a magnetic field, the breakdown voltage of the device increases rapidly when pressures drop below ~1 Torr. With a measured magnetic flux density of 0.25 T, the breakdown voltage remains low below 100 mTorr.

2.4.2 Pump Operation

In a typical result, with device details as described by entry "C" in Table 2-1 and with a starting pressure of 115 mTorr (15.3 Pa), the chip-scale SIP is able to evacuate the package volume to below 10 mTorr (1.33 Pa) over a period of about 4 hours (Fig. 2-9). The applied voltage (across the SIP and the ballast resistance) was held constant at 1 kV; the plasma voltage during this operation ranged from 450 V to 600 V, with higher voltages occurring at lower pressures. This indicates that the plasma resistance is higher at lower pressures, likely a result of less frequent ionization events. The power dissipated across the SIP ranged from 100 mW to 250 mW, again depending on the operating pressure.

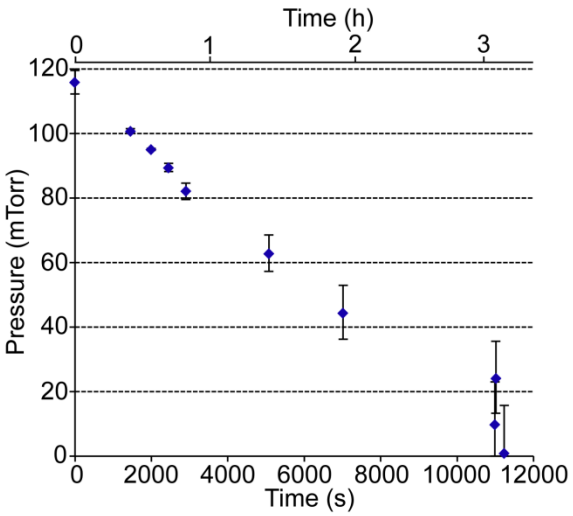

Figure 2-9: Using ion current as a measure of pressure, the chip-scale SIP is shown to pump from ≈115 mTorr down to <10 mTorr. The pumping rate over this time period is 0.027 Torr-µL/s. Not shown in this chart is the ~5 hours of operation when the pumping rate is much lower as the gases initially adsorbed on the electrode surfaces are degassed by the plasma.

The pressure data shown in Fig. 2-9 is not from the Freescale MPXV4006DP differential pressure sensors, as these sensors are not sufficiently sensitive in this absolute pressure range. Instead, the ion current through the SIP is used as an indicator of package pressure. The relationship between ion current and package pressure is determined before and after pump operation by using the vacuum chamber to modulate the pressure and applying the same 1 kV voltage across the SIP and ballast resistance (Fig. 2-10). The resulting calibration curve is used to calculate the pressure during pump operation as given in Fig. 2-9.

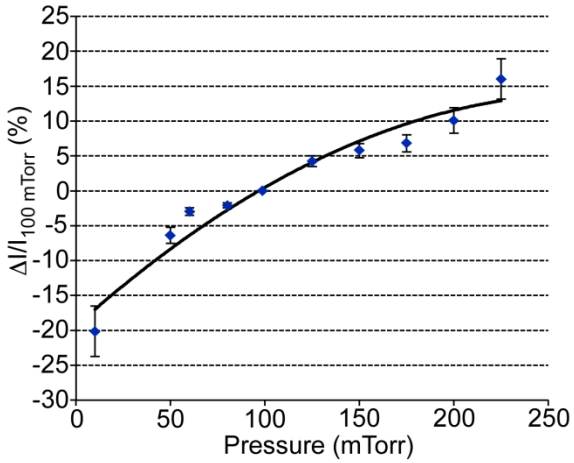

Figure 2-10: Calibration curve for differential ion current versus pressure, used in determining the pumping results shown in Fig. 2-9. The ion current at 100 mTorr (150 µA) is used as a normalization standard, and the percentage difference from this value is used as the measurand. The error bars in this chart and in Fig. 2-9 illustrate the difference in the calibration curve before and after pump operation.

The preliminary prototype structure is used to investigate operation at higher pressures. In a typical result, with device details as described by entry "B" in Table 2-1 and with a starting pressure of 1 Torr (133.3 Pa), the pump is able to evacuate the package to below 200 mTorr (26.7 Pa) over the course of about 10 hours (Fig. 2-11). The pressure inside the package is actually above the starting pressure for a significant portion of this pump down time. Above and near 1 Torr (133.3 Pa), the pumping rate is relatively low. The rate significantly increases once the pressure reaches about 800 mTorr (106.6 Pa). This is discussed in more detail in the subsequent section. During pump operation, the voltage across the device varied from 280 V at the highest pressures to about 600 V at the lowest pressures. Power dissipated was typically 100-200 mW, again depending on pressure.

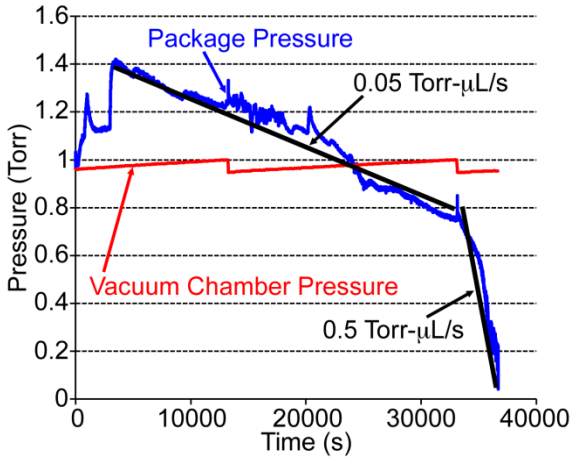

Figure 2-11: The preliminary test structure is used to illustrate that a SIP of this size can start pumping at 1 Torr. An initial period of slow pumping due to plasma-induced surface desorption can be seen. This is followed by rapid pumping down to ~200 mTorr, which is found to be the sensitivity limit for the differential pressure sensors used in this work.

2.5 Discussion

The start-up period of the pump operation provides some interesting pressure and electrical characteristics. As shown in Fig. 2-11 – and also present but not shown in the pump operation detailed in Fig. 2-9 – the start-up period (i.e. the period of time immediately after creating a plasma current through the pump) is characterized by an increase in pressure inside the package followed by a very slow pressure reduction. This pressure increase occurs only upon starting the plasma, and does not occur when simply closing the solenoid pinch valve (i.e. outgassing upon closing the solenoid pinch valve is negligible due to sufficiently long exposure to the starting vacuum pressure). Electrically, the voltage across the plasma is relatively low. An increase in applied voltage across the device and the ballast resistance does not significantly increase the plasma voltage; however, this action does significantly increase plasma current and tends to also increase the package pressure. This situation is exhibited in the "spikes" in package pressure shown in Fig. 2-11, which are concurrent with manual increases in applied voltage. As the package pressure increases, the plasma current tends to increase further, indicating a reduced

plasma resistance. Eventually, if the applied voltage is increased only when there is a concurrent increase in plasma voltage, then the package pressure can be slowly reduced. Once the voltage across the plasma reaches a sufficiently high level, then the pumping rate increases substantially. A likely explanation for this combines the insight gained from the sputtering yield analysis presented earlier with an understanding of plasma surface cleaning [Gam13, Kan74]. When the plasma is initially started, the surfaces that are being impacted by ions have a large number of adsorbed molecules – molecules such as water vapor that are tightly adhered and thus have not outgassed by simply being exposed to vacuum for a long period of time. The impacting ions, however, have sufficient energy to cause these molecules to desorb and enter the gas phase in the package. As shown in Table 2-2, at higher operating pressures and lower plasma voltages (as experienced at start-up), the ions have a very low sputtering yield. Thus, many gas molecules are being desorbed and only a few getter molecules are being exposed – leading to an increase in package pressure. This increase in package pressure further reduces the sputtering yield. Once a large portion of the molecules are desorbed, the gettering process can begin to dominate – reducing the package pressure, increasing the plasma voltage (and sputtering yield), and eventually increasing the pumping rate.

Future efforts may be aimed at overcoming the prolonged start-up periods described above. Macro-scale SIPs also face challenges in "high-pressure" startup, and typically overcome such challenges with appropriate power supply controllers and interlock systems that shut down the SIP when the pressure is too high (e.g. [Gam13]). For a chip-scale SIP, similar control systems could be implemented. Other likely solutions to the prolonged start-up period would center on increasing the plasma resistance at the starting pressures, such that the plasma voltage can be high at start-up. This would result in ions with sufficient kinetic energy to increase sputtering

yield at start-up and better combat the plasma-induced desorption. Plasma resistance could be increased by minimizing active electrode areas or decreasing the electrode gap, among other approaches. Other future efforts in this area may include batch-fabrication and further miniaturization of the pump. In addition, a fabrication process that could accommodate monolithic integration of the pump architecture with the devices that require vacuum packaging may enable extreme system miniaturization.

Chapter 3: Microdischarge Based Neutron Detectors

3.1 Introduction

In this chapter, use of microdischarges with the application to radiation detectors is discussed. There are currently different types of radiation detectors available using various mechanisms to detect radiation. A summary and brief explanation of these detectors is provided. This is followed by the particular detection mechanism of the fabricated detectors, fabrication method and experimental results.

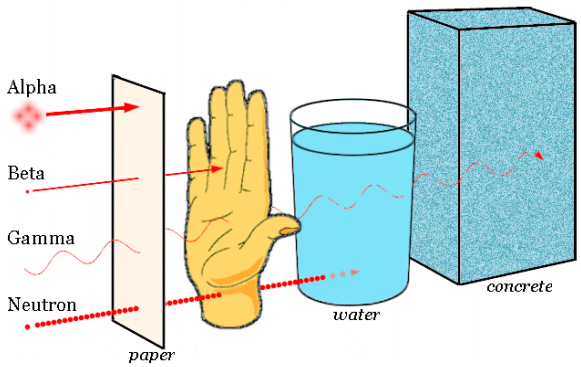

Figure 3-1: Different types of radiation and their penetration depth. Neutrons are the radiation particles of interest [Pen13].

3.1 Types of Radiation

There are four main types of radiation, which have varying depths of penetration: alpha particles, beta particles, gamma rays, and neutrons (Fig. 3-1). Alpha particles consist of two protons and two neutrons bound together to form a helium nucleus, α^{2+}. Generally, the higher the charge, the faster a particle loses its energy, which is why alpha radiation have the shortest range. Beta particles are essentially high energy electrons that can travel distance of meters in air, but are very easily blocked by a solid material. Gamma rays are electro magnetic waves that have a very high penetration depth and their attenuation is largely proportional to atomic number, Z, of the blocking material. Neutrons, being neutral in charge, unaffected by electric fields and tend to pass through most materials,

3.2 Radiation Detection

There are primarily three types of radiation detectors that are commercially available: scintillators, solid-state and gas based detectors. Scintillators convert incident radiation into visible light photons which are then converted into electrical signals through use of a photomultiplier tube or reverse biased photodiode. In recent years, scintillation methods have seen marked improvements through micro fabrication technologies. For instance, certain scintillators are directly deposited onto thin film silicon-well photo detectors for gamma and neutron imaging [All00, All01]. The main advantages of scintillator technology lie in their relatively fast response time and good interaction probability with high energy gamma radiation [Kno07]. However, the scintillator crystal themselves are bulky, along with the need for a photomultiplier tube and high power requirements.

For the remaining two classes of radiation detectors, the incident radioactive particle ionizes the fill gas in a gas detector or creates electron-hole pairs in a semiconductor detector and the charges are collected at the respective electrodes resulting in a current pulse. This architecture works well for detection of charged particles like alpha radioactivity or beta particles/fast electrons because the particle's energy is directly deposited in the detector to produce ion-electron pairs.

The detection of electromagnetic radiation like X-rays and gamma rays can only be done indirectly by ejecting photoelectrons from the electrodes through the photoelectric effect or Compton scattering [Kno07]. These ejected photoelectrons are akin to fast electrons/beta particles having a fraction of the energy of electromagnetic radiation (X-rays or gamma), directly depositing that energy in the detector to form ion-electron pairs. The probability of interaction of

a gamma ray with a material to produce the fast electrons increases with its atomic number, *Z*, and its thickness.

Detectors utilizing semiconductor material achieve the highest energy resolution [Aud90, Kem87, Wad87]. However, some semiconductor detectors, like the ones using germanium crystal, require cryogenic cooling to maintain high signal-to-noise ratio [Kno07]. The latest solid-state detector technologies use wide band gap, high-Z materials such as CdZnTe which offers high conversion efficiency, and operates at room temperature [Leh03]. However, these semiconductor crystals are expensive, bulky, and require complex interface circuits which limits their usage to only the most critical and high performance applications [MTI13].

Gas-based detectors are often favored for environmental surveillance efforts (e.g. looking for radiation leaks and contamination). They are relatively simple and robust, operate over a large temperature range, and measure a wide range of radiation species and energies. As mentioned previously, a voltage bias is applied between two electrodes (anode and cathode) within a gas-filled chamber. Electron and ion pairs which are formed by the interaction of gas molecules with the radiation can be detected in one of four regions shown in Fig. 3-2.

In the ion saturation regime, electrodes collect the charges created by each interaction between the incident radiation and the gas. There is no charge multiplication of the original ion electrons pairs. This results in a limited signal amplitude, comparable to the noise floor. To make up for limited signal, the detectors working in this regime are large (about 1 m^3 in volume) to ensure maximum interaction of radiation with the gas, thus maximizing the number of ion-electron pairs formed.

The detectors that work in the proportional regime use charge amplification by using higher electric fields (compared to detectors in the ion-saturation regime) to multiply the original number of ion-electron pairs before they are collected by their respective electrodes. The ion-electron pairs are formed by incident radiation directly transferring energy to the gas. The multiplication is proportional to the energy deposited in the detector, resulting in a proportional current pulse amplitude which can then be used for energy spectroscopy of the incident radiation. Despite the inherent charge amplification by detectors working in this regime, external amplification is still needed to resolve the received signal, making the interface circuit design somewhat complex or at the very least bulky. Usually, a charge-to-voltage converter is used for resolving spectral information [Kno07].

If the voltage − and thus, the electric field − is raised even higher, the detector approaches the Geiger-Muller regime of operation, in which discharges are created until the entire anode is enveloped in an ion-electron cloud. After the initial formation of ion-electron pairs through interaction with radiation, electrons drift towards the anode, which has an even higher electric field, compared to the proportional regime. This results in ionization collisions which lead to greater charge multiplication. The charge multiplication itself is sufficient to eliminate the need for external amplification, making the interface circuit simple. However, due to the large number of ion-electron pairs created for each detection event, the current pulse amplitude is the same regardless of incident radiation energy. Thus, no energy information about the incident radiation can be retained and this regime can only be used for radiation particle counting. Since gamma rays have a very high penetration depth and rarely deposit their entire energy in a gas-based detector, detectors operating in G-M regime provide a good solution for gamma detection. In principle, only one ejected electron is needed to start the discharge. Therefore, as long as a

gamma ray can eject one photoelectron from the electrode or create an electron-ion pair through direct interaction with gas, a current pulse/count will be observed. By leveraging micromachining technologies, a single and multi-stack electrode gamma radiation detector operating in the G-M regime was fabricated which was inherently capable of wireless signaling in the ultra wideband (UWB) [Eun10, Eun11].

Detection of the last category of radiation, the neutrons, is the most difficult due to their long penetration depths. However, neutrons and their detection have gained increasing importance for homeland security purposes because the presence of neutrons can be an indicator of special nuclear materials (SNMs). SNMs are fissile materials, including highly enriched uranium and plutonium that can potentially be used in a nuclear weapon. The following section discusses the state of the art in neutron detection along with the proposed solution for a microfabricated device with increased neutron sensitivity.

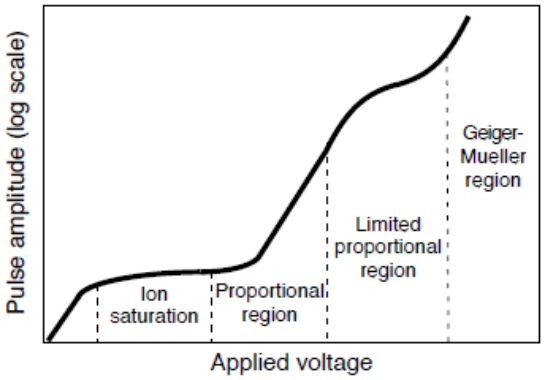

Figure 3-2: Gas-based radiation detectors have four regimes of operation that are defined by applied voltage.

3.3 Neutron Detectors

Neutrons can be categorized by energy. Fast neutrons have energies greater than 100 keV, whereas slow (thermal) neutrons have energies near 0.025 eV. Thermal neutrons, upon

interacting with certain materials, can produce charged particles (alpha, beta) or gamma raysm which are detected. This is called the 'conversion' of the neutrons into detectable forms of radiation through nuclear interactions.

Gas-based neutron radiation detectors are coated (if the conversion material is solid) or filled (if the conversion material is gas) with materials which have a high conversion cross section for thermal neutrons. Charged particles or gamma rays produced as a result of neutron conversion, transfer energy to the gas by formation of electron-ion pairs, which in turn are swept by the applied bias to the respective electrodes. By operating these detectors in the G-M regime, a high electric field region present at the anode creates an avalanche of electron-ion pairs amplifying the original discharge without a need for complex electronics. Gas-based detectors offer the advantage of simple electronic interfaces, insensitivity to temperature changes and mechanical robustness.

Neutron conversion material for conventional gas-based detectors has been limited to ^{3}He-filled [Lea66, Lea68], BF_3-filled [Sto66, Han47], and ^{10}B-lined [Lin09] and ^{6}Li coatings [Vei04, Eng04]. Gas-based neutron detectors operating in the proportional regime utilizing ^{3}He have been the most widely used for neutron detection because of its high neutron sensitivity, as it has a capture cross section of 5330 barns (1 barn=10^{-24} cm^2). The neutron interaction produces a proton and a tritium particle. However, there is a world-wide shortage of ^{3}He because of reduction and discontinuation of the nuclear weapons program, as it is a by-product of nuclear weapons maintenance [Ely10]. Additionally, ^{3}He detectors require high encapsulation pressures (5-10 atm) and require high biasing voltages (1 kV-2 kV) [GE13]. Detectors that use BF_3 as fill gas convert thermal neutrons to produce alpha particles and $^{7}Li^{+}$ ions. One drawback to BF_3 detectors is inherently lower neutron sensitivity because of lower interaction cross section

[Sto66, Yam66, Bro74]. Also, BF_3 is toxic and poses a health hazard if released [Che13] . Boron-lined (^{10}B) detectors use a thin-film (1-2 μm thick) coating of highly-enriched (95-98%) ^{10}B on the inside of a metal tube. The detection efficiencies tend to be lower (compared to ^{3}He and BF_3) because the neutron interaction is limited to the inner surface of the tube [Ely10]. Detectors using ^{6}Li convert neutrons to high energy alpha radiation. This isotope is present 7.40% by weight in naturally occurring Li and is readily available in separated form. However, the neutron conversion cross section of ^{6}Li at 904 barns, is the lowest among the candidate materials, limiting the detector sensitivity [Kno07].

Table 3-1: Comparison of various conversion materials for thermal neutrons.

Converter material	Particle emitted by neutron	Energy (MeV)	Thermal neutron cross section (barns)	Attenuation Coefficient (cm^{-1})
^{3}He	proton	0.573	5330	616.3
^{6}Li	alpha	2.05	940	43.7
^{10}B	alpha	1.47	3840	444
Gd-sputtered	gammas x-rays electrons	γ < 2MeV x-rays = 44-80 keV β = 72 keV	48,890	1548.22
^{157}Gd	gammas x-rays electrons	γ < 2MeV x-rays = 44-80 keV β = 72 keV	255,000	7921.1

Finally, the material of choice for the fabricated detector, ^{157}Gd as a conversion material is attractive because of its extremely high conversion cross section of 255,000 barns − amongst the highest nuclear cross sections found in any candidate material [Kno07, BNL13]. The isotope is present 15.7% by weight in naturally occurring Gd. Neutron conversion results in an assortment of reaction products that include gamma rays and beta particles. These range of products are particularly useful to the current device architecture which operates in the G-M regime: gamma

rays can eject a photoelectron from the electrode and beta particles can directly interact with the fill gas to deposit their energy. Table 3-1 lists a comparison of various converter materials.o

The next sections describe the operation of gas-based neutron detector operating in the G-M regime using a stack of micromachined Gd-coated cathodes. Section 3.4 describes the detector structure and operation. Section 3.5 details the fabrication and assembly process followed by section 3.6 which details the experimental results.

3.4 Design Concept and Operation

3.4.1 Detector structure

A schematic representation of the detector is shown in Fig. 3-3. The detector structure includes a stacked set of stainless steel 304 (SS 304) electrodes and insulating spacers that are placed in an Argon environment at atmospheric pressure. A spacer insulates the package base from the SS 304 elements. The middle electrode is a perforated anode, sandwiched between two solid (unperforated), Gd-coated cathodes. The package pins were used for lead transfer through the package and also within the stack, and serve the additional purpose of providing alignment for detector assembly. During device operation, thermal neutrons interact with the ^{157}Gd sputtered on the SS 304 cathodes and produces fast electrons (39% of the time) and gamma rays. The fast electrons have a characteristic energy of 72 keV and generate electron-ion pairs as they pass through the electric field region. The electrons that are produced travel to the high electric field region near the perforations, where they initiate current-driven avalanche pulses between the biased electrodes.

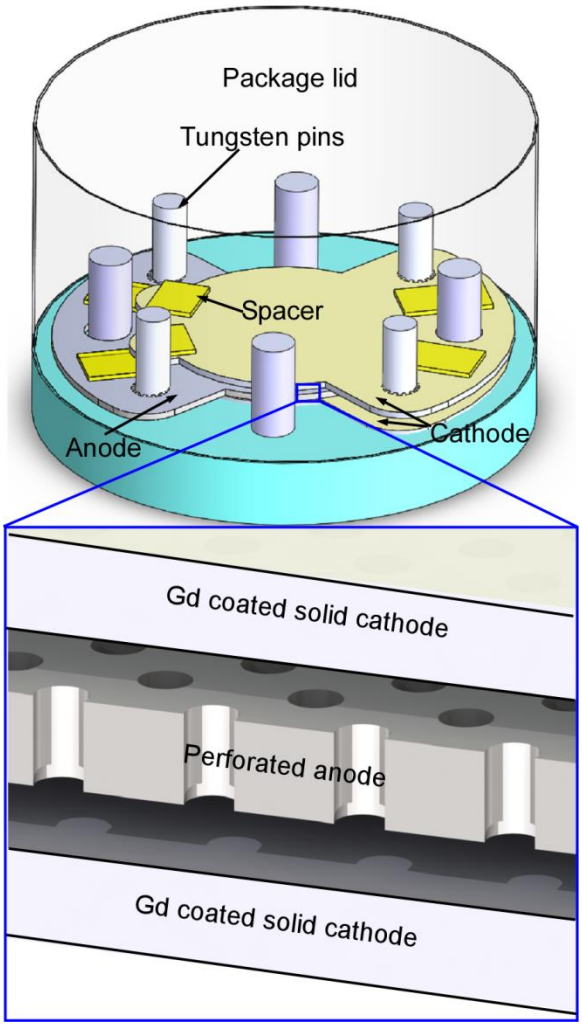

Figure 3-3: Device concept. A stacked arrangement of solid cathodes and a perforated anode separated by spacer. PMMA used for neutron moderation.

3.4.2 Electric field

The selected detector architecture should provide sites of high electric field which facilitate avalanche amplification of microdischarge. Electric field strengths on the order of 4-5 MV m^{-1} (for Ar at 760 Torr) are necessary for avalanches [Kno07]. Additionally, the electric field near the cathode should be minimized so that Ar^{+} ions do not gain enough energy through the electric field to release secondary electrons from the cathode. This would further create electron avalanches, the source of which is not the incident radiation. A perforated anode is used because the perforations provide sites of electric field concentration for charge amplification.

Solid cathodes sustain lower electric fields than anodes, thereby reducing spurious discharges. The solid surface also provides greater area coverage of the Gd layer and thereby enhances neutron sensitivity. After neutron conversion, as the fast electron and gamma rays travel through the fill gas, electron-ion pairs are formed and separated by the electric field. The initial charge is amplified through multiple collisions as the electrons approach the high field regions close to the anode.

Finite element analysis (FEA) of the electrode configuration show that with a 70 µm gap and a bias level of 300 V, the electric field at various locations within the structure is between 5 and 6 MV/m, this is sufficient for creating avalanche discharge (Fig. 3-4). The analysis predicts high field regions near the edges of the perforation and low electric field regions in the center of the perforations and near the cathode, as expected. The FEA was performed with COMSOL 3.5a

a)

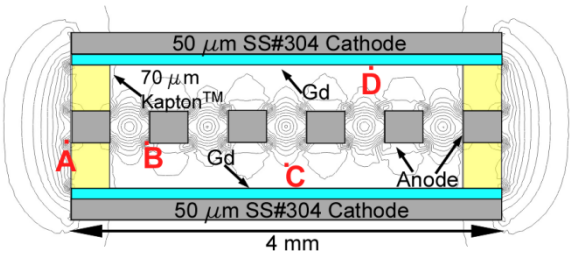

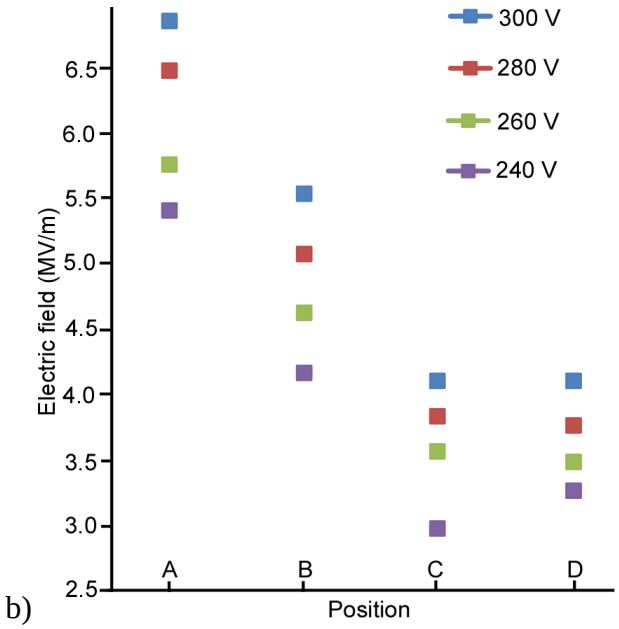

b)

Figure 3-4: Electric field modeling using COMSOL 3.5a. a) A cross-section of the 2D model. b) The generated electric fields range from 2.5-4 MV/ m (i.e. close to the cathode) to 4-6.8 MV/m (i.e. near the perforation and anode edges).

3.4.3 Neutron conversion

Neutron interactions with matter can be mainly of two types, scattering or conversion. Scattering results in change of energy or direction of the neutron but does not directly result in its disappearance. Conversion leads to disappearance of a free neutron as a result of nuclear reaction with fission or the formation of a new nucleus and/or particles such as alpha, beta particles or gamma rays.

The probability of any of these reactions is dependent on the energy of neutrons and properties of the nucleus itself and can be conveniently expressed in cross section data. They are evaluated as a function of neutron energy given in eV or MeV. The sum of reactions which can lead to disappearance of a neutron can be designated as conversion cross section:

$$\sigma_c = \sigma_\gamma + \sigma_f + \sigma_p + \sigma_T + \sigma_\alpha \qquad (3\text{-}1)$$

where σ_γ is gamma conversion cross section (cm^2), σ_f is fission cross section (cm^2), σ_p is (n, proton) reaction cross section (cm^2), σ_T is (n, tritium) reaction cross section (cm^2), σ_α is (n, alpha particle) reaction cross section (cm^2).

For a material like ^{157}Gd, the gamma conversion section, σ_γ, is high for thermal neutrons (0.025 eV) and is shown in Fig. 3-5 [Fie 57]. Thus ^{157}Gd can be used for converting thermal neutrons, releasing gamma rays and fast electrons which can be further used by the G-M detector to produce current avalanche and result in detection events. Using the conversion cross section σ_c, it is possible to calculate the neutron linear attenuation co-efficient, also known as the macroscopic cross section denoted by Σ and atomic number density by N [Kno07].

$$\Sigma = N\,\sigma_c\,[cm^{-1}] \qquad (3\text{-}2)$$

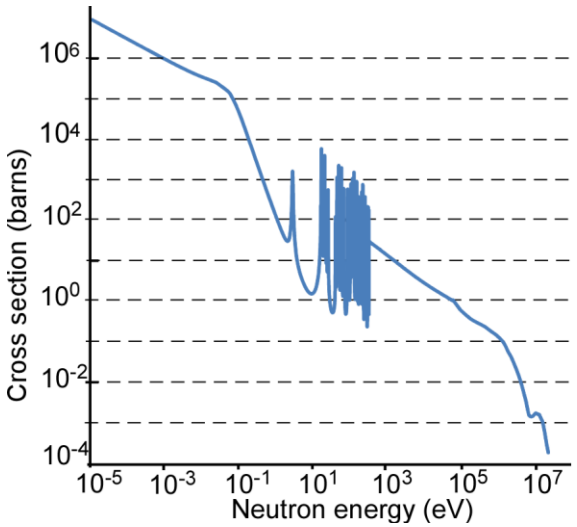

Figure 3-5: Neutron interaction cross section for Gd as a function of neutron energy. (1 barn=10^{-24} cm^2).

Once the thermal neutrons have been converted into a gamma ray or fast electron they can be detected by the Geiger counter as described previously. Fast electrons directly ionize the fill gas resulting in a current avalanche, while gamma rays interact with the cathode material through Compton scattering or the photoelectric effect.

The intensity of neutron radiation is described by [Kno07]:

$$I = I_0 e^{-\Sigma t} \tag{3-3}$$

where I is the number of transmitted photons, I_0 is the original number of photons, Σ is the linear attenuation coefficient (cm^{-1}) of the absorber dependent on neutron energy in MeV, and t (cm) is the thickness of the absorber material. Since the attenuation co-efficient of Gd depends on the incident neutron energy, which is not necessarily thermalized, the intrinsic conversion efficiency of the material, ε_{int}, is defined as the percentage of radiation incident on the detector that results in conversion of neutrons into daughter gamma rays and fast electrons [Kno07]. Assuming a point isotropic source of activity, A (Ci), a source-detector distance, d_1 (m), a detector surface area (i.e. facing the direction of source), S_D (m^2), and the number of transmitted photons, I, then ε_{int} can be rewritten as:

$$\varepsilon_{int} = \frac{I}{A \cdot 3.7 \times 10^{10} . \frac{S_D}{4\pi d_1^2}} \times 100 \tag{3-4}$$

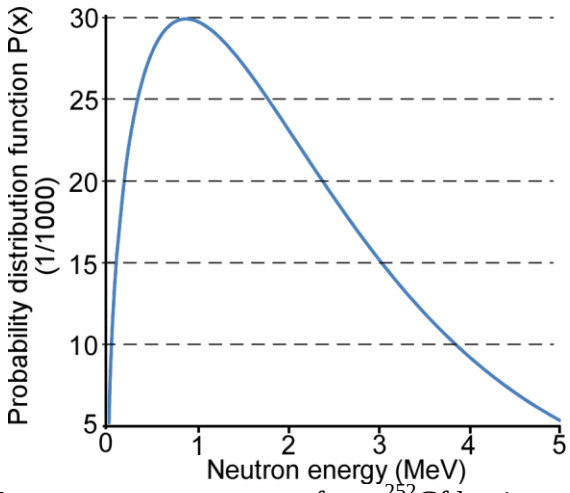

Figure 3-6: (Calculated) Neutron energy spectrum from ^{252}Cf having a mean energy of 0.7 MeV with the most probable energy of 1.1 MeV [Fie57].

3.4.4 Neutron moderation

Since the neutron source, ^{252}Cf has a neutron energy spectrum that spans from 0 to 5 MeV as shown in Fig. 3-6 [Fie57]. Since the interaction of ^{157}Gd with neutrons is highly dependent on neutron energy, it is important to moderate neutron energies to approach thermal levels. Neutron moderation can be performed using materials that have a high density of hydrogen. The mass of a single neutron is close to the mass of hydrogen nucleus, it is possible for neutron to lose all of its energy through elastic collision. More realistically, it is necessary to take into account head-on and glancing collisions. The mean logarithmic reduction of neutron energy per collision, ξ, depends only on the atomic mass, M, of the nucleus as given by [Kno07]:

$$\xi = \ln\frac{E_0}{E} = 1 + \frac{(M-1)^2}{2M}\ln\frac{(M-1)}{(M+1)} \qquad (3\text{-}5)$$

This shows that by using a hydrogen-rich material ($M \approx 1$ amu) like a polymer, it is possible to moderate the neutron energies which in turn will increase the conversion cross section. As shown in Fig. 3-7, the total neutron counts increased with an increasing Polymethylmethacrylate (PMMA) thickness. Additionally presented is the percentage attenuation by a 2.1 μm thick Gd coated on 50 μm thick SS 304 shim. By moderating the neutron energy with PMMA, the conversion cross section of a ^{3}He detector was increasing, and so was the interaction with Gd which resulted in appreciable conversion of neutrons into fast electrons and gamma rays. Since the proportional counter was not sensitive to detection of fast electrons and gamma rays [Kno07], coupled with higher conversion cross section of Gd, there was a drop in the total neutron count with increasing PMMA thickness. Neutron counts dropped by as much as 12.5% with only a 2.1 μm thick Gd in the presence of 49 mm thick PMMA. The measurements in this assessment were done using Reuter Stokes ^{3}He Proportional counter to provide a theoretical

reference for expected percentage neutron detection with increasing PMMA thickness and the resulting conversion by Gd.

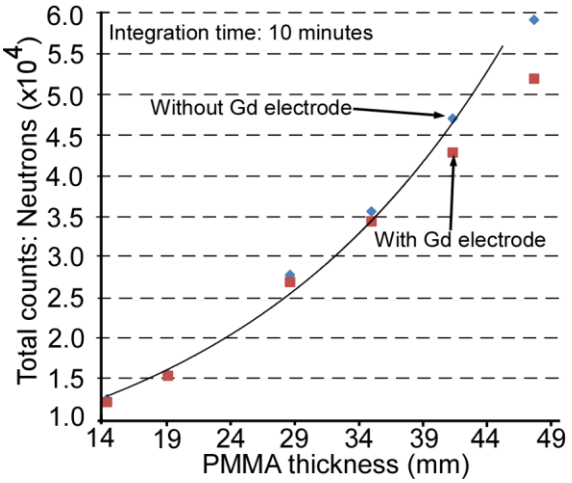

Figure 3-7: (Measured) Experimental characterization of Gd conversion following PMMA moderation. Using ^{252}Cf and a commercial neutron Reuter-Stokes 3-He proportional detector, neutron count increased with thicker PMMA as more neutrons are moderated. By placing 2.1 μm thick Gd between detector and PMMA, the moderated neutrons are converted to fast electrons and gamma rays, leading to neutron count attenuation up to 12.5%.

3.4.5 Receiver Operating Characterstics

The receiver operating characteristic (ROC) curve depicts the compromise between successful detection events and false-alarm events [Kno07]. The probability of true detection, P_D, is determined by the total number of detection events or "counts" in a given period that have exceeded a certain predetermined threshold value in the presence of a radiation source. The probability of false detection, P_{FA}, is determined by the total counts exceeding the threshold value in the absence of source, i.e., in the presence of background radiation. Since radiation is a random event, a Gaussian distribution around a mean count is obtained. The probability distribution function (PDF), *P(x)*, for a Gaussian distribution is given by:

$$P(x) = \frac{1}{\sqrt{2\pi}} \exp\left(- \frac{(x - \bar{x})^2}{2\bar{x}} \right) \quad (3\text{-}6)$$

where x is a data point and $\bar{x}$ is the mean.

Depicted in Fig. 3-8 are two hypothetical Gaussian curves for a radiation detector in presence and absence of a source. In the absence of a source, all counting events occur due to naturally occurring background radiation with a mean count of 1.67 in 10 seconds. In the presence of a radiation source, this mean count increases to 3.67. The best choice of a threshold count level, L_C, will be such that it maximizes probability of true detection event, P_D (i.e., pushes it to 1) while it reduces the probability of false positive events, P_{FA} (i.e., pushes it to 0). For an L_C of about 1.98, the probability that background exceeds this threshold (P_{FA}) is only about 0.03 whereas the probability that counts in the presence of radiation source exceed the threshold (P_D) is 0.76. Therefore, the selected value of L_C could be a good choice to determine the true presence of a source.

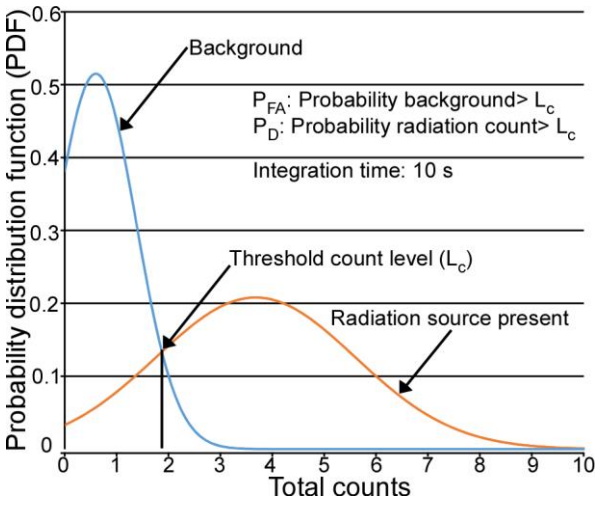

Figure 3-8: Simulated Gaussian distribution of counts in the absence and presence of source.

However, to further increase P_D and decrease P_{FA}, two changes can be made. First is to increase the integration time, i.e., the time over which the count rates are integrated to obtain total counts. This basically improves the confidence level in the total counts obtained, increasing the probability in detecting true radiation source while decreasing the probability of false detection. For a given integration time, P_D can also be increased by increasing detector sensitivity. For a higher detector sensitivity, the counts in presence of source will be higher while counts due to background will only increase slightly. Thus, the overlap between the Gaussian curves of background counts and source radiation counts will reduce, and a threshold count level that is highly improbable for just background but possible in the presence of a source can be set.

3.5 Device Fabrication and Assembly

For convenient technology transfer, the detector elements were manufactured by commercially compatible processes. In particular, the electrodes are formed by photochemical machining of steel foil (Kemac Technology, Inc). In this process, (Fig. 3-9(a)), dry photoresist was laminated on 50 μm thick SS 304. Following double sided lithography, the sample was through-etched by a hot etchant spray. In this particular design, 70-80 μm diameter circular perforations were formed, with 180 μm center-to-center spacing (Fig. 3-9(b)). Additionally, solid SS 304 electrodes were also fabricated to be used as cathodes. A 2.1 μm thick layer of Gd was sputtered on a single side of solid SS 304 cathodes (Fig. 3-10(a)). To facilitate assembly, each element was designed with alignment openings that line up with the package pins. The electrodes are assembled into an 8-pin TO-5 package of 9 mm diameter and 9.6 mm height. It was comprised of a nickel base and a lid composed of a Kovar^{TM} body with a 750 μm thick glass (Corning 7052) window. Electrical feed-throughs are present as insulated pins that perforate the package base. Four of the package pins were replaced by custom tungsten (W) extension pins to enable taller stacks for future generations. Finally, 70 μm thick Kapton^{TM} tape was used as a spacer to assemble the cathode-anode-cathode detector (Fig. 3-10(b)). .

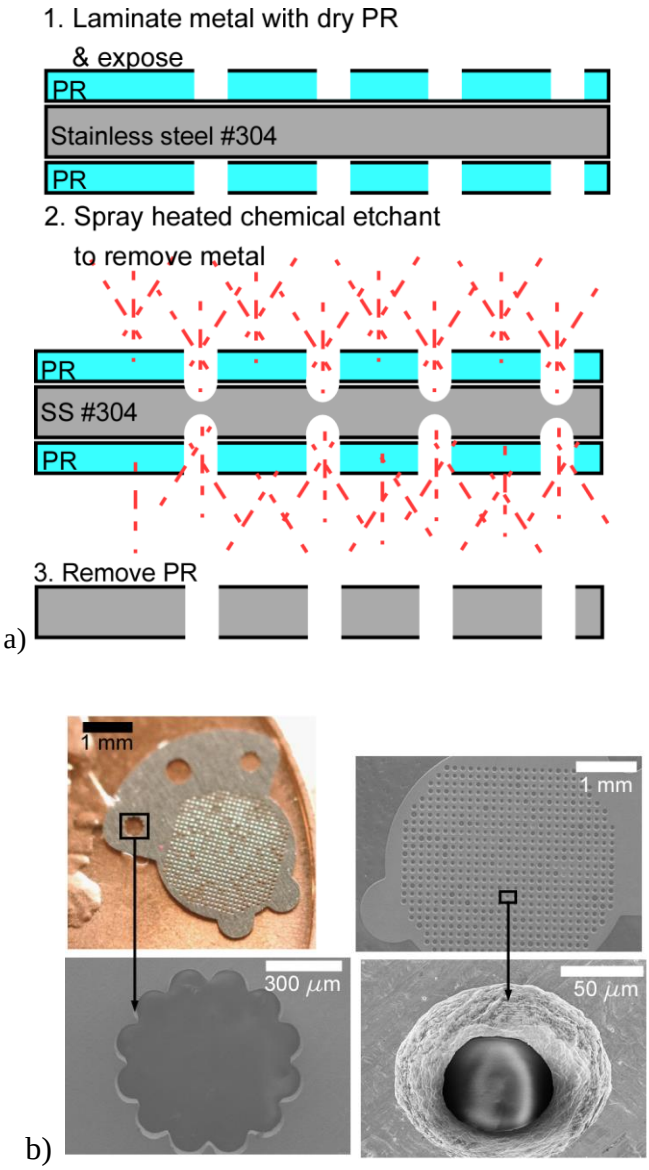

Figure 3-9: a) Fabrication process for photochemically etched electrodes. b) Finished anode with 60 um perforations. SEM shown of the electrode tabs which are used to ensure contact between the Tungsten extension pin and electrode.

a)

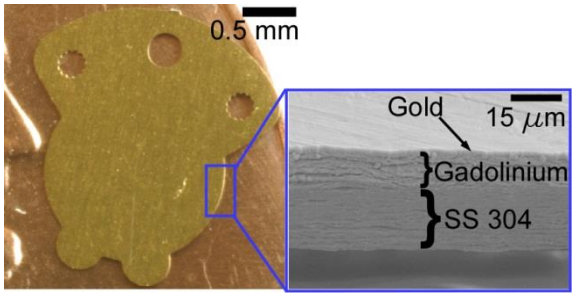

b)

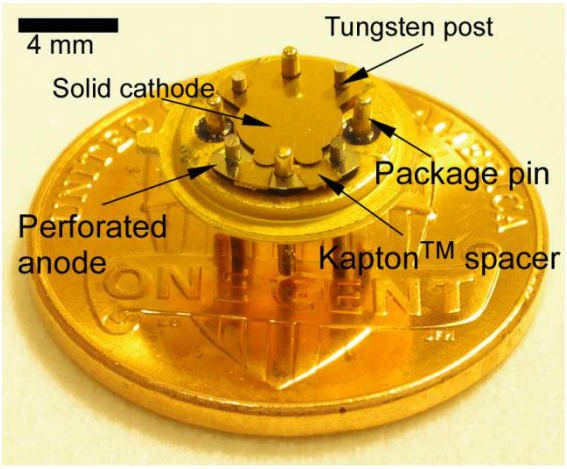

Figure 3-10: Device assembly. (a) Solid cathodes and perforated anode separated by spacer are placed within the TO-5 package. A total of 3 electrodes were used. (b) A solid SS 304 cathode sputtered with 2.1 μm Gd for neutron conversion and passivated with 50 nm gold.

3.6 Experimental Results

The goal of these experiments was to investigate the detector capability and identify performance compromises imposed by the manufacturing approach.

3.6.1 Experimental setup

The detectors were tested in a bell jar which was evacuated and then backfilled with Ar gas near atmospheric pressure. A small flow of Ar was maintained during tests to minimize contamination. Additionally, by using a glass bell jar, all the beta particles were block and only neutrons and gamma rays were admitted to the detector. The detectors were characterized using two sealed sources; one ^{137}Cs (99 μCi), a gamma emitter, and the other, ^{252}Cf (90 μCi), a gamma and neutron emitter. The detector outputs were measured across a 1 nF capacitor using a voltage

probe attached to an oscilloscope (Agilent DS08064A) (Fig. 3-11). A voltage drop across the capacitor signified the creation of ion-electron pairs and was registered as a detection event, or a count.

For every 100 disintegrations of the ^{252}Cf source, 96.91 produce alpha particles which-due to their short range and use of PMMA for neutron moderation-can be safely assumed to not reach the detector. The other 3.09 disintegrations result in spontaneous fission of gamma rays and neutrons. For every spontaneous fission, 8 gamma photons of average energy 0.87 MeV are released and 3.76 neutrons of average energy 0.7 MeV are released. The ^{252}Cf source, which has an activity of 90 μCi, is going through $90 \times 3.7 \times 10^4$ disintegrations/s. Since 3.09% of the disintegrations result in spontaneous fission, the total gamma and neutron activity is 8.23×10^5/s and 3.86×10^5/s respectively. Similarly, for 99 μCi ^{137}Cs which releases gamma rays in 85% of its total radiation activity, gamma photons are released at a rate of 3.11×10^6 /s.

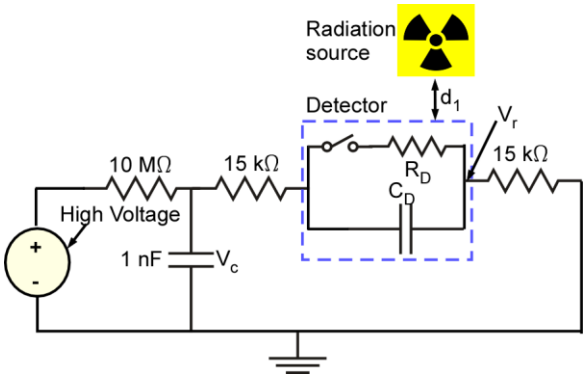

Figure 3-11: The test setup with the device and bias circuitry (positioned at distance, d_1, with Pb shield to remove gamma from the rad source). Two types of measurements were taken in current mode and pulse mode by measuring the current pulse after a detection event, V_r and voltage drop, V_c across the capacitor respectively.

3.6.2 Device measurements

Experiments were performed to determine the neutron detection capabilities of the fabricated device. These tests included determining the neutron detection sensitivity and detector dead time.

The microdischarge current pulses (Fig. 3-12) (measured using the bias circuit shown in Fig. 3-10) were observed to have 400 ns duration and 80 mA peaks. Each pulse is registered as a count. The measured background rates were less than 2 cpm. Background rates are triggered by cosmic rays or naturally occurring background radiation.

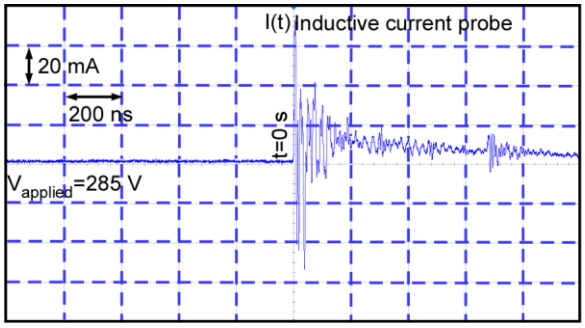

Figure 3-12: (Measured) Current pulse measurement of a "count" showed approximately 800 mA peaks and about 400 ns duration.

3.6.2.1 Neutron detection

The special considerations of using the ^{252}Cf as a test source include not only neutron moderation but also the provision for blocking strong gamma background to ensure pure neutron detection. This was done by introducing a strong gamma absorber, Pb, between the source and the detector. The setup for ensuring sufficient neutron flux to the detector while moderating the neutrons, and blocking gamma from ^{252}Cf, was 48 mm thick PMMA and 6.4 mm thick Pb respectively. The source-to-detector distance was 10.6 cm. To ensure that most of the gamma rays reaching the detector were indeed blocked, the setup was first tested with ^{137}Cs, a pure gamma emitter. The total count with just ^{137}Cs in a period of 10 minutes was not significantly higher than the background (Fig. 3-13). Since the gamma activity of ^{252}Cf is lower than the

gamma activity of ^{137}Cs, the residual counts signify neutron detection. The total neutron count was 8.7 cpm against a background count of 1.2 cpm.

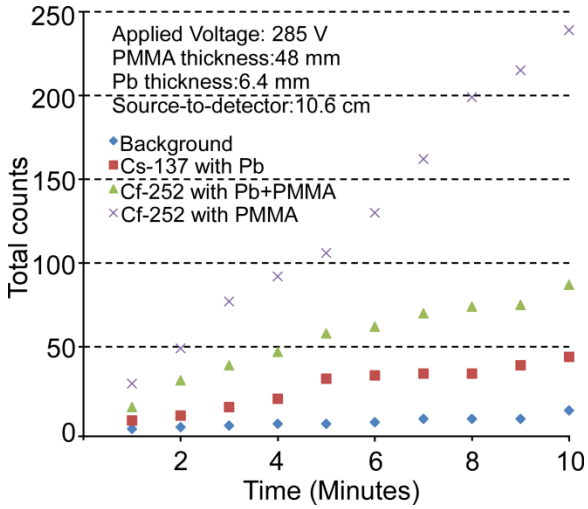

Figure 3-13: (Measured) Neutron detection: Since ^{252}Cf has a gamma background, most number of counts are observed with no gamma shielding (X). Appropriate gamma attenuation shielding by Pb is established using pure gamma source (^{137}Cs) (■). The residual counts obtained after blocking gamma is a result of neutron detection by the detector (▲). (◆) Background radiation.

3.6.2.2 Dead time

A typical G-M detector is unable to detect radiation events for a certain period immediately following a detection event. This period is called the dead time of the detector. When a detection event occurs, the mobility of the positive ions is less than that of free electrons because of the mass of the ions, and they remain essentially motionless as the free electrons are rapidly collected by the anode. The presence of the positive ions in the vicinity of the anode is sufficiently high, their presence begins to reduce the electric field close to the anode below the minimum necessary to maintain an avalanche. The time necessary for the positive ions to migrate to the cathode and thus the electric field to return to its original value is know as the "dead time". For this detector, the dead time was measured as 5.4 ms (Fig. 3-14). This number

also sets the upper threshold on the maximum number of detectable events per second which is just the inverse of dead time, or roughly 200 counts per second.

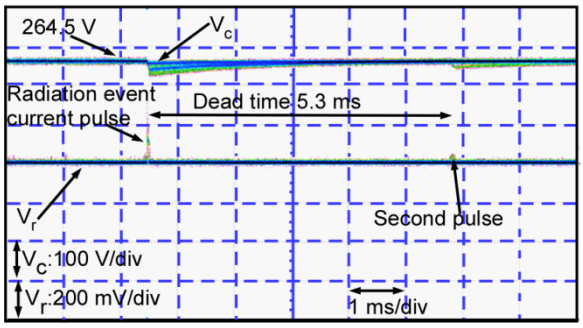

Figure 3-14: Dead time of the device is the duration time the device is inactive as it recovers from a detection event. Dead time sets upper limit on count rate possible with the detector. Refer to Figure 3-10 for V_c and V_r.

3.6.2.3 Detector Receiver Operating Characterstics

ROC curves were calculated (using MATLAB R2013) for the neutron radiation detector. The mean count in the presence of source was 8.7 cpm and the mean count with background radiation was 1.2 cpm. Fig. 3-15 shows the ROC curves for integration times from 30 s to 120 s. The probability of true detection is given by P_D and the probability of false detection is given by P_{FA}. The total counts increase with increasing integration times providing higher confidence of the true detection of a radiation source. This leads to threshold values that are closer to P_D of 1 and P_{FA} of 0 as was observed when the integration time was increased to 120 s.

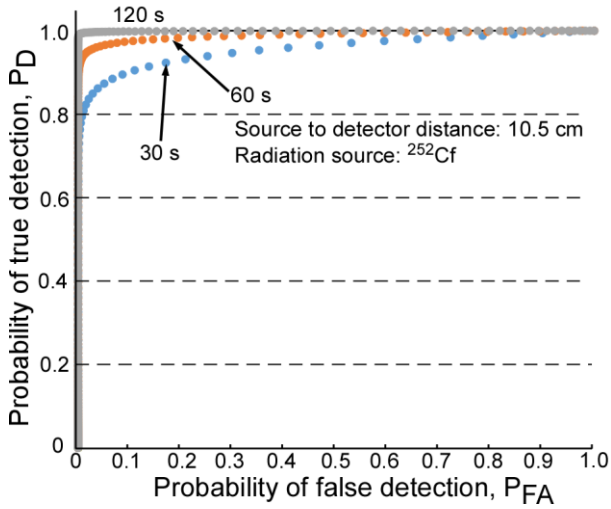

Figure 3-15 ROC curves for various integration times ranging from 30 s to 120 s

Chapter 4: Radiation Detectors with Improved Stability

4.1 Introduction

This chapter introduces a new structure for the micromachined G-M detector in continuing quest for improved stability, increased sensitivity, and reduced system dead time. The revised architecture is introduced in the Section 4.2. Section 4.3 describes the designs of the components which will be used to assemble the device. Based on the designed parts, Section 4.4 discusses how each of the above goals are met with the revised architecture along with the simulation results. Section 4.5 describes the fabrication process and the obtained components. Section 4.6 details the assembly method and finally, Section 4.7 discusses the experimental setup and the obtained results thus far.

4.2 Revised Architecture

Detectors operating in the G-M regime have been used for many years for surveillance efforts to detect high energy radiation like gamma rays. However, conventional G-M detectors are limited by prolonged dead time (≈100 μs), high operating voltages (600-800 V) and limited conversion efficiency (1%-3%) that translates to poor sensitivity. In the past, significant work has focused on addressing these challenges. Devices with thicker walls or walls with higher atomic number have been used to detect high energy gamma rays [Ora14]. However, this decreases the efficiency for low energy gamma rays. Fill gases with higher atomic number like Kr, Xe have been used to improve gamma interaction [Kno07]. However, these gases are relatively expensive, offer poor discharge characteristics, and are limited to detecting lower gamma energy spectrum [Kno07, Cob58]. Some efforts have focused on fabricating multiwire proportional counters using lithography techniques [Oed88, Bac98, Gio96]. Such an architecture

lends itself to position imaging, but it has mainly been limited to detecting low energy X-rays or charged particles.

A new stacked cathode architecture is presented that leverages the 3-D microfabrication to improve device performance and enable detection of high energy gamma rays with increased sensitivity (Fig 4-1). It utilizes a stacked array of cathodes to improve sensitivity by increasing the probability of interaction with incident gamma radiation. The device stability is provided by reducing spurious discharges. This is done by having a thin anode trace patterned and deposited on glass fingers suspended in the middle of larger cathode perforations. In doing so, the avalanche and drift regions for electrons are separated. The electric field lines are more concentrated close to the anode, which provides charge multiplication. The area around the cathode sustains a lower electric field which reduces secondary electron emission from the impinging Ar^+ ions, thereby reducing spurious discharges and making the device stable. Each of the anode finger within a cathode perforation represents an independent detector biased by the common voltage source. This parallel operation reduces the detector dead time. The design parameters for each of parts used to obtain such an architecture are discussed in the next section.

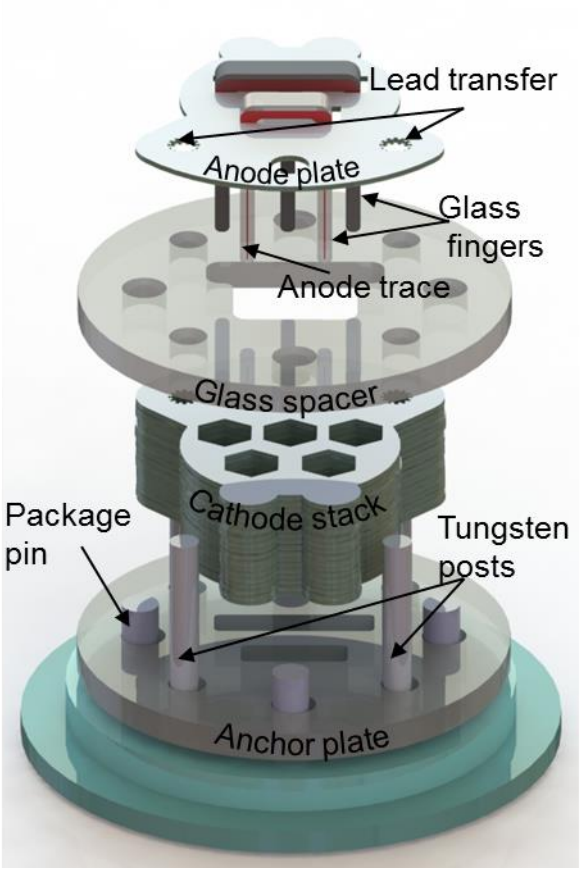

Figure 4-1: Overall device schematic

4.3 Device Design

All the parts to be used in the device assembly are designed around the TO-5 package as its package pins provide spatial alignment as well as electrical contact (Fig. 4.1). The exact dimensions of the package are shown in Appendix A. Since its desirable to obtain a taller cathode stack for increased sensitivity, four of the package pins were replaced with taller tungsten posts having a diameter of 500 μm. These tungsten posts can then be used to create a 3-D stack.

4.3.1 Stainless Steel Cathode

The cathode is designed to have hexagonal perforations to provide uniform probability of a photoelectron emerging from the cathode walls (Fig. 4-2). The edge length of each hexagonal

perforation is limited mainly by two factors. It needs to provide clearance for glass fingers to pass through. Additionally, there should be sufficient distance between the perforation vertex and anode trace to provide separation of the avalanche and drift region. The hexagonal perforations are strategically placed to make sure that any photoelectron created in the active area, with energy greater than 100 keV could escape through the metal and emerge in the gas and ionize it. Each cathode also has circular perforations to provide spatial alignment and also enable lead transfer through the package pins. Two of these perforations have tabs to make electrical contact with the tungsten posts. For the purposes of fabrication process compatibility and appreciable interaction with gamma rays, each cathode layer is to be fabricated using 50 μm thick SS 304 sheet.

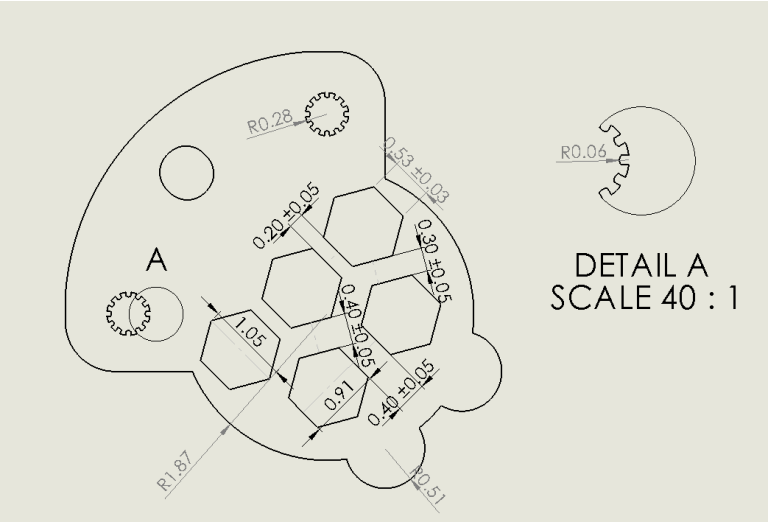

Figure 4-2: Cathode schematic. All dimensions are in mm

4.3.2 Glass Finger

The glass fingers are designed to provide the support structure for depositing thin anode trace, the site of avalanche multiplication. For ease of handling and mechanical robustness, the material of choice is Pyrex 7740 glass of 500 μm thickness. Additionally, to provide structural support to fingers so that these do not break away, each of the glass fingers is greater than 250

μm wide. The spacing between the fingers is designed with respect to the placement of hexagonal perforations on the cathode. Two and three finger designs are shown in Fig. 4-3a) and 4-3b) respectively.

a)

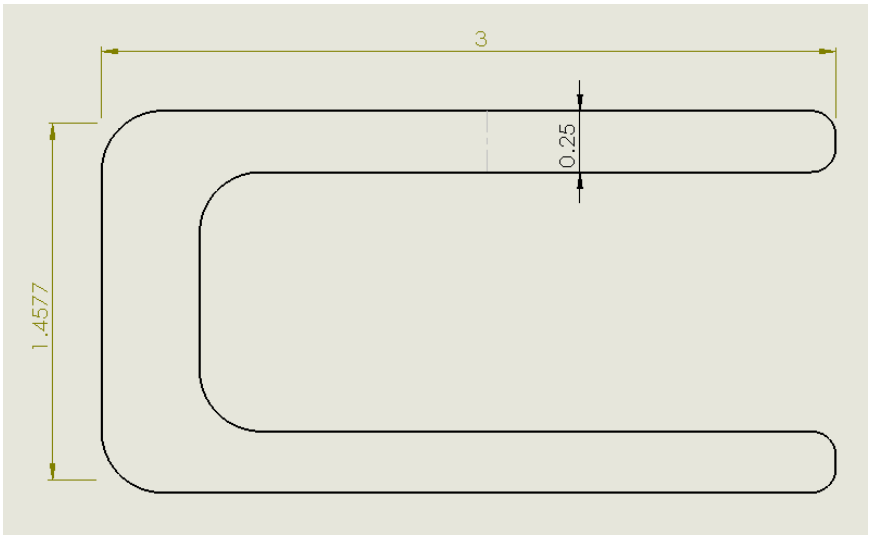

b)

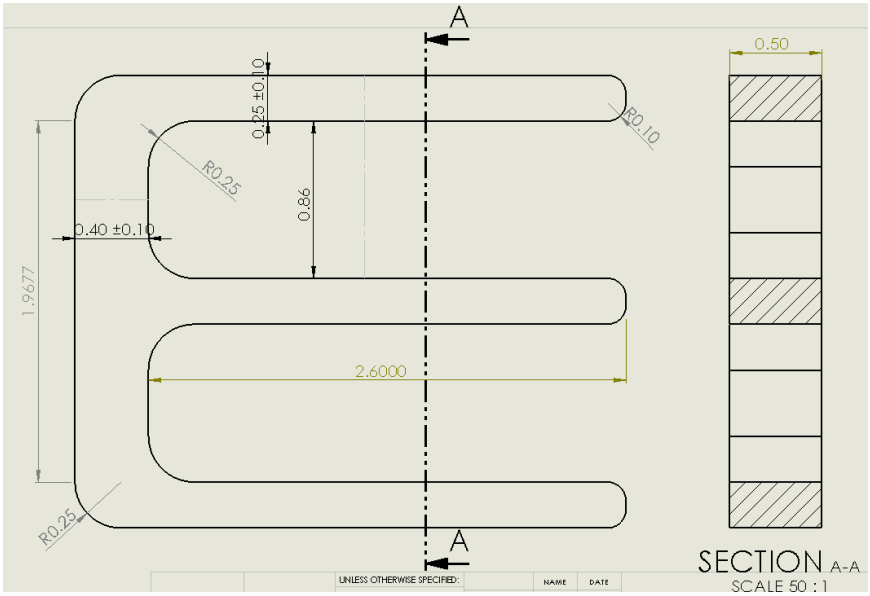

Figure 4-3: Glass finger designs: a) Two finger and b) Three finger. All dimensions are in mm

4.3.3 Stainless Steel Anode Plate

The anode plate is designed to limit the movement of the glass fingers and provide lead transfer. Anode plates have rectangular perforations through which the glass fingers passed and

helped maintain a constant distance of 215 μm between the anode trace and the cathode perforation vertex. The dimensions for the circular perforations are identical to the cathode and provided the same functionality of lead transfer and spatial alignment. These are designed for 50 μm thick SS 304. Figure 4-4 shows the anode plate design along with listed dimensions of the rectangular perforations. The dimensions for the circular perforations are not listed as these are the same as cathodes.

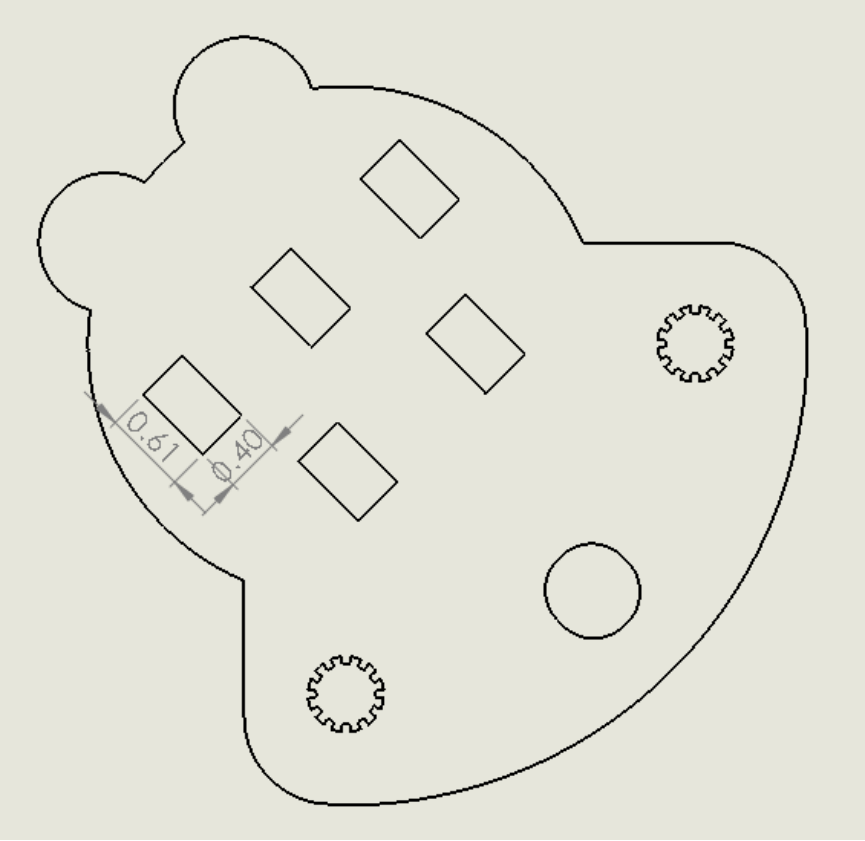

Figure 4-4: Anode plate design. All dimensions are in mm

4.3.4 Glass Spacer and Glass Anchor Plate

The glass anchor plate is designed to limit the movement of glass fingers and insulate the package base from both anode and cathode. A glass spacer is designed to separate the anode base plate from the cathode stack. It has a large opening to let the glass fingers pass through.

The circular perforations in both glass spacer and glass anchor plate provide alignment with respect to the package pins. Once again, for easier handling and mechanical robustness these are designed for 500 μm thick Pyrex 7740 glass. Figure 4-5 a) and b) shows the design glass anchor plate and glass spacer respectively along with dimensions in mm.

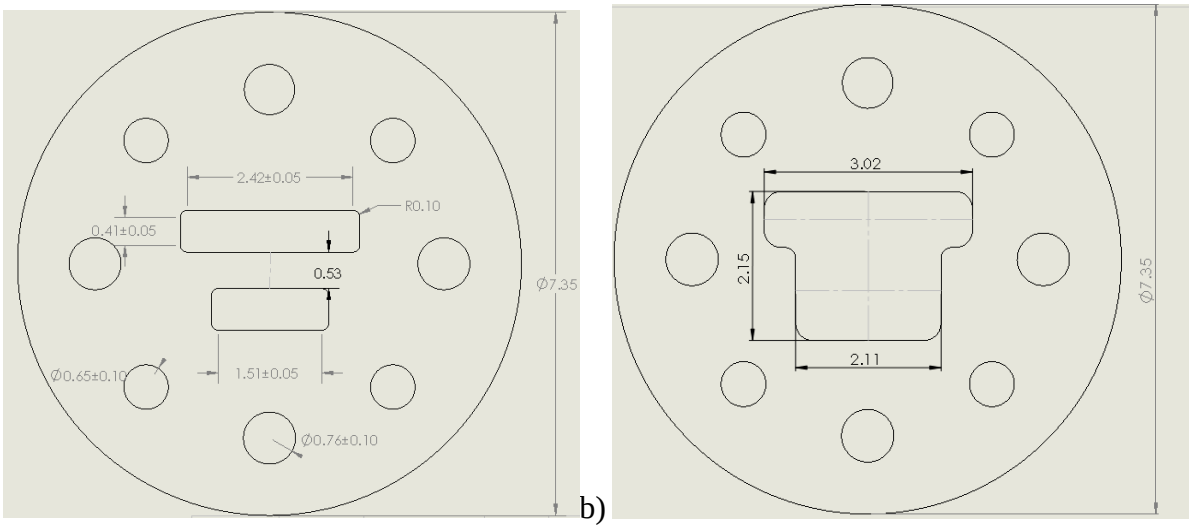

Figure 4-5: Designs for a) glass anchor plate and b) glass spacer. All dimensions are in mm.

4.3.5 Anode Trace

Finally, a thin anode trace patterned on the glass fingers is required to concentrate the electric field lines and create a discharge at low voltages. It is designed to be 3 μm wide, limited by the lithographic patterning process. Additionally, wider metal is placed at the base of the glass fingers to make contact with the anode plate using conductive epoxy (Fig.4-6). Figure 4-7 shows the final schematic of anode trace on glass fingers.

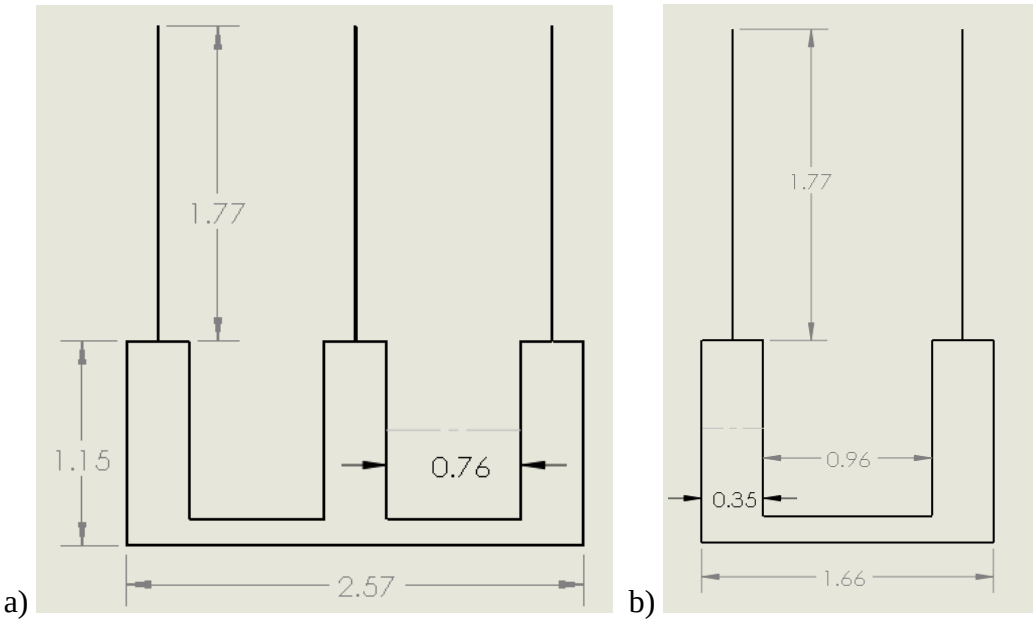

Figure 4-6: Anode trace design for a) three fingers and b) two fingers. All dimensions are in mm

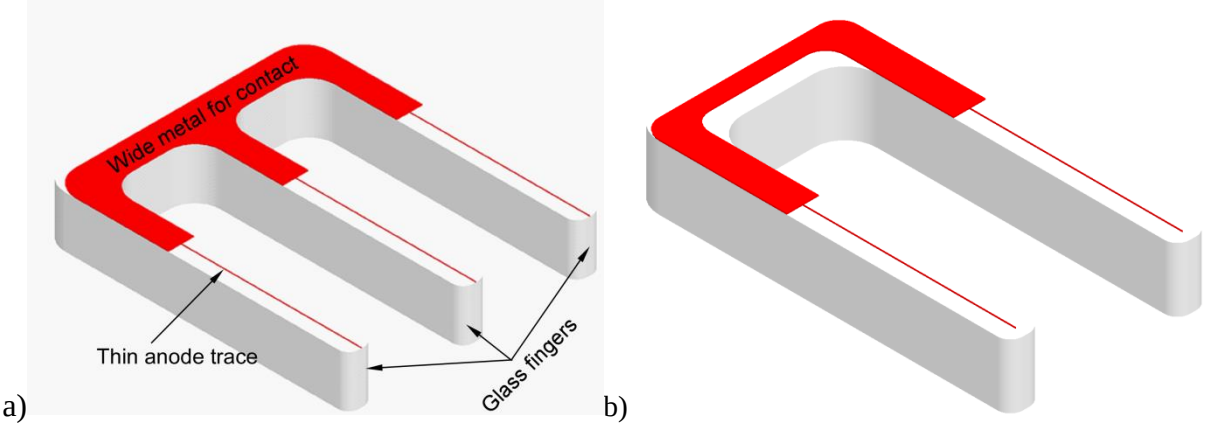

Figure 4-7: Schematic for anode trace on glass fingers a) three fingers and b) two fingers

4.4 Device Modeling

This section provides the theoretical foundations of the device stability and sensitivity along with simulations which show how each of the primary goals of improved stability, increased sensitivity and reduced dead time can be met with the proposed design.

4.4.1 Avalanche and Drift Region Separation

In conventional G-M detectors, a thin wire is used as an anode, while a hollow cylinder is used as a cathode. Fig. 4-8a shows the setup with typical anode and cathode dimensions. In operation,

after the primary Geiger discharge is terminated, the positive ions slowly drift away from the anode wire and ultimately arrive at the cathode or the outer wall of the counter. Here the ions upon combining with an electron from the cathode surface. In this process, an amount of energy equal to the ionization energy of the gas minus the energy required to extract the electron from the cathode surface is liberated. If this liberated energy also exceeds the cathode work function, it is energetically possible for another electron to emerge from the cathode surface. This electron will then drift towards the anode and will trigger another avalanche, leading to a second full Geiger spurious discharge.

In the conventional architecture, the electric field variation from anode to cathode is exponential in nature [Kno07]. The advantage of such architecture is that electric field crosses the Townsend avalanche threshold only in vicinity of the anode (Fig. 4-8b). The areas close to the anode having high electric fields, are responsible for electron multiplication and are called avalanche regions. Located away from the vicinity of anode and towards the cathode are the drift regions with lower electric fields. Once the avalanche has terminated, and as Ar^+ ions drifting towards the cathode undergo charge exchange or momentum transfer collisions losing their energy [Phe91]. Thus, Ar^+ ions have a lower probability of releasing secondary electrons because of frequent collisions and ever decreasing electric field as the ions approach the cathode thus limiting the maximum amount of kinetic energy the ions can gain. The secondary electron emission probability is further decreased by using a quench gas (usually halogen gases) which has a lower ionization potential and more complex molecular geometry than Ar. The positive ions formed are mostly of primary type i.e. Ar^+ ions, and as these drift towards the cathode they undergo charge exchange collisions with quench gas, in effect transferring their charge to quench gas molecules and becoming neutral. By having a 5-10% concentration of the quench gas, most

of the ions reaching the cathode are of quench gas type and the excess energy released is used is disassociating complex gas molecules than releasing secondary electrons.

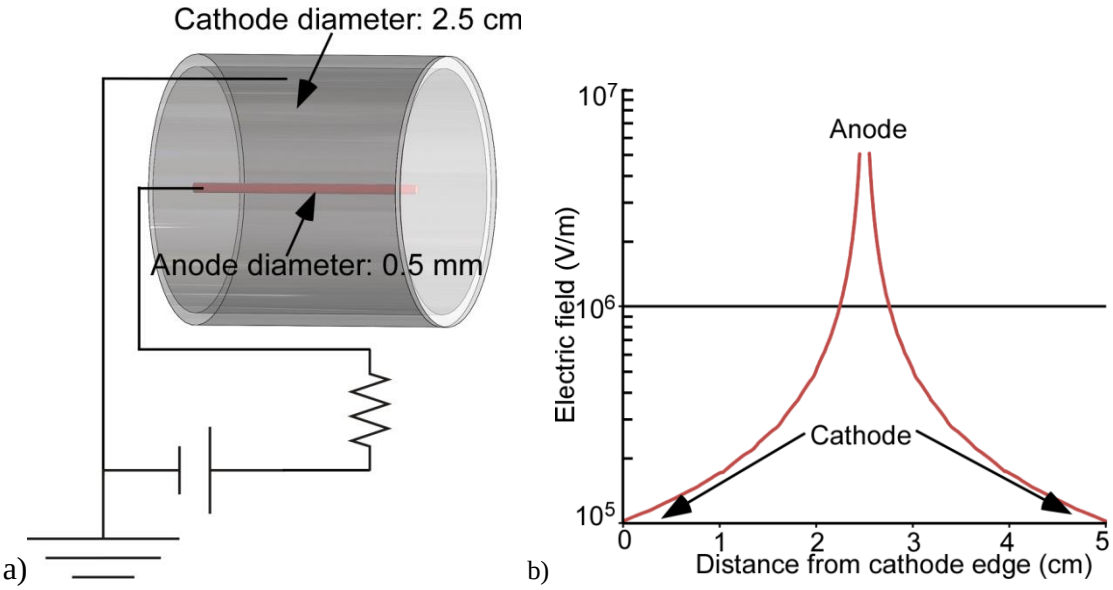

Figure 4-8: A conventional G-M counter with accompanying electric field variation.

However, in structures that have been described in chapter 3 as well as the ones fabricated previously [Eun10],[Eun11], the perforated anode and a planar cathode do not provide an exponential reduction of electric field moving from anode to cathode. As shown in Fig. 3-4 the electric field ratio of anode:cathode is only 2:1. A large number of ion-electron pairs are created during a discharge, approximately 10^{12}, and even if one of these ions has enough energy to release a secondary electron, a spurious discharge takes place. Even though it will be difficult to eliminate all spurious discharges, careful design considerations can definitely reduce a large proportion. This can be done by creating an architecture that separates drift and avalanche region, i.e., it increases the ratio of the electric field between anode to cathode.

4.4.1.1 Electric Field Simulations

By having a very thin anode trace on the glass fingers and a comparatively large cathode perimeter, as determined by the perforation in stacked cathode plates, an exponentially distribute asymmetric electric field can be obtained.

Electric field simulations of the anode-cathode system are obtained using COMSOL 3.5a (Fig.4-9a). For the purpose of these simulations, the distance between anode trace to cathode perimeter is 215 µm. Anode trace width is 3 µm wide, it is patterned on a Pyrex 7740 glass substrate that is 250 µm wide, 500 µm thick and has a dielectric constant of 4.6. Applied voltage is 100 V. As can be observed from Fig. 4-9 a) an electric field distribution of 50:1 is achieved when moving from edge of the cathode perimeter towards the anode trace. The region in the vicinity of the anode trace sustains an electric field a maximum electric field of 5×10^6 V/m, enough to create an avalanche discharge [Kno07]. Such an electric field distribution ensures avalanche discharges take place close to anode; the majority of the Ar^+ ions, as they traverse through the interelectrode gap, do not gain enough energy to release secondary electrons from the cathode. Another concern in this architecture can be the charging of glass substrate due to accumulation of Ar^+ ions. However, as shown in Fig. 4-9 b), the electric field on the edge of the glass is about 5000 V/m. This electric field provides a sufficient repulsive force to the Ar^+ ions to ensure that no charge accumulation occurs even in areas furthest from the anode trace (i.e., closest to the glass edge), where the resulting repulsive force will have its lowest value.

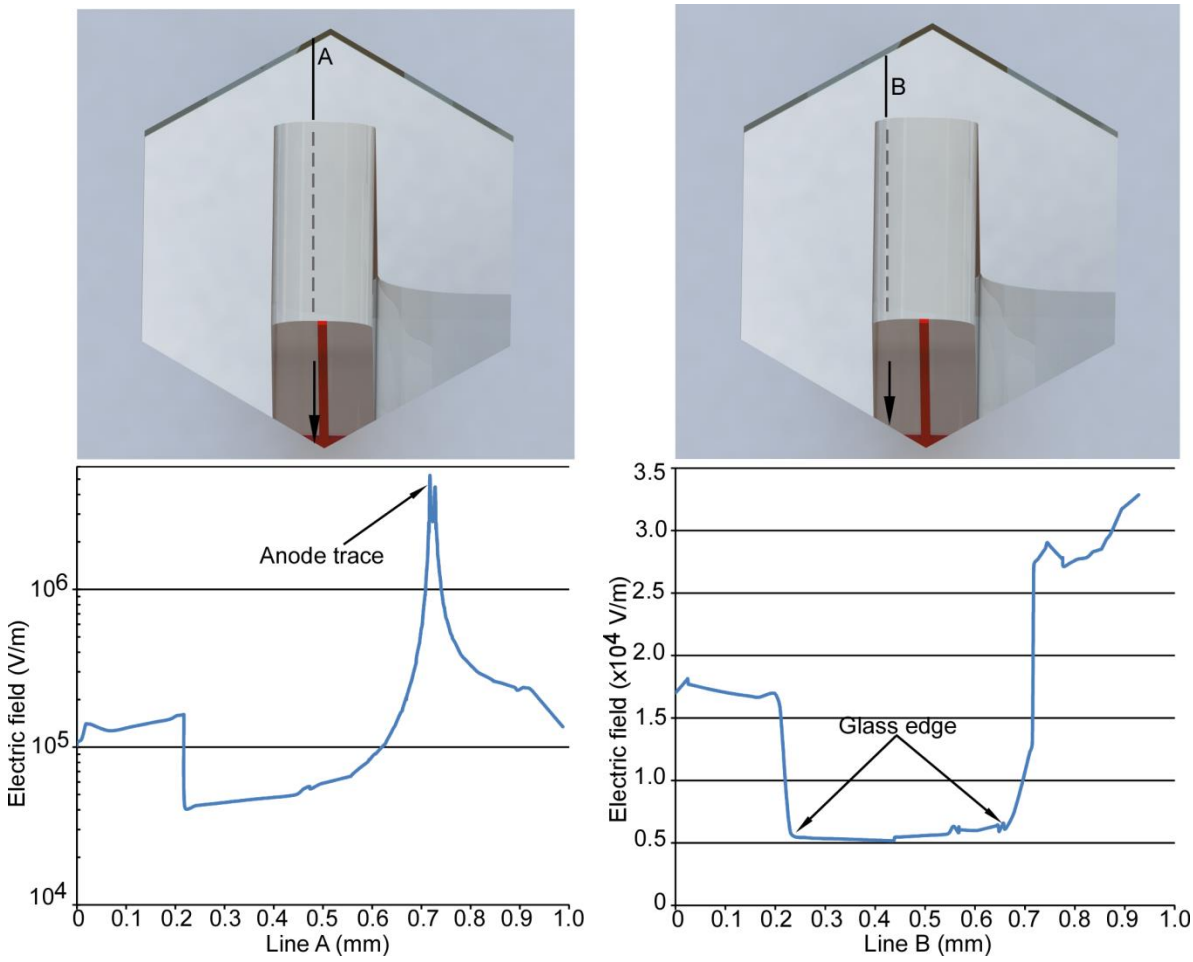

Figure 4-9: Electric field simulation for areas a) close to anode trace and b) close to glass edge

4.4.2 Reduced Dead Time

Each set of the stacked hexagonal cathode perforations and the enclosed anode finger form a G-M detector. Each of the detectors is powered by the same voltage source, and are connected in parallel. The parallel operation the detectors is advantageous in improving system dead time. If one of the detectors has undergone a detection event, while it is making a recovery; the other detectors are still active, capable of detecting radiation. This results in effective reduction of the dead time of the overall system. In contrast, conventional G-M detectors have a limited dead time in the range of ≈100 μs [Kno07]. By having 5 G-M elements in parallel, the dead time can potentially be reduced linearly to ≈20 μs.

Maximum counting rates are determined by the detector dead time. By having a smaller dead time, it is possible to count more radiation events. This is advantageous for the entire field of gas-based detectors operating in G-M regime, since the upper limit on maximum counting has so far prohibited their use in high radiation environments.

4.4.3 Increased Gamma Sensitivity

Increasing the stack height enhances the probability of interaction with incident gamma rays, leading to more photoelectrons, and thus more counts for every unit of radiation. The probability of gamma interaction can be found using the mean free path (λ), which is the reciprocal of gamma attenuation factor. The gamma attenuation factor is directly proportional to atomic number of interacting material, Z, and inversely proportional to gamma ray energy, E. Although analytical formulas exist to determine gamma attenuation factor, it is best found empirically. A table for compiled gamma attenuation factors for all elements and different gamma energies can is available [Ato13].

Knowing the mean free path for different gamma energies in SS 304, it is possible to determine the percentage interaction as the cathode stack height increases. Fig. 4-10 shows the percentage gamma interaction of the detector as a function of gamma energy with for progressing stack height. These results are obtained using Monte Carlo simulations performed in MATLAB. In these simulations, it is assumed that gamma rays interacted with unperforated SS 304 stacks, ignoring hexagonal perforations of the cathodes. Such an assumption leads to overstating the gamma percent interaction because a perforation presents a region where the gamma ray passes through without interaction.

The trajectory of a gamma ray, x, was tracked in one dimesion, through the SS 304 by integrating its equation of motion given by

$$x = \int v.dt \tag{4-1}$$

where v is 3.8×10^8 m/s, velocity of a gamma photon and dt is the time elapsed as it travels through the metal. The point of next gamma photon collision is given by d= $\lambda \pm \Delta\lambda$ where $\Delta\lambda$ is the variation from the mean free path. For a Gaussian distribution of the collision mean free path, the distance to next collision was d=-λ ln(r), where r was a random number between 0 and 1 [Cha80]. Each collision was recorded as a gamma interaction. If no collision occurs, then the integration in eqn 4-1 is continued until the gamma ray escapes through the metal. Repeating this process for 5,000 gamma rays provided the probability of gamma ray-metal interaction as a function of gamma energy and increasing stack height. Each cathode was 100 μm thick. A cathode stack, 500 μm thick contained 5 cathodes. The mean free path (λ) value corresponding to each gamma ray energy is presented in Table 4-1.

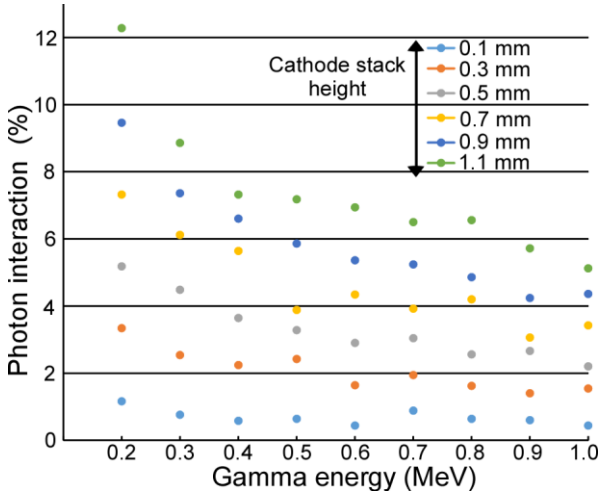

Figure 4-10: Simulated photon interaction as a function of incident gamma energy with increasing stack height.

Table 4-1: Mean free path for different gamma energies [Ato13].

Gamma energy (MeV)	0.2	0.3	0.4	0.5	0.6	0.7	0.8	0.9	1
Mean free path, λ (mm)	9.29	11.86	13.68	15.15	16.47	17.46	18.31	19.73	20.82

Another way to present the interaction probability is based on the expected photon interaction as a function of stack height and gamma energies (Fig. 4-11). The gamma photon interaction (γ_i) was plotted using the following equation [Kno07]:

$$\gamma_i = 1 - e^{-\mu x} \tag{4-2}$$

where μ is the gamma attenuation factor, unique for each gamma energy, and x is the metal thickness. This result agreed with that of Fig. 4-10 because the photon interaction has the same dependence on the mean free path of the gamma rays. As stated previously, mean free path is just the reciprocal of gamma attenuation factor.

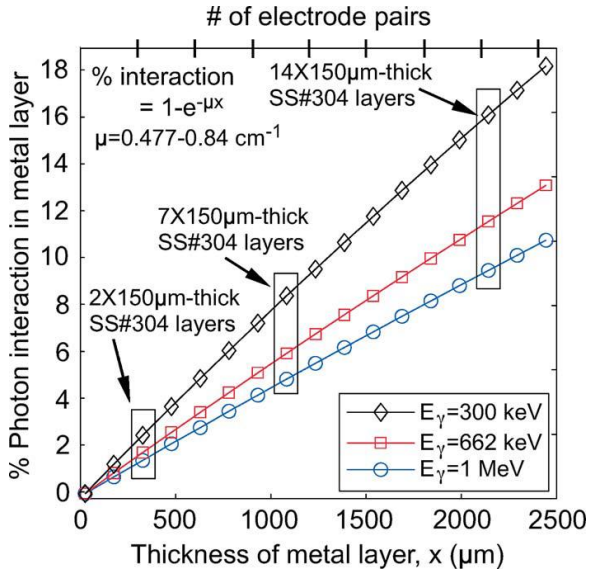

Figure 4-11: Photon interaction in SS 304 as a function of its stack height, for different gamma energies.

4.4.4 Receiver Operating Characteristics

ROC curves for increasing integration time and increasing cathode stack height are shown in Figs. 4-12 and 4-13, respectively. The simulations are carried out using MATLAB. A 99 μCi ^{137}Cs source is assumed to be located at a distance of 30.5 cm, resulting in a flux of 33 gamma rays/s at the detector having a radius of 2 mm. The gamma rays are assumed to have a characteristic energy of 0.662 MeV. The mean count rate in the presence of source is then obtained by percent interaction of 0.662 MeV gamma rays using Fig. 4-11. The mean counts under an integration time of 10 s, for increasing stack height are listed in Table 4-2. It is assumed that each gamma ray interaction with metal results in a detection event. This is a justifiable assumption considering each cathode has a limited thickness that allows the photoelectrons with characteristic energy of 0.662 MeV, having range of 500 μm, to escape to the metal surface [Kno07]. For the background mean count, the number is experimentally obtained from a stack of 7 electrodes, each 150 μm thick [Eun11]. While it is true that background counts will vary with the stack height, by using the background with the highest stack size, the highest possible background count is used for simulations. In doing so, the simulations underestimate the true ROC curves because P_{FA} should be lower than the values obtained by the using the highest possible background count.

Each data point represented the P_D and P_{FA} of a certain threshold level. For a very low threshold level, both the background count and radiation source count exceed the threshold count, leading to both P_D and P_{FA} to be 1. As the threshold level is increased, P_{FA} moves to zero while P_D remains 1. If the threshold level is increased beyond a certain point, as expected, P_D also moves toward zero.

For a cathode stack height of 100 μm and 300 μm and an integration time of 10 s, no threshold level guarantees ideal P_D and P_{FA} values because of higher overlap between background and mean counts. Thus the integration time over which detection events must be increased to reduce the overlap between background counts and radiation source counts (Fig 4-12). Alternatively, the performance can be improved by increasing stack height which makes the device more sensitive. As shown in Fig. 4-13, for stack heights exceeding 500 μm, threshold levels can be obtained that drive P_D to 1 and P_{FA} to 0.

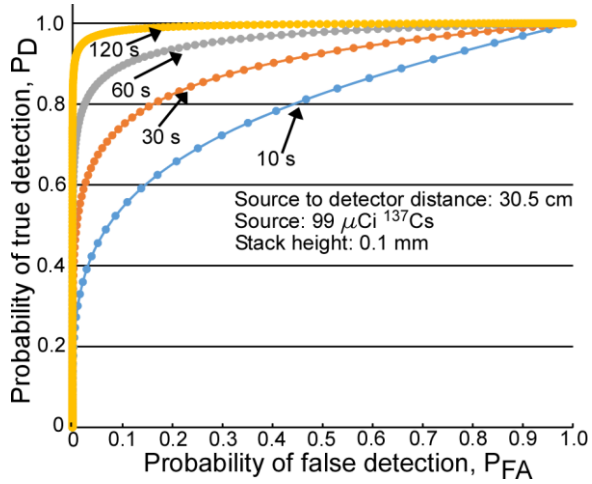

Figure 4-12 Simulated ROC curves for various integration times and a stack height of 0.1 mm.

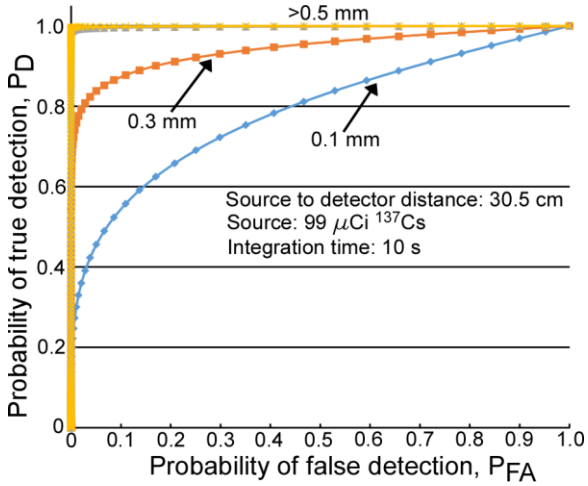

Figure 4-13: Simulated ROC curves for various stack heights and an integration time of 10 s.

Table 4-2: Simulated mean counts for various stack heights for an integration time of 10 s.

Stack height (mm)	0.1 mm	0.3 mm	0.5 mm	0.7 mm	0.9 mm	1.1 mm
Mean counts	1.67	3.67	9.70	12.03	15.04	20.72
Background	0.6					

4.5 Device fabrication

The device fabrication leverages commercially available micromachining techniques and services to fabricate all the parts required for assembly. The metal fabrication was performed using the commercially available photochemical machining (PCM) process (Kemac Inc.). The glass fabrication was performed using the commercially available abrasive jet machining (ABJ) process (Bullen Ultrasonics). Each of the steps along with the fabricated parts form the discussion of the subsequent sections.

4.5.1 Photochemical Machining for SS 304

The photochemical machining method was used to fabricate the anode plate and cathode on 50 μm thick SS 304. The exact process had already been illustrated in Figure 3.8a). In the process, dry photoresist is applied on both sides of 50 μm thick SS 304. Following double-sided lithography, the sample is etched using an etch spray. The tolerances of the process are +/- 25 μm on each side. Figure 4-14 shows the post fabrication results of PCM process for anode plate and cathode.

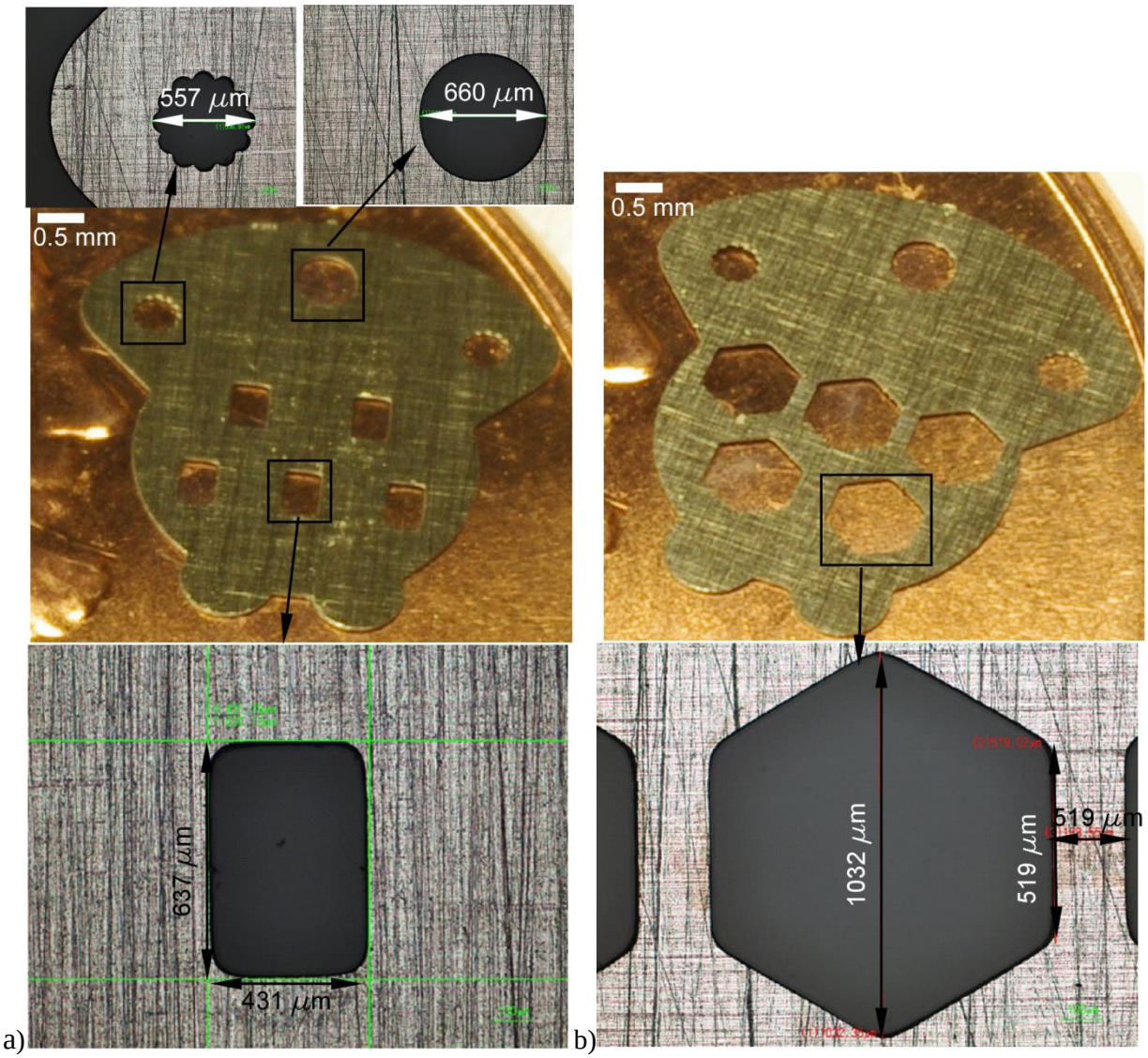

a) b)

Figure 4-14: Post fabrication images of a) Anode plate and b) Cathode

4.5.2 Anode Trace Patterning

Metal layers of Ti/Pt (25 nm/100 nm) were deposited and patterned to form thin anode trace on 500 μm thick Pyrex 7740. The deposition performed by the evaporation process and the pattern was performed by liftoff. Fig 4-15 shows the anode trace deposited on glass. An illustration of a fully patterned metal on a 4 inch Pyrex 7740 glass wafer is shown in Fig.4-16.

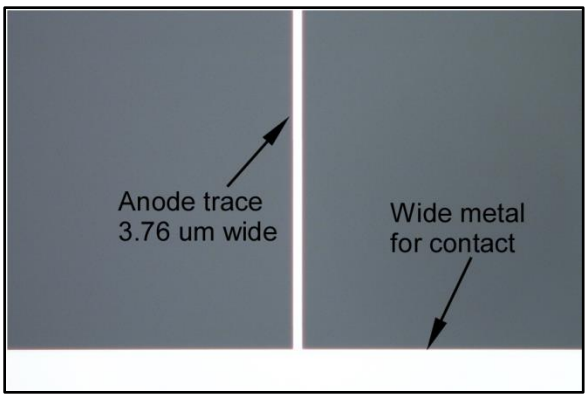

Figure 4-15: Patterened metal on glass wafer

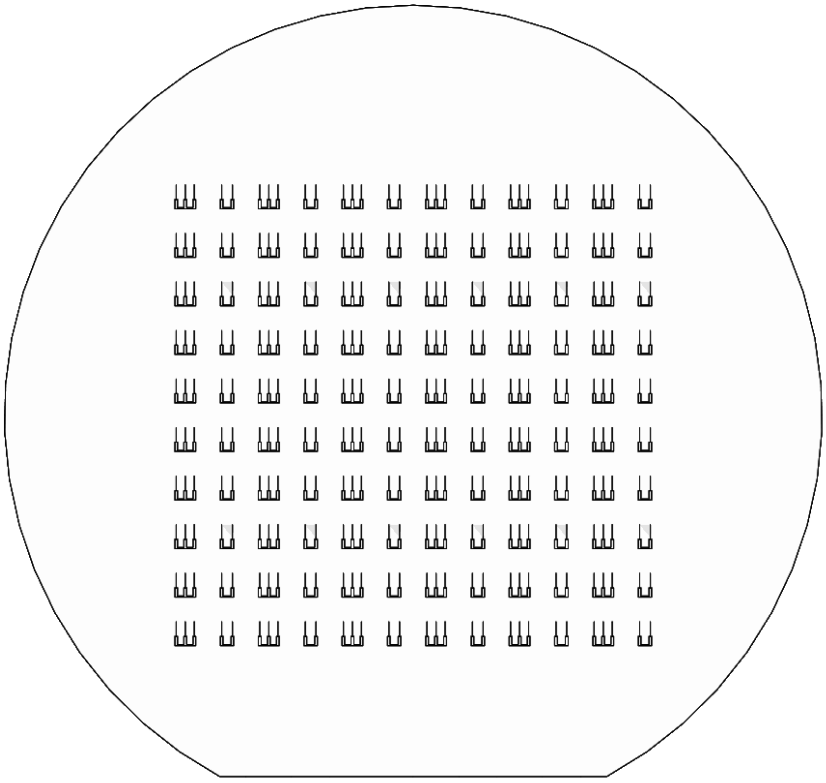

Figure 4-16: Patterned metal on a 4 in diameter Pyrex 7740 glass wafer

4.5.3 Abrasive Jet Machining for Glass

The glass wafers with metal patterns were sent for abrasive jet machining to release the two and three finger designs (Fig. 4-17). Double sided machining was used to reduce the taper associated with the machining. Fig. 4-18 show post fabrication image of the finger structure.

One of the sides had been overetched due to misalignment (Fig. 4-18 b). Fig. 4-19 shows the post fabricated glass base plate and glass spacer

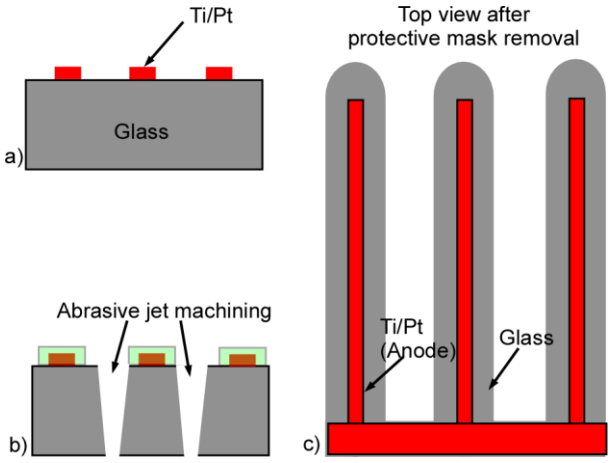

Figure 4-17: Fabrication procedure for glass fingers with patterned metal. (a) Deposit and pattern a Ti/Pt layer on a glass substrate. (b) Use abrasive jet machining to create the finger structure (c) Top view of the finger structure after machining

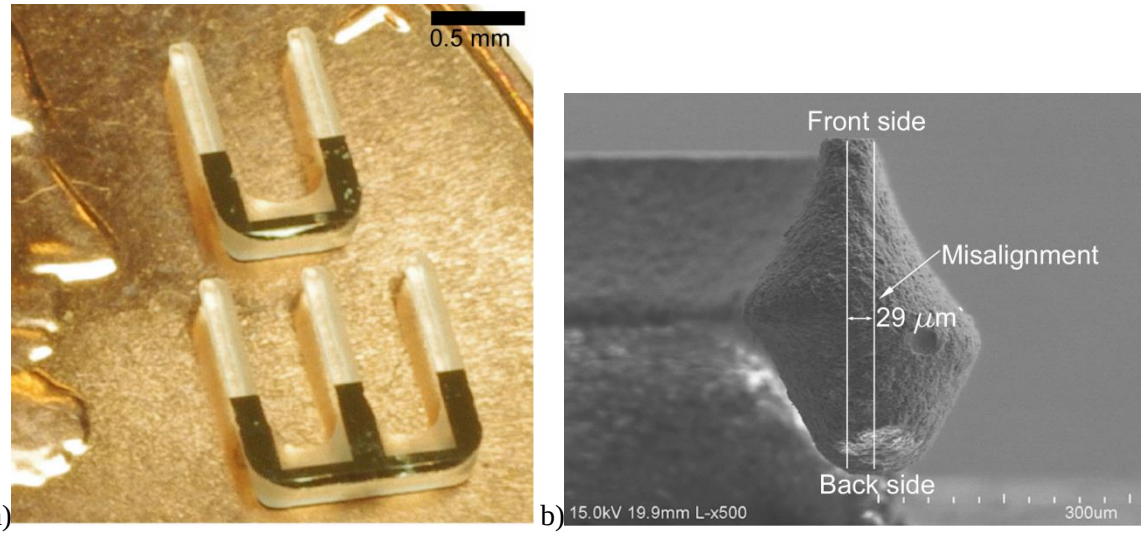

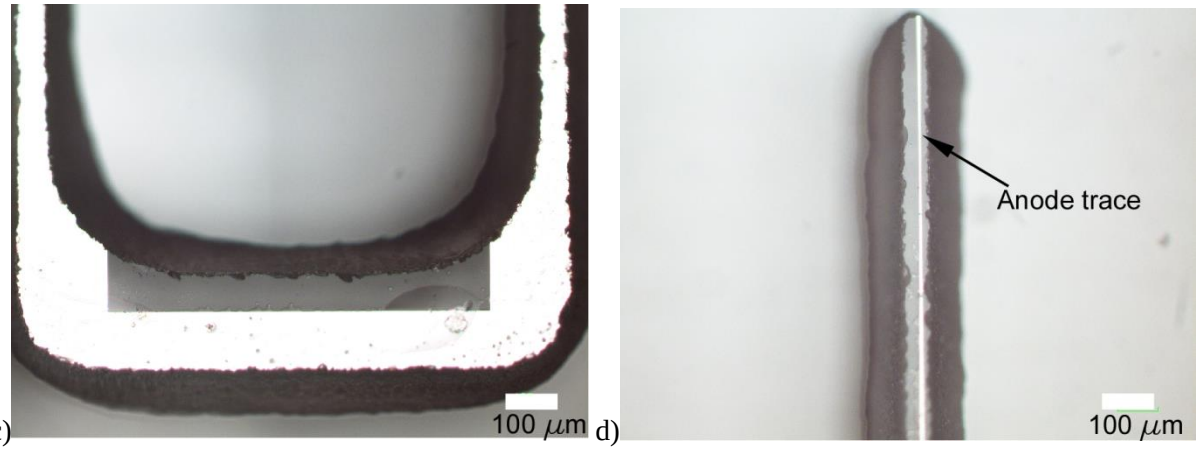

Figure 4-18: Glass finger after release using the abrasive jet processing a) Overall finger structure b) side view showing the misalignment c) closeup of the metal pattern and d) the anode trace

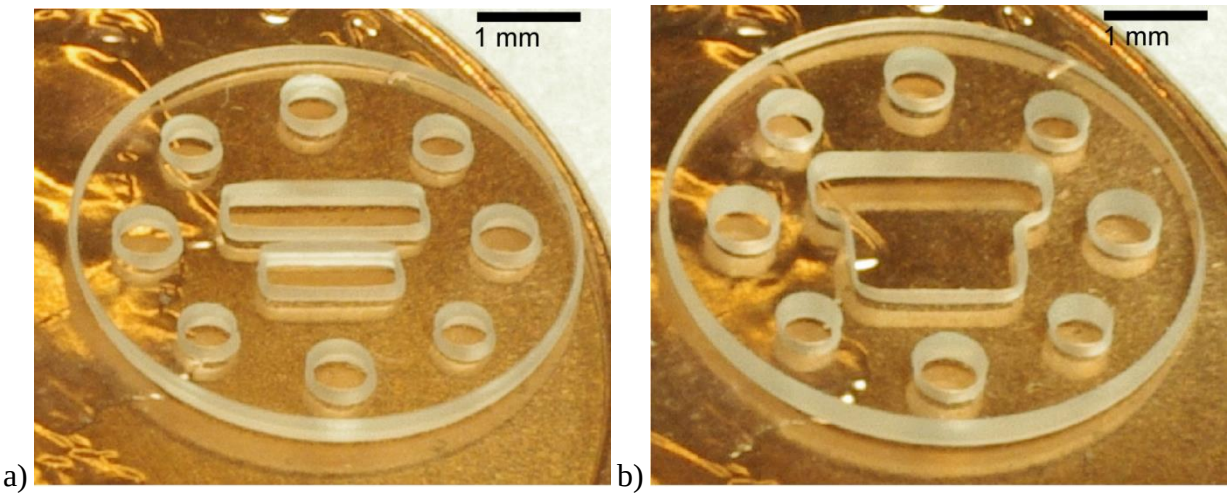

Figure 4-19: Post fabrication for a) Glass base plate and b) Glass spacer

4.6 Device Assembly

The device was assembled on TO-5 header packages. Package pins were used for alignment as well as making electrical contact. The glass anchor plate was placed first to insulate the base and additionally limit the movement of glass fingers. The SS 304 cathode stack was placed next. The circular perforations made contact with the tungsten pins and also provided spatial alignment. The glass spacer was placed next. The SS 304 anode plate was placed next, this provided the lead transfer for the anode trace to the package pins. Finally, the fingers with anode trace were placed last. Due to tighter machining constraints on the photochemically machined

SS 304 metal, anode plate also reduced the tilt angle of the fingers when placed vertically. By constraining the movement of glass fingers using the anode plate, a fixed distance of 215 μm was obtained between the narrow anode trace and the cathode perforation edge. Fig. 4-20 illustrates the fabrication sequence described above. Fig. 4-21 shows the final assembled device.

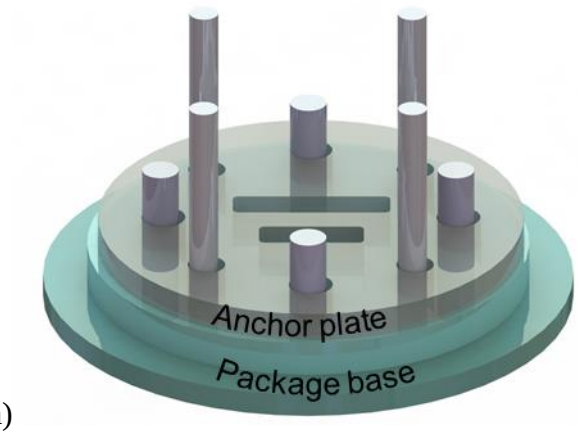

a)

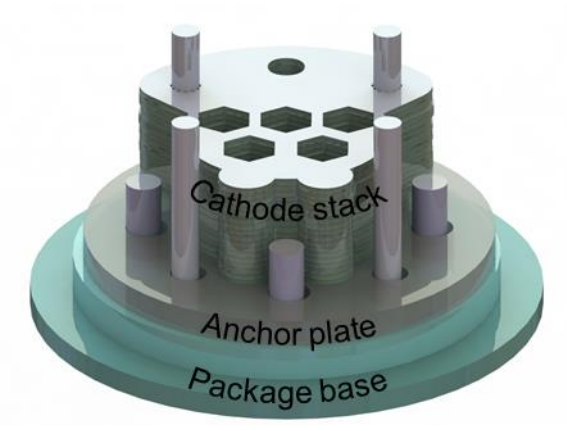

b)

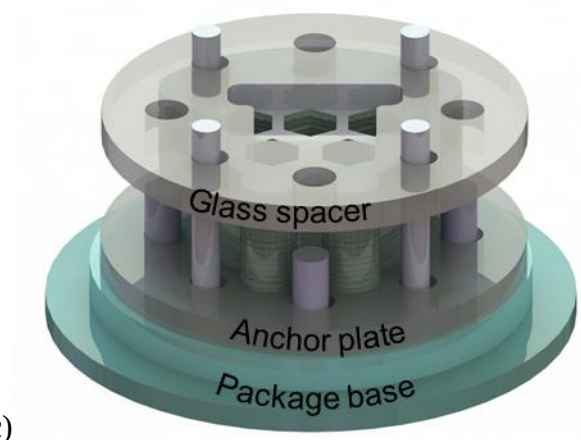

c)

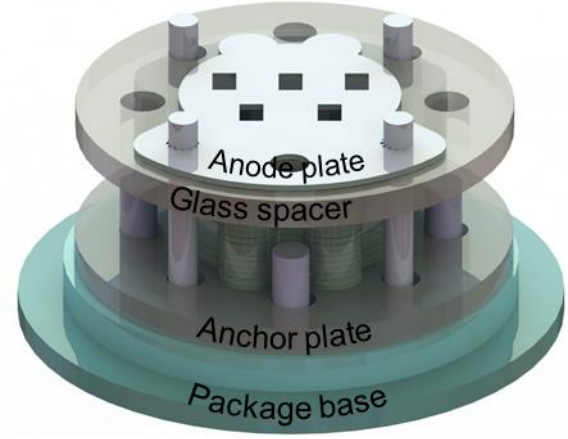

d)

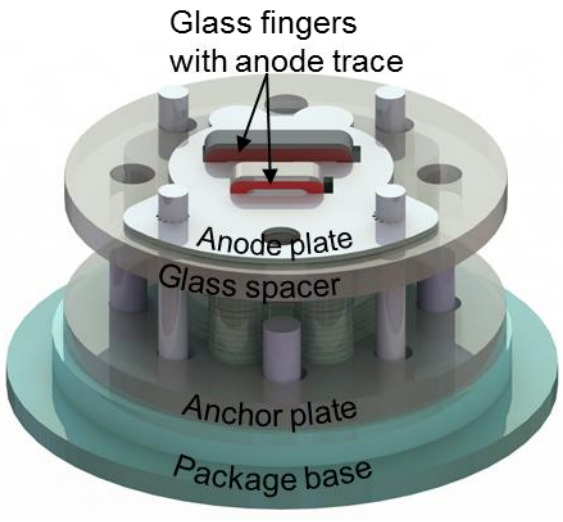

e)

Figure 4-20: Assembly sequence for the radiation detector

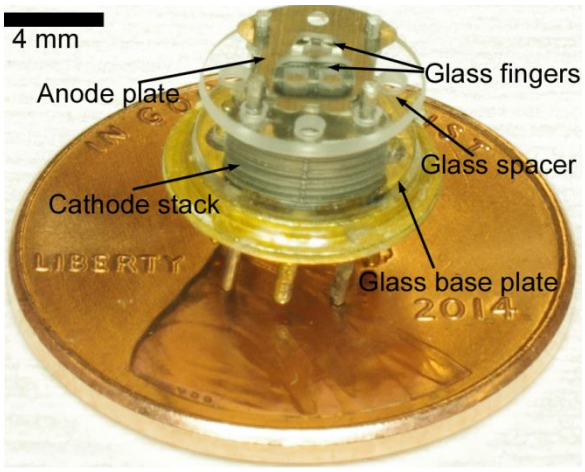

Figure 4-21: Fully assembled device

4.7 Experimental Results

4.7.1 Experimental setup

Since the total charge generated in a discharge is small it is not possible to measure detector output signal by simply measuring the current increase across a resistor during a discharge event. Instead, a commercial preamplifier (Kromek eV-550, Saxonburg, PA) is used to measure the total generated charge and output a proportional signal. Fig. 4-22 shows the detector

interface schematic [Evp13]. The op-amp of the preamplifier is powered by + / -12 V, supplied by a bench top power supply (HP E3630 A). The power connection is made using a pre-amp cable (Canberra C1402 X). The radiation detector is connected to the *detector input* of the preamplifier using BNC cable, high voltage power supply is connected to the *HV input* of the preamplifier using SHV cable, and the signal output is measured by connecting the *energy output* to the oscilloscope using BNC cable. A simple method to verify the preamplifier is powered up and proper operation of charge-to-voltage converter, is to connect *detector input* to a BNC-to-banana cable or BNC-to-alligator clips. The noise floor of the output signal from the *energy output*, when the measurement scale is at least 5 mV/div, should rise significantly due to EMI interference from the surrounding environment. If the noise floor does not rise, the chip in the preamplifier box (eV-5092) is damaged and needs to be replaced.

To reduce the EMI interference while testing, coaxial cables are used and the length of jumper wires connecting to the detector is minimized as much as possible. During the preamplifier operation, the protective FET is quite sensitive to large amount of current created and is permanently damaged by unintended sparks in the detector at voltage >650 V. To limit this current, an external 33 kΩ resistor is placed between the detector and *detector input*. However, as a precaution the voltage should not be increased beyond 650 V.

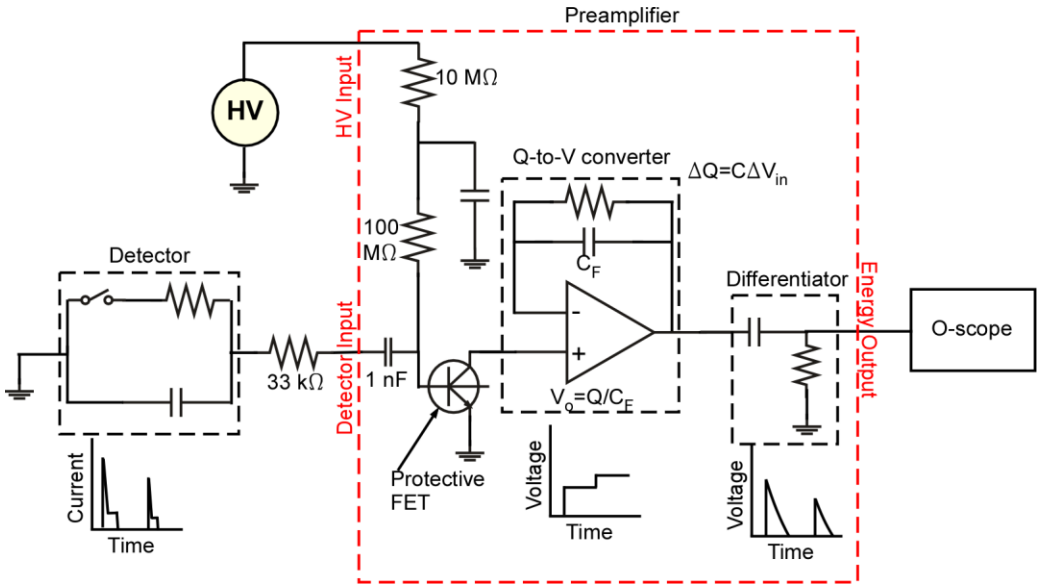

Figure 4-22: Block diagram of the radiation detector interface circuit [Evp13]

As the electron-ion pairs are created, a current is generated by their motion. This pulse of current is integrated on to the feedback capacitor (C_F), producing pulses of amplitude Q/C_F. C_F is in picofarads, and amplitude is in millivolts. In a typical measurement, the input charge per pulse is in the order of femtocoulombs. The feedback resistor R_F restores the input to ground with a very long time constant, R_FC_F, usually set to hundreds of microseconds. The result is usually called a step pulse and is illustrated above as the output of the operational amplifier resembling a staircase. Because the operational amplifier output pulses superimpose on one another in time, the next stage of the preamplifier is a high-pass filter or differentiator. This stage passes the rising edge of the signal from the op-amp, but then signal returns rapidly to the baseline so that subsequent pulses can be accurately processed. The output of the preamplifier is a rapidly decaying function and is called a tail pulse. Finally, the received tail pulse triggers the oscilloscope as it goes above a preset threshold. For every triggered signal the total count goes up by 1.

A typical output signal from the preamplifier is shown in Fig. 4-23. The output signal had a magnitude of 6 V, a rise time of 50 ns and a fall time 100 μs. Since the charge sensitivity of the preamplifier is 1.1 mV/fC, a total charge of approximately 6.6 pC or 3.47×10^7 ion-electron pairs was created per discharge.

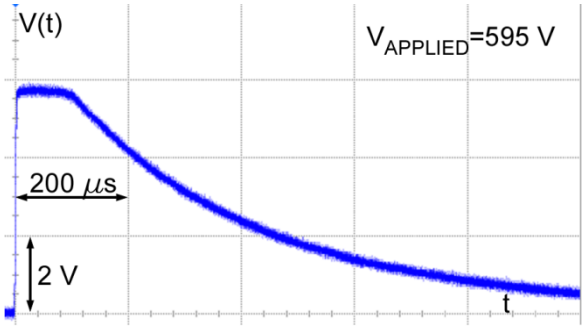

Figure 4-23: Typical preamplifier output

For the purposes of device performance evaluation under an Ar environment, a customized glass tubing was glued on the device package. It had nozzles on the side for continuous Ar gas flow during the testing (Fig.4-24).

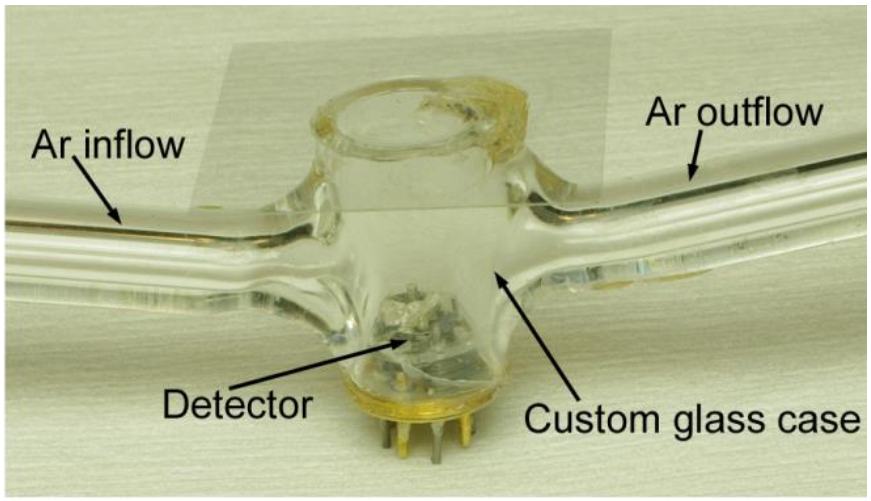

Figure 4-24: Custom glass case glued on the device package. A continuous Ar gas flow was maintained through the nozzles.

4.7.2 Range of Applied Detector Bias

The working bias range for the detector was determined using a 99 μCi ^{137}Cs source placed 3 cm away. A bias ranging from 585 V to 630 V in increments of 10 V was applied and the counts were measured for a total of 10 minutes. Afterwards, background counts (i.e. no source present) were also measured. The measured counts increased with an increasing applied bias. A peak of 89 counts was measured at an applied bias of 630 V (Fig. 4-25). However, as expected, increasing bias had negligible effect on the background counts. In fact, a maximum of only 2 counts was measured at an applied bias of 625 V. The results showed an increase in the number of detection events with an increased applied bias in the presence of the radiation source. This can be attributed to increasing electric field in regions where it was previously below the threshold level for creating a discharge and therefore no detection was taking place.

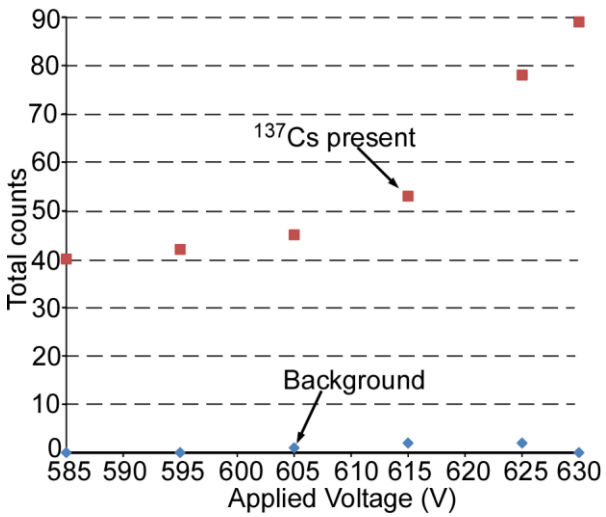

Figure 4-25: Detector operating bias range. The ^{137}Cs source was present 3 cm away from the detector

4.7.3 Spurious Discharge Reduction

In order to determine if the system is stable and spurious discharges have been eliminated, a "chi-squared test" was utilized. A chi-squared test measures the difference between the

measured variance and theoretical variance [Kno07]. The theoretical variance is modeled by Gaussian distribution and given by

$$\sigma^2 = \bar{x}_e \tag{4-1}$$

where σ^2 is the theoretical variance and $\bar{x}_e$ is the experimental mean.

Chi-squared, χ^2, is simply another parameter of the experimental data distribution and is defined as:

$$\chi^2 = \frac{1}{\bar{x}_e}\sum_{i=1}^{N}(x_i - \bar{x}_e)^2 \tag{4-2}$$

where the summation is taken over each individual data point x_i and N is the number of samples taken. Chi-squared is closely related to the experimentally measured sample variance, s^2, and the two are related by

$$\chi^2 = \frac{(N-1)s^2}{\bar{x}_e} \tag{4-3}$$

Given the fact that the data is closely modeled by the Gaussian distribution then, $s^2 \cong \sigma^2$. Therefore, the degree to which the ratio $s^2/\bar{x}_e$ differs from unity is a direct measure of the extent to which the observed sample variance differs from the predicted variance. Referring to eq. 4-3, the degree to which χ^2 differs from N-1 is a corresponding measure of the departure of the data from predictions of the Gaussian distribution. Chi-squared distribution tables can be used that are generally of the form shown in Table 4-3 [PSU14]. The df column indicates the stastical degrees of freedom in the system. This is one less than the number of independent measurements. Each column in the table is headed by a specific value of χ_p^2, defined as the probability that a random sample from a true Gaussian distribution would have a larger value of

χ^2 than the one shown in table. Very low probabilities (p less than 0.02 indicate abnormally large fluctuations in data), whereas very high probabilities (p greater than 0.98) indicate abnormally small fluctuations. A perfect fit to the Gaussian distribution for large samples would yield a probability of 0.5.

Table 4-3: Portion of a chi-squared distribution table [PSU14]:

df	$\chi^2_{.995}$	$\chi^2_{.990}$	$\chi^2_{.975}$	$\chi^2_{.950}$	$\chi^2_{.900}$	$\chi^2_{.100}$	$\chi^2_{.050}$	$\chi^2_{.025}$	$\chi^2_{.010}$	$\chi^2_{.005}$
1	0.000	0.000	0.001	0.004	0.016	2.706	3.841	5.024	6.635	7.879
2	0.010	0.020	0.051	0.103	0.211	4.605	5.991	7.378	9.210	10.597
3	0.072	0.115	0.216	0.352	0.584	6.251	7.815	9.348	11.345	12.838
4	0.207	0.297	0.484	0.711	1.064	7.779	9.488	11.143	13.277	14.860
5	0.412	0.554	0.831	1.145	1.610	9.236	11.070	12.833	15.086	16.750

For the fabricated detector, the χ^2 values along with the p-values were calculated for each applied voltage and shown in Table 4-4. 10 samples for each applied voltage were used for determining the experimental distribution. As can be observed, the p values for all voltages except 585 V are within the expected range of 0.02-0.98, proving that spurious discharges have been reduced.

Table 4-4: Calculated p-values for various applied voltages using chi-square distribution table

Applied Voltage (V)	**585**	**595**	**605**	**615**	**625**	**630**
Experimental Mean, $\bar{x}_e$	4	4.2	4.5	5.3	7.8	5.49
Experimental Variance, s^2	0.2	1.36	1.45	3.01	5.76	8.9
χ^2	0.45	2.91	2.9	5.1	6.6	5.5
p	>0.99	0.968	0.968	0.825	0.674	0.784

The comparison between the theoretical distribution and measured distribution is also showed in Fig.4-26, all the counts in one minute were within 1σ of the measured mean, when the applied

voltage was 585 V and 630 V. This was found to be true for all measurements within applied voltage range of 585 V to 630 V.

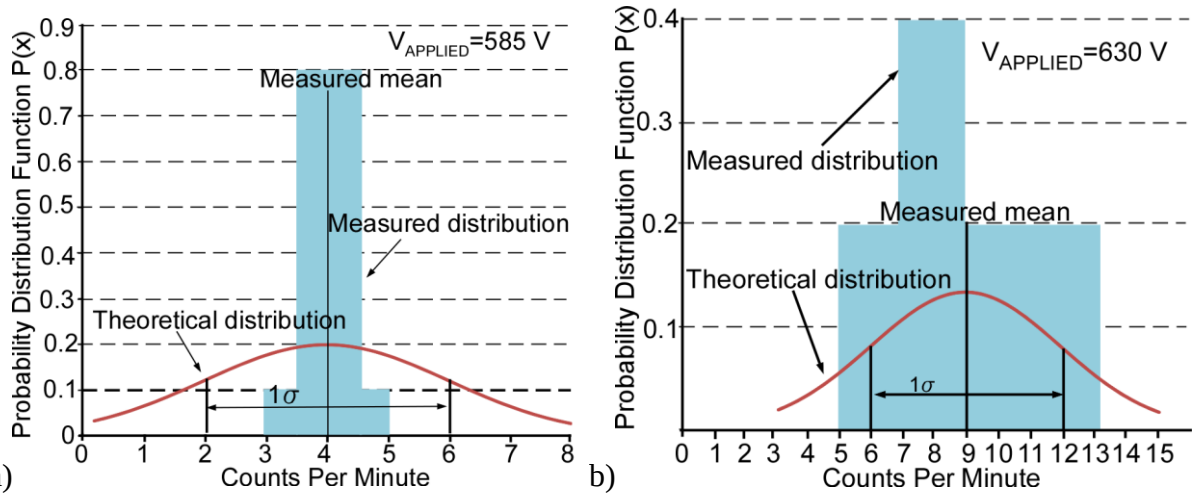

Figure 4-26: Measured and theoretical distribution at an applied voltage of a) 585 V and b) 630 V

4.7.4 Increased Sensitivity and Reduced Dead Time

The latest reported results had the largest average count rate of 8.9 cpm at 630 V when a ^{137}Cs source was placed 3 cm away. However, the measured count rate is lower than the predicted count rate for a total stack thickness of 2 mm (See section 4.4.3, Table. 4-1). This issue is currently being investigated. It is suspected that the anode trace has certain areas which are covered in a thin film of gluing layer, used to mount the glass wafers during the AJM process. Since the glue is an insulator, anode areas covered in it cannot undergo any avalanche multiplication, and any photoelectrons generated through gamma interaction are not detected in that particular cathode region. This decreases the overall sensitivity of the device. A cleaning technique that involves soaking in denatured ethyl alcohol followed by 10 minutes of ultrasonication process seems to give cleaner glass fingers void of any glue. However, these have not yet been tested to see if they improve device performance.

Similarly, dead time has not been measured because the detection rate is not high enough that it saturates the detector. Detector dead time can only be measured when the system is not able to recover from a previous discharge before the next one happens and this will happen only when the detector is detecting at a higher count rate.

.

Chapter 5: Conclusions and Future Work

To conclude this thesis has described two types of microdischarge based devices that utilize microfabrication techniques: 1) sputter ion pump (SIP) and 2) radiation detectors.

The SIP utilized micromachined Penning cell array to ignite plasma at pressures as low as 1.5 μTorr. The system pressure was reduced from 1 Torr to <10 mTorr. By reducing the interelectrode distance, the plasma is ignited as low as 400-600 V, compared to >2000 V for commercial devices. The resulting power consumption was 100-250 mW. The overall pump volume was 0.2 cm^3.

Next, a microfabricated neutron detector operating in the Geiger-Muller regime was described. The detector utilized electrodes that were lithographically micromachined from 50-μm thick stainless steel #304 foil. The cathode was coated with 2.9-μm thick layer of Gd on one side to convert thermal neutrons into fast electrons and gamma rays, which were then detected by ionization of the fill gas (Ar). Three electrodes were stacked in a cathode-anode-cathode arrangement, separated by 70-μm thick polyamide spacers, and assembled within a commercial TO-5 package. For a 90 μCi ^{252}Cf neutron source, placed at a distance of 10 cm from the detector, the total neutron count rate with an applied voltage of 285 V was typically 8.7 counts per minute (cpm). Detector dead time was measured as 5.3 ms. The device was operated at lower voltages with a reduced volume and can detect beta particles, gamma rays and neutrons compared to commercial devices which operate at >900 V, have a higher detector volume (>100 mm^3) and can only detect a combination of the listed radiation types**.**

Lastly**,** a new architecture for radiation detectors was described that improved device stability and can also increase device sensitivity and reduce dead time. The device consisted of thin metal trace (Ti/Pt: 25/100 nm) deposited on micromachined glass fingers, used as anodes. Cathodes

with hexagonal perforations were lithographically micromachined from 50 μm thick SS 304 foil. A stack of 20 cathode plates was assembled and the glass fingers were suspended in between the hexagonal perforations to form the anode-cathode system. The benefits of using such an architecture are three fold: 1) the thin metal trace suspended in the middle of a larger hexagonal perforation separated the ion drift region from the avalanche region, this reduced spurious discharges, 2) a multi-stack architecture increases the probability of interaction with gamma rays, thus increasing the device sensitivity and 3) each hexagonal perforation and glass finger forms an independent G-M detector working in parallel with other detectors. This can reduce system dead time because if one of the detectors is recovering from a discharge, other detectors will still be operating. For a 99 μCi ^{137}Cs source placed 3 cm away from the detector, a device bias range of 585-630 V was obtained. The signal to background ratio was 89:1 for an integration time of 10 minutes at an applied voltage of 630 V. Additionally, the counts per minute were within one standard deviation of the measured mean for all applied voltages, showing that spurious discharges have been eliminated. Results proving increased device sensitivity and reduced dead time remain to be measured.

Looking forward, design improvements can be made to both the SIP and radiation detector to advance device performance. Future efforts for SIP may be aimed at overcoming the prolonged start-up periods. To reduce the start-up period, efforts could center on increasing the plasma resistance at the starting pressures, such that the plasma voltage can be high at start-up. This would result in ions with sufficient kinetic energy to increase sputtering yield at start-up and better combat the plasma-induced desorption. Plasma resistance could be increased by minimizing active electrode areas or decreasing the electrode gap, among other approaches. Other future efforts in this area may include batch-fabrication and further miniaturization of the

pump. In addition, the SIP can be integrated with a Knudsen pump, capable of reducing system pressure from 200 Torr to 2.6 Torr [An14]. Therefore, in principle it is possible to reduce system pressure from 200 Torr down to <10 mTorr through the pump integration. The overall system can then be utilized in gas chromatography systems that require active pressure control

Future work for the radiation detector can aim for higher sensitivities by using a cathode metal that has a higher atomic number to provide increased gamma interaction probability. Additionally, the cathode stack height can be increased by providing even taller anode fingers. By having an even thinner anode trace, the electric field lines will be more concentrated, leading to lower operating voltages. Additionally, the electric field separation between the drift and avalanche regions will be larger eliminating spurious discharges at all applied voltages. Finally, a fully packaged device can be realized that combines the detector system with an interface circuit, ready for surveillance efforts

Appendix A

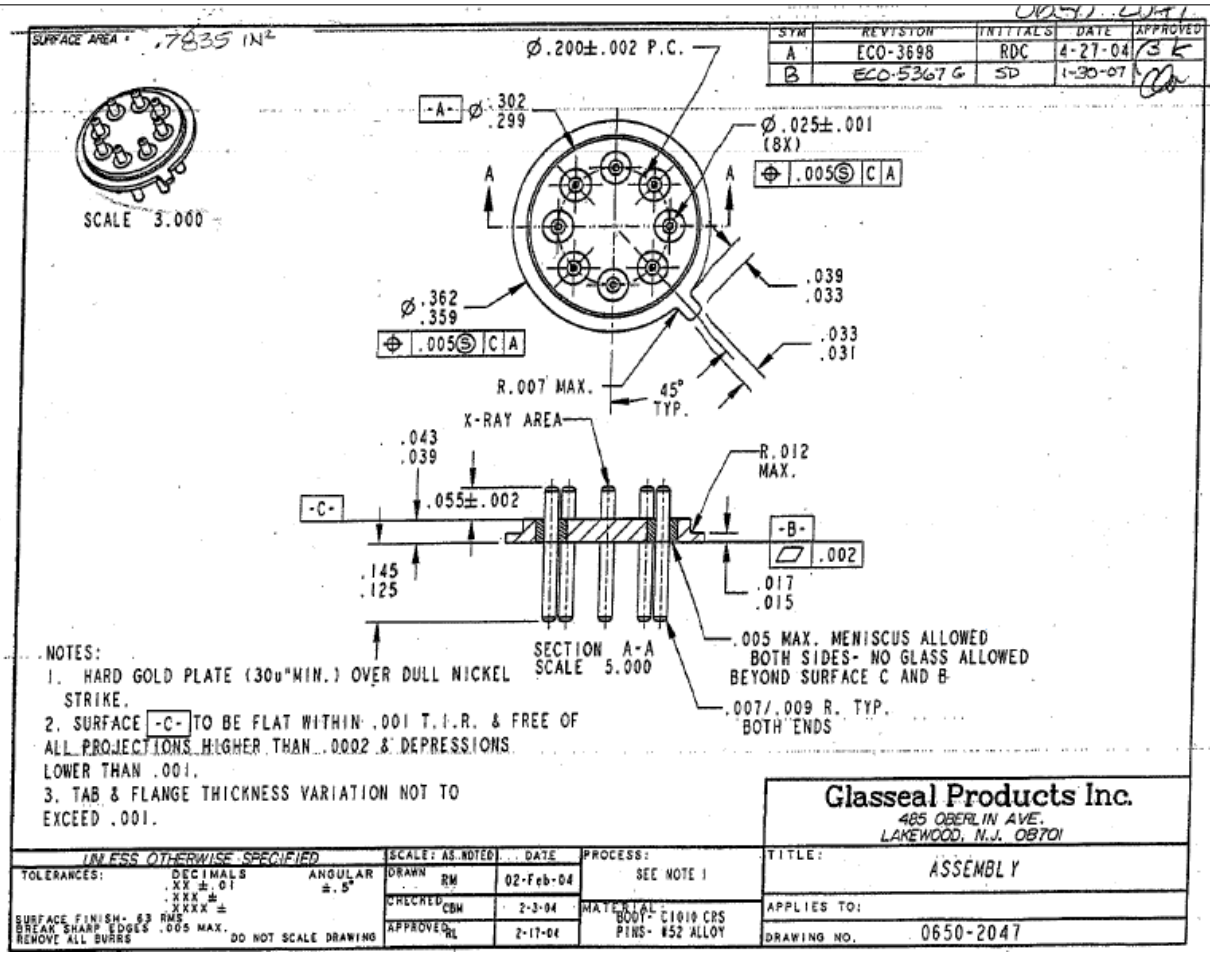

Figure A-1: TO-5 Package Dimensions

Appendix B

MATLAB code for ROC Curves

```
background_count=0.1/6;
counts=[8.9/6];
l_c=[0:0.01:9]; %critical level
for j=1:length(counts)
    for l=1:length(l_c)

pdf_a(l)=normpdf(l_c(l),background_count,sqrt(background_count));
    pdf_b(j,l)=normpdf(l_c(l),counts(j),sqrt(counts(j)));
    l=l+1;
    end
normal_pdf_back=pdf_a/sum(pdf_a);
normal_pdf_counts(j,:)=pdf_b(j,:)/sum(pdf_b(j,:));
    for k=1:length(pdf_a)
    sum_background(k)=sum(normal_pdf_back(k:length(l_c)));
    sum_activity(j,k)=sum(normal_pdf_counts(j,k:length(l_c)));
    k=k+1;
    end
    j=j+1;
end
figure(1)
plot(l_c,pdf_a)
figure(2)
plot(l_c,pdf_b)
figure(3)
plot(sum_background,sum_activity)
l_c_transpose=transpose(l_c);
pdf_a_tranpose=transpose(pdf_a);
pdf_b_tranpose=transpose(pdf_b);
sum_background_transpose=transpose(sum_background);
sum_activity_transpose=transpose(sum_activity);
```

Appendix C

MATLAB code for Monte-Carlo Simulations

```
metal_thickness=[100E-6 300E-6 500E-6 700E-6 900E-6 1100E-6];
for n=1:length(metal_thickness)
gamma_energy=[0.2 0.3 0.4 0.5 0.6 0.7 0.8 0.9 1];
mean_free_path=[9.29E-3 1.18E-2 1.37E-2 1.515E-2 1.65E-2 1.75E-2
1.83E-2 1.97E-2 2.08E-2];
for k=1:length(mean_free_path)
nsamples=5000;
count_new(n,k)=0;
    for f=1:nsamples
    x_displacement(f)=0;
    count(f)=0;
    v=3E8;
        while x_displacement(f)<metal_thickness(n)
        step_size=metal_thickness(n)/1000;
        dt=step_size/v;
        location=rand(1);
        xlocation_of_next_collision=x_displacement(f)-
(mean_free_path(k)*log(location));
        x_displacement(f)=x_displacement(f)+v*dt;
            if x_displacement(f)>xlocation_of_next_collision
            count(f)=count(f)+1;
            x_displacement(f)=metal_thickness(n);
            end
            if count(f)>0
            count_new(n,k)=count_new(n,k)+1;
            end
        end
    f=f+1;
    end
    count_new(n,k);
    sensitivity_percentage(n,k)=count_new(n,k)*100/nsamples;
k=k+1;
end
n=n+1;
end
plot(gamma_energy,sensitivity_percentage)
```

Appendix D

MATLAB code for data acquisition from the oscilloscope

```
function [elapsed_time,count_matrix]=oscilloscope_count()
% Create time device object.
deviceObj = icdevice('Agilent8064A.mdd', 'GPIB0::6::INSTR');

% Connect device object to hardware.
connect(deviceObj);

% Configure property value(s).
set(deviceObj.Trigger(1), 'Trigger_Level', 0.25);
set(deviceObj.Trigger(1), 'Trigger_Source', 'Channel1');
i=0; %the total number of counts
time=0; %time elapsed
j=0;
j_previous=0;counts=0;
elapsed_time=NaN(1,20); %create an empty matrix for vectorization
aka speed up code. Make sure this is greater than the total
points you expect to see
count_matrix=NaN(1,20); %create an empty matrix

t=timer; %timer function. This interrupts the object function
loop at every t.period to pull out the value of 'i'
t.TimerFcn = @numberofevent; %the function that is called at
every t.period
t.executionmode='fixedRate'; %this makes sure that the timer is
activated at a fixed rate
t.period=1; %period of the the time aka at what rate t.TimerFcn
is called

function numberofevent(mTimer,~) %the function that is called
every t.period
j_previous=j;%the next 3 lines are the code to determine the
number of counts in between last time the function was called
versus the present time
j=i;
counts=j-j_previous; %counts every t.period
for time=1:length(count_matrix)
     if isnan(count_matrix(time))~=1 %fill the count_matrix. If
the element of count_matrix(a) is not NaN move to the next
element. If the next element is NaN, stop right there.
     time=time+1;
     elseif isnan(count_matrix(time))==1
     break, end
```

```
end
count_matrix(time)=counts; %when the loop breaks at a NaN, pick
the most updated value of time and fill count_matrix (time)
element with the counts of that period.
elapsed_time(time)=time;
%disp(counts);
disp(time);
%disp(count_matrix);
end
%tic
start(t);
% Execute device object function(s).
for i=1:100


      set(deviceObj.Trigger(1), 'Trigger_Level', 0.25);
      groupObj = get(deviceObj,
'Waveformacquisitionlowlevelacquisition');
      groupObj = groupObj(1);
      invoke(groupObj, 'initiateacquisition');
      [st] = invoke(groupObj, 'acquisitionstatus');
if st==0
i=i;
elseif st==1
    i=i+1;
    set(deviceObj.Trigger(1), 'Trigger_Level', 10); %set to a
trigger level which your signal will never reach so that the
acquisition status can go to zero again
    invoke(groupObj, 'initiateacquisition');
    [st] = invoke(groupObj, 'acquisitionstatus');
end
end
stop(t);
%toc
end
```

References

[All00] C.P. Allier, R.W. Hollander, P.M. Sarro, and C.W.E Eijk, "Scintillation light read-out by thin photodiodes in silicon wells," *Nuclear Instruments and Methods in Physics Research A*, vol. 442, pp. 255-258, 2000.

[All01] C.P. Allier et al., "Thin photodiodes for a neutron scintillatorsilicon-well detector," *IEEE Transactions on Nuclear Science*, vol. 48, no. 4, pp. 1154-1157, Aug. 2001.

[An14] S. An, NK Gupta, YB Gianchandani, "A Si-micromachined 162-stage two-part Knudsen Pump for on-chip vacuum,"Journal of MicroMechanical Systems, Vol.23, No.2, April 2014

[Arc73] R.J.D. Arcy and N.A. Surplice, "Work function of titanium films," *Surface science*, pp. 783-788, 1973.

[ASM89] *ASM Handbook*.: ASM International, 1989

[Ato13] Photon cross sections and attenuation coefficients. [Online] http://atom.kaeri.re.kr/cgi-bin/w3xcom

[Aud90] S.A. Audet and E.M. Wouters, "High Purity Silicon X-Ray Imaging Sensor," *Sensors and Actuators*, vol. 22, no. 1, pp. 482-486, 1990

[Bac98] S. Bachmann, A.Bressan, L. Ropelewski, F. Sauli, A. Sharma, and D. Mörmann "Charge amplification and transfer processes in the gas electron multiplier, "*Nuclear Instruments and Methods in Physics Research Section A: Accelerators, Spectrometers, Detectors and Associated Equipment*,vol.*438, no.*3, 376-408, 1998

[BNL13] BNL reference database, Sigma experimental nuclear reaction data. [Online]. www.nnldc.bnl.gov

[Bro74] D.P. Brown , "Optimizing the cipping time constant for BF3 neutron detectors operated in a high level gamma environment," *IEEE Transactions on Nucear Science*, vol. 21, no. 1, pp. 763-766, Feb. 1974.

[Cha68] G. Charpak, R. Bouclier, T. Bressani, J. Favier, and C. Zupancic, "The use of multiwire proportional counters to select and localize charged particles," *Nuclear Instruments and Methods*, vol. 62, pp. 262-268, Feb 1968.

[Cha02] G. Charpak, J. Derre, Y. Giomataris, and Ph Rebourgeard, "Micromegas, a multipurpose gaseous detector," *Nuclear Instruments and Methods in Physics Research A*, vol. 478, no. 1-2, pp. 26-36, Feb. 2002

[Cha80] Brian Chapman, *Glow Discharge Processes*, 1st ed.: Wiley, 1980

[Chi93] Chin C Lee., Chen Y. Wang, and Goran Matijasevic. "Au-In bonding below the eutectic temperature." *Components, Hybrids, and Manufacturing Technology, IEEE Transactions on* 16, no. 3 (1993): 311-316.

[Cle93] F. Cleri and V. Rosato, "Tight binding potentials for transition metals and alloys," *Physics. Review B.*, vol. 48, no. 1, pp. 22-33, 1993.

[Cob58] James Cobine, *Gaseous Conductors: Theory and Engineering Applications*, Dover Publications, 1958

[Dom05] J. Doms and J. Muller, "A micromachined vapor jet pump," *Sensors and Actuators*, vol. 119, pp. 462-467, 2005.

[Dom07] M. Doms and J. Muller, "A micromachined vapor-jet vacuum pump," in *Digest of Transducers & Eurosensors '07, Lyon, France, June 10-14*, Lyon, France, 2007, pp. 2425-2428

[Ede05] J.G. Eden and S.J. Park, "Microcavity plasma devices and arrays: A new realm of plasma physics and photonic applications.," *Plasma Phys. Controlled Fusion*, vol. 47, pp. 83-92, Nov. 2005.

[Eji00] J. Ejikel, H. Storei, and A. Manz, "Atmospheric pressure dc glow discharge on a microchip and its application as molecular emission detector," *Journal of Analytical Atomic spectroscopy*, vol. 15, no. 3, pp. 297-300, 2000

[Eng04] R. Engels, U. Clemens, G. Kemmerling, and J. Schelten, "Neutron detection experiments with ionization counter and ^{6}Li converter," *IEEE Transactions on Nuclear Science*, vol. 51, no. 5, pp. 2131-2134, Jun 2004.

[Ely10] J.H. Ely L.E. Erikson, W.J. Kernan, A.T. Lintereue, E.R. Siciliano, D.L. Stephens, D.C. Stromswold, R.M. Van Ginhoven, M.L. Woodring, R.T. Kouzes, "Neutron detection alternatives to 3He for national security applications," *Nuclear Instrument and Methods in Physics Researach A*, vol. 623, no. 3, pp. 1035-1045, Nov. 2010.

[Eun08] C.K. Eun, C. Wilson, and Y. Gianchandani, "A bulk silicon micromachined structure for gas microcharge-based detection of beta particles," *Journal of Micromechanics and Microengineering*, vol. 18, July 2008.

[Eun10] C. Eun and Y.B. Gianchandani, "A Microfabricated Steel and Glass Radiation Detector with Inherent Wireless Signaling," *Journal of Micromechanics and Microengineering*, vol. 21, no. 1, pp. 1-10, Dec. 2010

[Eun11] C. Eun and Y.B. Gianchandani, "A Wireless-Enabled Microdischarge-Based Radiation Detector Utlizing Stacked Electrode Arrays for Enchanced Detection Efficiency," *IEEE/ASME J. Microelectromechanical Systems*, vol. 20, no. 3, pp. 636-643, June 2011

[ev14] eV Kromek products, EV-502 manual. [Online]

[Fie57] A.B. Fields and P.R. Fields, "Spontaneous fission neutron spectrum of Cf-252," Physics Review, vol.8 no.2, pp 411-414, Oct. 1957

[Foe06] R Foest, M. Schmidt, and K. Becker, "Microplasmas, an emerging field of low-temperature plasma science and technology," *Jounral of Mass Spectroscopy*, vol. 248, no. 3, pp. 87-102, Feb. 2006

[Gam13] Gamma Vacuum Ion Pump Users Manual, PN 900013, Rev B; www.gammavacuum.com

[Gre13] S. Green, R. Malhotra, and Y.B. Gianchandani, "Sub-Torr Chip-Scale Sputter-Ion Pump Based on a Penning Cell Array Architecture," *Journal of Microelectromechanical Systems*, vol. 22, no. 2, pp. 309-317, Apr. 2013

[GE13] GE Reuter Stokes, ^{3}He neutron detector fact sheet. [Online]. http://www.ge-mcs.com/download/reuter-stokes/GE_14158_L.pdf

[Gio96] Giomataris, Yannis, Ph Rebourgeard, Jean Pierre Robert, and Georges Charpak. "MICROMEGAS: a high-granularity position-sensitive gaseous detector for high particle-flux environments." *Nuclear Instruments and Methods in Physics Research Section A: Accelerators, Spectrometers, Detectors and Associated Equipment* 376, no. 1 (1996): 29-35.

[Gup12] N. Gupta, S. An, and Y.B. Gianchandani, "A Si-micromachined 48-stage Knudsen pump for on-chip vacuum," *Journal of Micromechanics and Microengineering*, vol. 22, pp. 1-8, 2012

[Han47] A. Hanson and J.L. Mckibben, "A neutron detector having uniform sensitivity from 10 keV to 3 MeV," *Physics Review*, vol. 72, no. 8, pp. 673-677, 1947.

[Har76] D. Harra, "Review of sticking coefficients and sorption capacities of gases on titanium films," *Journal of Vacuum Science and Technology* , vol. 13, no. 1, 1976

[Hen02] W. R. Hendee and E. R. Ritenour, *Medical Imaging Physics*., 4th ed. Hoboken, NJ: Wiley, 2002.

[Hir48] J. O. Hirschfelder, J. L. Magee, and M. H. Hull, “The penetration of gamma-radiation through thick layers,” *Physics Review*, vol. 73, no. 8, pp. 852– 862, Apr. 1948.

[Hwa06] J. Hwang et al., "The Micro Mass Spectrometer with a Carbon Nano Structure Ion Source," *Proceedings of IEEE Conference on Nano/Micro Engineered and Molecular Systems*, pp. 1220-1223, Jan. 2006

[Kan74] D. O'Kane, K. Mittal, "Plasma cleaning of metal surfaces," *Journal of Vacuum Science and Technology* , vol. 11, no. 3, pp. 567-569, 1974.

[Kem87] J.A. Kemmer, "Silicon detectors for nuclear radiation," *IEEE Transducers A.*, vol. 478, pp. 252-257, 1987.

[Kno07] Glenn F. Knoll, *Radiation Detection and Measurement*, 4th ed.: Wiley, 2007

[Kyk04] R. Kyker, N. Berry, D. Stark, N. Nachtigal, and C. Kershaw, "Hybrid Emergency Radiation Detection (HERD), a wireless sensor network application for consequence management of a radiological release," *Proceedings of SPIE*, vol. 5440, pp. 293-304, 2004

[Lea68] J.W. Leake, "An imporoved spherical dose equivalent neutron detector," *Nuclear Intstruments and Methods* , vol. 63, pp. 329-332, 1968.

[Leh03] C.E. Lehner, Z. He, and G.F. Knoll, "Intelligent gamma-ray spectroscopy using 3-D position-sensitive detectors," *IEEE Transactions on Nuclear Science*, pp. 1090-1097, Aug. 2003.

[Lin09] A. Lintereur, A.T. Kouzes, J.H. Ely, L.E. Erikson, and E.R. Siciliano, "Boron-lined neutron detector measurements," U.S. Department of Energy Report, No. PNNL 18938, 2009.

[Lut04] "The chip-scale atomic clock – Low-power physics package," *36th Annual Precise Time and Time Interval (PTTI) Meeting*, pp. 339-354, 2004

[Med03] Medalia, Jonathan. "Terrorist" Dirty Bombs": A Brief Primer." Library of Congress, Washington DC, 2003.

[Mit08] B. Mitra and Y.B. Gianchandani, "The detection of chemical vapors in air using optical emission spectroscopy of pulsed microdischarges from two and three electrode microstructures," *IEEE Sensors*, vol. 8, no. 8, pp. 1445-1454, Aug. 2008.

[MTI13] MTI corporation, mtixtl.com. [Online]. http://mtixtl.com/cdtedopedwithznptypehi-rczt11110x10x10mmtwosidespolished.aspx

[Mye97] H.P. Myers, *Introductory Solid State Physics*, 2nd ed.: Taylor and Francis, 1997.

[Nak83] M. Nakamura, "The energy spectra and the quantum efficiencies of electrons emitted from the metallic elements irradiated by 60Co gamma-rays,"*Journal of Applied Phyics.*, vol. 54, no. 6, pp. 3141–3149, Jun. 1983.

[Nem04] R.J. Nemzek , J.S. Dreicer, D.C. Torney, and T.T. Warnock, "Distributed sensor networks for detection of mobile radioactive sources," *IEEE Transactions on Nuclear Science*, vol. 51, no. 4, pp. 1693-1700, Aug. 2004

[Oed95] A. Oed, "Properties of micro-strip chambers (MSGC) and recent developements," *Nuclear Instruments and Methods in Physics Research Section A*, vol. 367, no. 1-3, pp. 34-40, Dec. 1995.

[Ohr92] M. Ohring, *The Materials Science of Thin Films*. San Diego, CA: Academic Press Inc, 1992.

[Ora14] Orau Corporation, orau.com [Online at]
https://www.orau.org/ptp/collection/GMs/GMs.htm

[Pal07] J. Pal'a, O. Stupakov, J. Bydzovsky, I. Tomas, and V. Novak, "Magnetic behaviour of low-carbon steel in parallel and perpendicular directions to tensile deformation," *Journal of Magnets and Magnetic Materials*, vol. 310, no. 1, pp. 57-62, 2007.

[Pas89] F. Paschen, "ber die zum Funkenübergang in Luft, Wasserstoff und Kohlensäure bei verschiedenen Drucken erforderliche Potentialdifferenz," *Annalen der Physik*, vol. 273, no. 69-75, 1889.

[Pen13] Penetration of radiation, bcm.edu. [Online].
http://www.bcm.edu/bodycomplab/Radprimer/radpenetration.htm

[Pen37] F.M. Penning, *Philips Technical Review*, vol. 201, no. 2, 1937.

[Phe91] V. Phelps, "Cross Sections and Swarm Coefficients for Nitrogen Ions and Neutrals in N2 and Argon Ions and Neutrals in Ar for Energies from 0.1 eV to 10 keV," *J. Phys. Chern*, vol. 20, 1991.

[Sak94] G.L. Sakaganskii, *Getter and Getter-Ion Vacuum Pumps*.: Harwood Academic, 1994.

[Scu67] W. Schuurman, "Investigation of a low pressure Penning discharge," *Physica*, vol. 36, no. 136, 1967.

[Sha05] Shamus Mcnamara and Yogesh Gianchandani, "On-chip Vacuum Generated by a Micromachined Knudsen Pump," *Journal of Microelectromechanical Systems*, vol. 14, no. 4, pp. 741-746, Aug 2005.

[Sha06] C. Shalem, R. Chechik, A. Breskin, and K. Michaeli, "Advances in thick GEM-like gaseous electron multipliers-Part I: atmospheric pressure operation," *Nuclear Instruments and Methods in Physics Research Section A*, vol. 558, no. 2, pp. 475-489, March 2006.

[She75] B. S. Sheinfux and A. Seidman, “High efficiency gamma-ray metal converters,” *Nucear Instruent Methods*, vol. 129, no. 1, pp. 177–186, Nov. 1975.

[Shi72] C. Shirley and R. Chaplin, "Evaluation of the Threshold Energy for Atomic Displacements of Titanium," *Physics Reiew. B*, vol. 5, no. 6, pp. 2027-2029, 1972.

[Shi74] U. Shimoni, B. Sheinfux, A. Seidman, J. Grinberg, and Z. Avrahami, "Investigations on metal converters for gamma-ray detection and mapping," *Nucear. Instrument Methods*, vol. 117, no. 2, pp. 599–603, May 1974.

[Ste57] E.J. Sternglass, "Theory of secondary electron emissions by high-speed ions," Physics Review, vol. 108, no. 1, pp 1-12

[Sto66] A.J. Stokes, T.J. Meal, and J.E. Myers, "Improved performance of BF3 neutron counters in high gamma fluxes," *IEEE Transactions on Nuclear Science*, vol. 13, no. 1, pp. 630-635, Feb. 1966.

[Sue95] Y. Suetsugo, "Numerical calculation of an ion pump's speed," *Vacuum*, vol. 46, no. 2, pp. 105-111, 1995.

[Vei04] G.M. Veith and N.J. Dudney, "Preparation of thin film neutron converter foils for imaging detectors," *IEEE Transactions on Nuclear Science*, vol. 51, no. 3, pp. 1034-1038, Jun 2004.

[Wad87] M. Wada, J. Suzuki, and Y. Ozaki, "Cadmium telluride ß-ray detector," *IEEE Transducers A*, vol. 478, no. 1, pp. 258-261, 1987.

[Wel01] K.M. Welch, *Capture pumping technology*, 2nd ed.: Elsevier, 2001.

[Wri07] S. Wright and Y.B. Gianchandani, "Controlling pressure in microsystem packages by on-chip microdischarges between thin-film titanium electrodes," *Journal of Vacuum Science Technology.*, vol. 25, no. 5, pp. 1711-1720, 2007.

[Wri12a] S.A Wright and Y.B Gianchandani, "Discharge based pressure sensors for high-temperature applications using 3-D and planar microstructures," *Journal of Microelectromechincal Systems*, vol. 18, no. 3, pp. 736-743, 2012

[Wri12b] S.A. Wright, Y.B. Gianchandani, and H.Z. Harvey, "A Microdischarge-Based Deflecting-Cathode Pressure Sensor in a Ceramic Package," *Journal of Microelectromechanical Systems*, pp. 1-7, Aug. 2012.

[Yam66] M. Yamashita, L.D. Stephens, A.R. Smith, and H.W. Patterson, "Detection efficiency of bare and moderated BF3-gas-filled proportional counters for isotropic neutron fluxes," *Journal of Nucear Science and Technology*, vol. 3, no. 8, pp. 343-353, Aug. 1966.

[Zho11] H. Zhou, H.Q. Li, V. Sharma, and M.A. Schimdt, "A single-stage micromachined vacuum pump achieving 164 Torr absolute pressure," in *IEEE 24th International Conference on Micro Electro Mechanical Systems (MEMS)*, Cancun, Mexico, 2011, pp. 1095-1098.

[Zoo92] J. Zook, D.W. Burns, H. Guckel, J.J. Sniegowski, R.L. Engelstad, Z. Feng "Characterstics of polysilicon resonant microbeams," *Sensors and Actuators*, vol. 35, no. 1, pp. 51-59, 1992.